EUROPEAN ORGANIZATION FOR NUCLEAR RESEARCH

CERN/SPSC 2000-021
SPSC/P317
April 24, 2000

PROPOSAL

A STUDY OF THE LINK BETWEEN COSMIC RAYS AND CLOUDS WITH A CLOUD CHAMBER AT THE CERN PS

B. Fastrup, E. Pedersen
University of Aarhus, Institute of Physics and Astronomy, Aarhus, Denmark

E. Lillestol, E. Thorn
University of Bergen, Institute of Physics, Bergen, Norway

M. Bosteels, A. Gonidec, G. Harigel, J. Kirkby*, S. Mele, P. Minginette, B. Nicquevert, D. Schinzel, W. Seidl
CERN, Geneva, Switzerland

P. Grundsøe, N. Marsh, J. Polny, H. Svensmark
Danish Space Research Institute, Copenhagen, Denmark

Y. Viisanen
Finnish Meteorological Institute, Helsinki, Finland

K. Kurvinen, R. Orava
University of Helsinki, Institute of Physics, Helsinki, Finland

K. Hämeri, M. Kulmala, L. Laakso, J.M. Mäkelä, C.D. O'Dowd
University of Helsinki, Lab. of Aerosol and Environmental Physics, Helsinki, Finland

V. Afrosimov, A. Basalaev, M. Panov
Ioffe Physical Technical Institute, Dept. of Fusion Technology, St. Petersburg, Russia

A. Laaksonen, J. Joutsensaari
University of Kuopio, Department of Applied Physics, Kuopio, Finland

V. Ermakov, V. Makhmutov, O. Maksumov, P. Pokrevsky, Y. Stozhkov, N. Svirzhevsky
Lebedev Physical Institute, Solar and Cosmic Ray Research Laboratory, Moscow, Russia

K. Carslaw, Y. Yin
University of Leeds, School of the Environment, Leeds, United Kingdom

T. Trautmann
University of Mainz, Institute for Atmospheric Physics, Mainz, Germany

F. Arnold, K.-H. Wohlfrom
Max-Planck Institute for Nuclear Physics (MPIK), Atmospheric Physics Division, Heidelberg, Germany

D. Hagen, J. Schmitt, P. Whitefield
University of Missouri-Rolla, Cloud and Aerosol Sciences Laboratory, Rolla, USA

K. Aplin, R.G. Harrison
University of Reading, Department of Meteorology, Reading, United Kingdom

R. Bingham, F. Close, C. Gibbins, A. Irving, B. Kellett, M. Lockwood
Rutherford Appleton Laboratory, Space Science & Particle Physics Depts., Chilton, United Kingdom

D. Petersen, W.W. Szymanski, P.E. Wagner, A. Vrtala
University of Vienna, Institute for Experimental Physics, Vienna, Austria

CLOUD† Collaboration

∗) spokesperson

†) Cosmics Leaving OUtdoor Droplets

Contents

1 Summary

In 1997 Svensmark and Friis-Christensen [1] announced a surprising discovery that global cloud cover correlates closely with the galactic cosmic ray intensity, which varies with the sunspot cycle. Although clouds retain some of the Earth's warmth, for most types of cloud this is more than compensated by an increased reflective loss of the Sun's radiation back into space. So more clouds in general mean a cooler climate—and fewer clouds mean global warming. The Earth is partly shielded from cosmic rays by the magnetic disturbances carried by the solar wind. When the solar wind is strong, at the peak of the 11-year sunspot cycle, fewer cosmic rays reach the Earth. The observed variation of cloud cover was only a few per cent over the course of a sunspot cycle. Although this may appear to be quite small, the possible long-term consequences on the global radiation energy budget are not.

Beyond its semi-periodic 11-year cycle, the Sun displays unexplained behaviour on longer timescales. In particular, the strength of the solar wind and the magnetic flux it carries have more than doubled during the last century [2]. The extra shielding has reduced the intensity of cosmic rays reaching the Earth's atmosphere by about 15%, globally averaged. This reduction of cosmic rays over the last century is independently indicated by the light radioisotope record in the Greenland ice cores. If the link between cosmic rays and clouds is confirmed it implies global cloud cover has decreased during the last century. Simple estimates indicate that the consequent global warming could be comparable to that presently attributed to greenhouse gases from the burning of fossil fuels.

These observations suggest that solar variability may be linked to climate variability by a chain that involves the solar wind, cosmic rays and clouds. The weak link is the connection between cosmic rays and clouds. This has not been unambiguously established and, moreover, the microphysical mechanism is not understood. Cosmic rays are the dominant source of ions in the free troposphere and stratosphere and they also create free radicals. It has been proposed [3]–[5] that ions may grow via clustering to form aerosol particles which may ultimately become cloud condensation nuclei (CCN) and thereby seed clouds. Recently a search for massive ions in the upper troposphere and lower stratosphere was started by MPIK-Heidelberg [6] using aircraft-based ion mass spectrometers. Preliminary results indeed indicate the presence of massive positive and negative ions. In addition to their effect on aerosol formation and growth, cosmic rays may also possibly enhance the formation of ice particles in clouds [7].

We therefore propose to test experimentally the link between cosmic rays and clouds and, if confirmed, to uncover the microphysical mechanism. We propose to make the measurements under controlled laboratory conditions in a beam at the CERN Proton Synchrotron (PS), which provides an adjustable source of "cosmic rays". The experiment, which is named CLOUD (Cosmics Leaving OUtdoor Droplets), is based on a cloud chamber that is designed to duplicate the conditions prevailing in the atmosphere. To our knowledge, cloud chamber data under these conditions have never been previously obtained.

This document is organised as follows. First we provide an overview of the scientific motivation for the experiment, including a summary of the most recent satellite observations of clouds. We present the scientific and experimental goals of CLOUD in

Section 3. These are followed in Sections 4–7 by descriptions of the detector and its performance, of the data interpretation and cloud modelling, and of the accelerator requirements. The planning for the experiment is summarised in Section 8. Since this proposal concerns several different scientific disciplines—atmospheric, solar-terrestrial and particle physics—we provide fairly extensive background information, mostly in footnotes and in Appendices A–E which cover, respectively, cloud physics, aerosol-cloud-climate interactions, classical operation of a Wilson cloud chamber, cosmic rays in the atmosphere, and cloud models.

2 Scientific motivation; the origins of climate change

2.1 Global warming

Global warming is a major concern of the world, with its potentially devastating effects on coastal settlements and world agriculture. The steep rise in greenhouse gas emissions since the Industrial Revolution has increased the CO_2 concentration in the atmosphere by about 30%. This is widely believed to be the dominant cause of the observed rise of about 0.6°C in the global mean surface temperature during this period [8].

A small systematic rise or fall in the global temperature is caused by a net imbalance ("forcing") in the Earth's energy radiation budget. The radiative forcing caused by the increase in the CO_2 fraction since 1750 is estimated to be 1.5 Wm^{-2} (Fig. 1) [8], compared with the global average incoming solar radiation[1] of 342 Wm^{-2}, i.e. an imbalance of only 0.4%. After including the effects of all greenhouse gases (+2.45 Wm^{-2}), aerosols[2] (-0.5 Wm^{-2}) and their indirect influence on clouds (-0.75 Wm^{-2}, but poorly known), the present net radiative forcing from mankind is estimated to be about 1.2 Wm^{-2}.

The climate models [8] upon which the predictions of greenhouse warming depend have gradually improved as new effects and better data have been incorporated. They now provide a reasonable match to the observed variation in global temperatures over the last century. However they remain subject to significant uncertainties, especially from feedback mechanisms and from the effects of anthropogenic aerosols. The latter contribute directly by scattering and absorption of radiation and also indirectly by influencing cloud formation. Nonetheless it is in this climate of scientific uncertainty that major political decisions on greenhouse gas emissions are presently being made (Earth Summit in Rio de Janeiro, 1992, and UN Climate Convention in Kyoto, 1997) that will have a profound effect on the economic development of both the developed and the developing countries. The need for such political decisions to be based on sound scientific grounds is self evident, and a major world-wide research effort on climate change is underway.

[1] By convention, the incoming solar radiation of about 1366 Wm^{-2} is averaged over the total surface area of the Earth, i.e. divided by a factor four, to give a global average of 342 Wm^{-2}.

[2] Aerosols are 0.001–1 μm diameter particles of liquid or solid suspended in the air [9]. Atmospheric aerosols include dust, sea salt, soot (elemental carbon), organic compounds from biomass burning, sulphates (especially H_2SO_4 and $(NH_4)_2SO_4$) from SO_2, and nitrates (especially HNO_3) from NO and NO_2. Aerosol concentrations vary typically from $\sim$100 cm^{-3} in maritime air to $\sim$ 1000 cm^{-3} in unpolluted air over land masses, but there are large variations from these values.

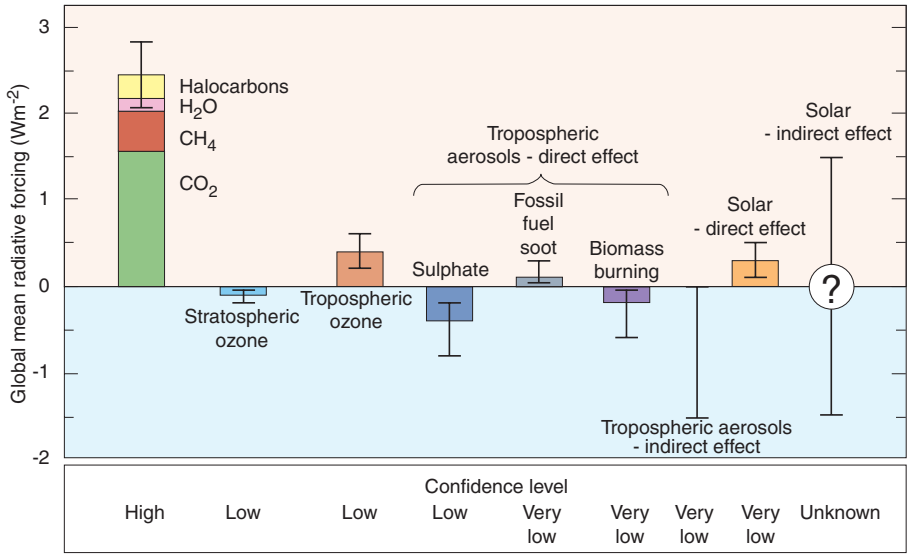

Figure 1: IPCC estimates of the global annual averaged radiative forcings due to changes in anthropogenic greenhouse gases and aerosols from 1850–1992 (first seven columns of the figure) [8]. Positive forcings lead to a warming and negative forcings cause a cooling. Natural changes due to the Sun are indicated by the final two columns; the first is the IPCC estimate of changes in solar output over the same period and the second concerns the present CLOUD proposal to study of the influence of galactic cosmic rays on cloud formation. Since the galactic cosmic ray flux is modulated by the solar wind, this would provide a mechanism for indirect solar radiative forcing.

2.2 Solar variability

In order to determine the influence of mankind on climate change it is first necessary to understand the natural causes of variability. A natural effect that has been hard to understand physically is an apparent link between the weather and solar activity—the sunspot[3] cycle.

The observation that warm weather seems to coincide with high sunspot counts and cool weather with low sunspot counts was made as long ago as two hundred years by the astronomer William Herschel [11] who noticed that the price of wheat in England was lower when there were many sunspots, and higher when there were few. The best known example of this effect is known as the Maunder Minimum [12], the Little Ice Age between 1645 and 1715—which ironically almost exactly coincides with the reign of Louis XIV,

[3]Sunspots are areas of the Sun's photosphere where strong local magnetic fields (typically 2500 Gauss, to be compared with the Earth's field of about 0.3 Gauss) emerge vertically [10]. They appear dark because their temperature is about half of the surrounding photosphere (3,000 K compared with 5,800 K). They are generated by the differential rotation of the Sun with respect to latitude: one revolution takes 25 days at the equator and 28 days at mid-latitudes. This transforms the quiescent dipole field into a toroidal field and eventually creates "knots" of strong localised fields. These knots may penetrate the photosphere to form sunspots, which appear cooler due to modification of the normal convective motions of the plasma by the strong magnetic fields. The sunspots first appear at high latitudes and then gradually migrate towards the equator. They eventually disappear by magnetic recombination, leaving a quiescent dipole field once more (but of opposite polarity). The cycle from dipole to toroidal and back to dipole field is known as the solar (sunspot) cycle and takes about 11 years on average.

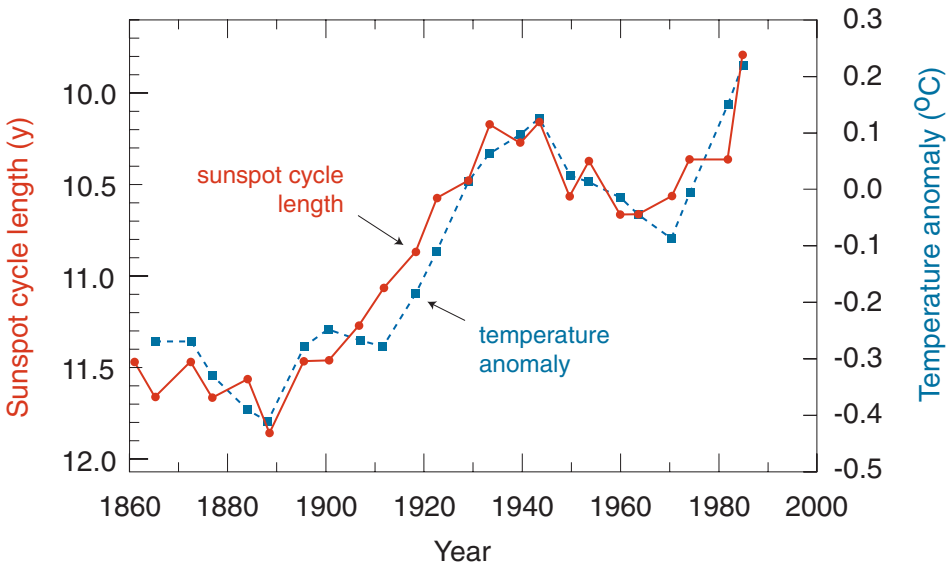

Figure 2: Variation during the period 1861–1989 of the sunspot cycle length (solid curve) and the temperature anomaly of the Northern Hemisphere (dashed curve) [16]. The temperature data are from the IPCC [8].

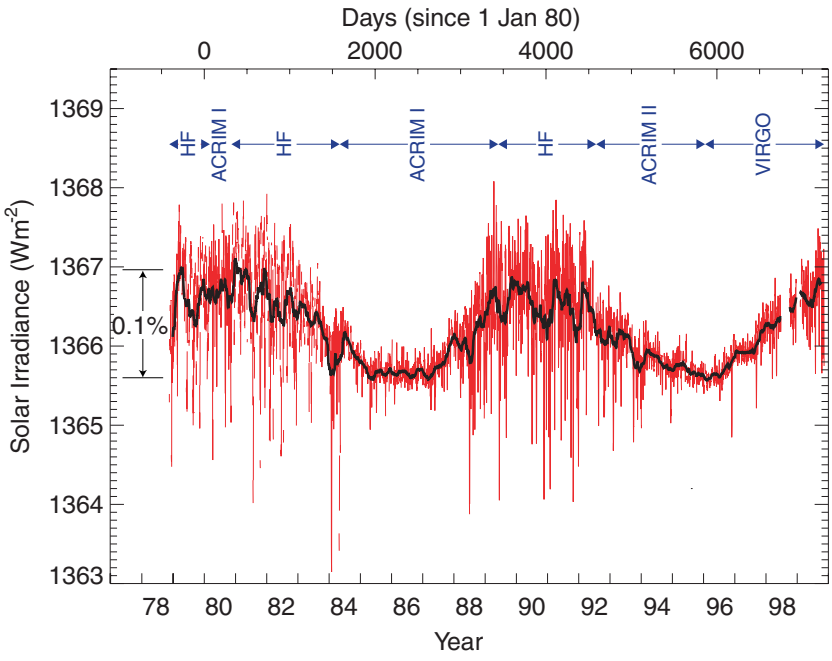

Figure 3: Satellite measurements of the variation of the Sun's irradiance over two solar cycles [19]. Sunspot maxima occurred around the beginning of 1981 and mid 1990, and sunspot minima occurred around the beginning of 1986 and 1996. The rapid fluctuations are due to sunspots rotating into the field of view. The solid line represents the smoothed data. The measurements are from active cavity irradiance monitors (ACRIM I and II) on the Solar Maximum Mission Satellites and from HF-type radiometers on the Nimbus 7 Earth Radiation Budget (ERB) and Earth Radiation Budget Satellite (ERBS) experiments.

le Roi Soleil, 1643–1715—during which time there was an almost complete absence of sunspots. During this period the River Thames in London regularly froze across and fairs complete with swings, sideshows and food stalls were a standard winter feature.

Since that time there have been numerous observations and non-observations of an apparent link between climate and the sunspot cycle [13]–[15]. One example of a positive observation was presented by Friis-Christensen and Lassen in 1991 (Fig. 2) [16]. They used the sunspot cycle length as a measure of the Sun's activity. The cycle length averages 11 years but has varied from 7 to 17 years, with shorter cycle lengths corresponding to a more magnetically-active Sun. A correlation was found between the sunspot cycle length and the change in land temperature of the Northern Hemisphere in the period between 1861 and 1989. The land temperature of the northern hemisphere was used in order to avoid the lag by several years of air temperatures over the oceans, due to their large heat capacity. The data shown in Fig. 2 cover the period during which greenhouse gas emissions are believed to be the major cause of the global warming of 0.6°C. Of particular note is the dip between 1945 and 1970, which cannot be explained by the steadily rising greenhouse gas emissions but seems to coincide with a decrease in the Sun's activity.

In the absence of sufficiently sensitive measurements, it was suspected that the Sun's irradiance may be fluctuating over the solar cycle. However, the steadiness of the Sun's irradiance over almost two sunspot cycles has recently been established by satellite measurements (Fig. 3) [17]-[19]. The solar irradiance is slightly higher at sunspot maximum; although sunspots are cooler and have reduced emission, this is more than compensated by an associated increase in nearby bright areas known as *plages* and *faculae*. The mean irradiance changes by about 0.1% from sunspot maximum to minimum which, if representative over a longer time interval, is too small (0.3 Wm^{-2}, globally-averaged) to account for the observed changes in the Earth's temperature. However it is not completely negligible, and current estimates—using the data shown in Fig. 3 together with the sunspot record—attribute a net direct radiative forcing over this century of about +0.3 Wm^{-2} due to changes in solar irradiance (indicated by the "solar - direct effect" in Fig. 1).

2.3 Cosmic rays and cloud variability

It is well known that the cosmic ray intensity on Earth is strongly influenced by the solar wind[4] [20], whose strength varies with the sunspot cycle (Fig. 4 and Appendix D.2). The solar wind contains frozen-in irregular magnetic fields. Galactic cosmic rays that enter the solar system suffer many scatters from these irregularities and undergo a random walk. This has been theoretically shown [21] to be equivalent to a heliocentric retarding electric potential, which varies over the course of the solar cycle. At times of low sunspot activity, the solar wind is weaker and the retarding potential at the Earth's orbit is about 400 MV. At times of high sunspot activity, the retarding potential is about 1200 MV, thereby reducing the low-energy component of galactic cosmic radiation reaching Earth.

[4]The solar wind is a continuous outward flow of charged particles (mainly protons and electrons, with 5% helium nuclei) from the plasma of the Sun's corona. Sources include streams from a honeycomb of magnetic fields in the solar atmosphere, and large and small mass ejections. The solar wind creates the huge heliosphere of the Sun that extends out 50–100 AU, well beyond the orbit of Neptune. At the Earth's orbit the solar wind has a velocity of 350–800 km s^{-1} (β = 0.001–0.003) and an intensity of (0.5–5)$\times 10^8$ particles cm^{-2} s^{-1}, carrying with it a magnetic field of about 5×10^{-5} Gauss.

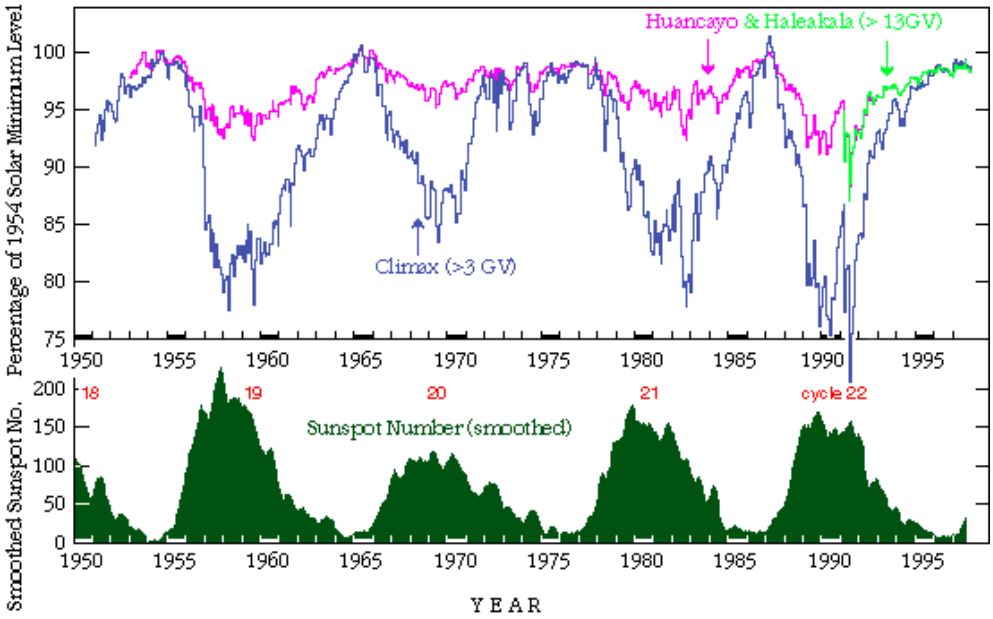

Figure 4: Variation with time of sunspot number and cosmic ray flux, as measured by ground-based neutron counters. The neutron data are from the University of Chicago neutron monitor stations at Climax, Colorado (3400 m elevation; 3 GeV/c primary charged particle cutoff), Huancayo, Peru (3400 m; 13 GeV/c cutoff) and Haleakala, Hawaii (3030 m; 13 GeV/c cutoff). The stronger modulation of the cosmic ray flux at higher latitudes (Climax) is due to the lower primary cutoff energy. The neutrons are mostly produced by primary hadronic interactions in the first 1–2 λ_{int} of the atmosphere and therefore measure the changes in cosmic ray intensity at altitudes above about 13 km. The primary cosmic radiation is about 80% protons, 15% He nuclei and 5% heavier nuclei. At sea level the most numerous *charged* particles are muons and their fluctuation is less pronounced—about 3% over a solar cycle [20]—since they are produced from the high-energy component of cosmic radiation, which is less affected by the solar wind.

The cosmic rays are also deflected by the Earth's geomagnetic field, which they must penetrate to reach the troposphere.[5] This sets a minimum vertical momentum of primary charged particles at the geomagnetic equator of about 15 GeV/c, decreasing to below 0.1 GeV/c at the geomagnetic poles. (The actual cutoff at high latitudes is determined by the atmospheric material; for example a 1 GeV/c proton can penetrate only as far as 15 km altitude.) As a result the modulation of the cosmic ray intensity is more pronounced at higher geomagnetic latitudes (Figs. 4 and 52). Averaged over the globe, the variation of the cosmic ray flux is about 15% between solar maximum and minimum

[5]The troposphere is the lowest level of the atmosphere and the region where there is enough water vapour and vertical mixing for clouds to form under suitable conditions. The troposphere has a depth of about 18 km over the tropics, decreasing to about 8 km over the poles; it contains about 80% of the mass of the atmosphere. The troposphere is divided into the *planetary boundary layer*, extending from the Earth's surface up to about 1 km, and the *free troposphere*, extending from 1 km to the boundary with the stratosphere (the tropopause). There is an overall adiabatic lapse rate of temperature in the troposphere of between 6°C (moist air) and 9.7°C (dry air) per km altitude, reaching a minimum of about -56°C at the tropopause. The stratosphere extends up to about 50 km and has a temperature that slowly rises with altitude due to absorption of solar UV radiation. This leads to very little turbulence and vertical mixing and, in consequence, it contains relatively warm, dry air that is largely free of clouds.

[22, 23]. It represents one of the largest measurable effects of sunspot activity near the Earth's surface.

But how could cosmic rays affect the Earth's weather? The energy deposited by cosmic rays is only a few parts per billion compared with the incident solar energy, so a strong amplifying mechanism would be necessary. The breakthrough was made by Svensmark and Friis-Christensen in 1997 [1] who discovered an unexpected correlation between global cloud cover and the incident cosmic ray intensity. The satellite data, which are shown in Fig. 5 (taken from the later ref. [24]), display a clear imprint of the solar cycle on global cloud cover.[6] Over a sunspot cycle, the absolute variation of global cloud cover is about 3%, to be compared with an average total cloud cover of about 65%, i.e. a relative fraction of about 5%.

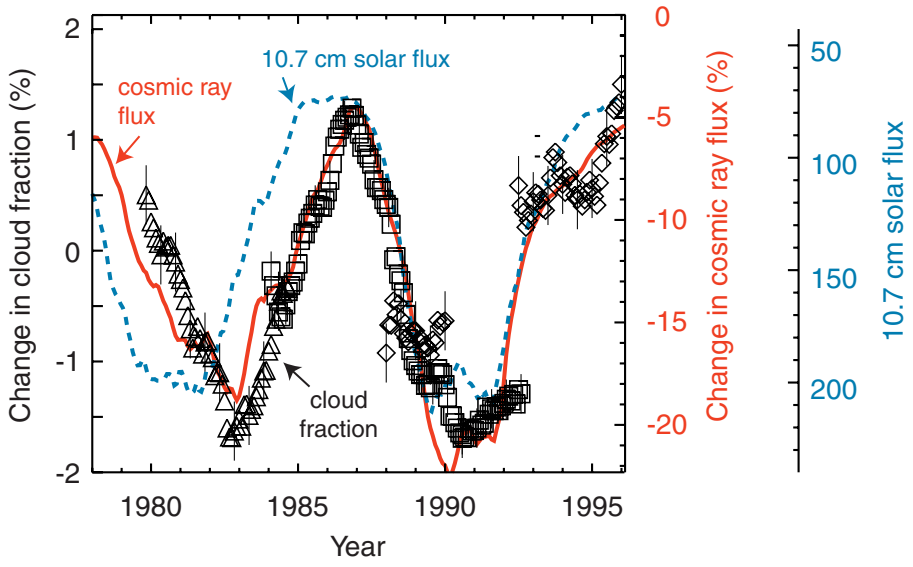

Figure 5: Absolute percentage variation of global cloud cover observed by satellites (data points; left hand scale) and relative percentage variation of cosmic ray flux (solid curve, normalised to May 1965; near-right hand scale) [1, 24]. Also shown is the solar 10.7 cm microwave flux (dashed curve, in units of 10^{-22} $\mathrm{Wm^{-2}Hz^{-1}}$; far-right hand scale). The cloud data are restricted to oceans; Nimbus 7 (triangles) and DMSP (diamonds) data are for the southern hemisphere over oceans, and ISCCP-C2 (squares) data are for oceans with the tropics excluded. The error bars indicate representative statistical errors. The cosmic ray data are neutron measurements from Climax (Fig. 4). All data are smoothed using a 12-month running mean. A more recent analysis is shown in Figs. 6 and 7.

In addition to this observation of cloud variations over the timescale of order one solar cycle, other data sets have been analysed to investigate transient effects on clouds due to sudden changes in the cosmic ray flux. Forbush decreases of galactic cosmic rays occur due to solar disturbances on timescales of order days and therefore allow study of short-term cosmic-ray induced changes. Pudovkin and Veretenenko [25] report observations of a short-term decrease of cloudiness that correlates with Forbush decreases, using a superposed epoch analysis on data obtained visually. Their observation is restricted to a

[6]The terms cloud cover, cloud frequency and cloud fraction are interchangeable.

narrow range of latitudes (60N–64N), and they suggest that cirrus clouds are responsible. A similar analysis of the effects of Forbush decreases on rainfall has been carried out by the Lebedev Physical Institute [26] using data from 50 meteorological stations in Brazil for 47 Forbush events recorded between 1956 and 1992. A 30% drop in rainfall (corresponding to a 3σ change from the mean) is observed on the initial day of the onset of the Forbush decrease.

A detailed mechanism modifying ice clouds has been proposed in a series of papers (notably Tinsley and Dean [7]), which suggests that significant changes in the latent heat released within supercooled clouds can occur as a result of aerosol electrification. The proposed mechanism is that charged aerosols are more effective than neutral aerosols as ice nuclei, which are generally rare in the atmosphere. The aerosol electrification is due to the ionisation created by cosmic rays. Rather than a comparison with cloudiness, Tinsley's superposed epoch analysis uses a dynamical parameter, the Vorticity Area Index (a measure of the regional scale motion), for which he finds a correlation with Forbush decreases. The mechanism of latent heat release via electrical enhancement of ice nucleation can lead to substantial amplification of the ionisation energy deposited by cosmic rays in the atmosphere.

2.4 Other solar-induced climate variability

Other solar activity also follows the sunspot cycle, so in principle the cloud variations might be attributed to (a) a direct effect of cosmic rays on clouds, (b) a direct effect of other solar activity on clouds, or (c) an effect of solar activity on global weather that indirectly results in a change in cloud cover.

Although the other explanations mentioned here cannot be ruled out, Fig. 5 contains evidence favouring (a), the direct cosmic ray effect, which is to be investigated in the CLOUD experiment. The solar 10.7 cm microwave flux is a good proxy both for variations in the sunspot count and for variations in the solar output of other electromagnetic radiation, namely visible light, X-rays and ultraviolet rays. In Fig. 5, the change in cloud fraction followed the cosmic rays closely but sometimes lagged as much as two years behind the change in the 10.7 cm flux. Delays in cosmic ray variations occur because disturbances in the solar wind, which scatter the cosmic rays, involve events (coronal mass ejections—CMEs, and co-rotating interaction regions) only loosely related to the sunspot count. Moreover the heliosphere is so large that disturbances can take up to about a year to reach its boundary, the heliopause. The delays show that the cloud variations correlate more closely with the cosmic rays than with the solar electromagnetic flux.

Could the solar wind have a direct effect on clouds, while coincidentally modulating the cosmic rays? This is unlikely because solar wind protons have very little energy (a few keV) and if they penetrate the Earth's magnetosphere in the auroral zone, the outer atmosphere stops them at altitudes above 100 km. Shock waves associated with CME disturbances colliding with the slow solar wind can accelerate protons to 100 MeV or more, generating solar cosmic rays, but only rarely do they have sufficient energy to reach the tropopause at 8–18 km altitude.

The *sign* of the effect is a consideration in assessing possible solar mechanisms influencing the cloud fraction. While the cloud fraction correlates positively with the cosmic ray intensity, it correlates negatively with the solar electromagnetic radiation and with

the strength of the solar wind. If enhancements in electromagnetic radiation or the solar wind were responsible for a direct effect on clouds, they would be in the counter-intuitive sense of reducing the cloud fraction.

As to whether changes in cloud fraction might be an indirect result of changes in global weather due to solar effects that coincide with the cosmic ray modulation, none of the other mechanisms on offer for a solar role in climate change suggests an effect on cloud fraction. Mechanisms currently discussed include:

- Increases in visible light, causing warming at the Earth's surface.
- Increases in ultraviolet (UV), causing warming in the stratosphere [28].[7]
- Solar-induced turbulence in the Earth's outer atmosphere that scatters gravity waves back to the lower stratosphere, again with warming effects [29].

All of these mechanisms seem likely to affect the geographical distribution of clouds, in particular by a poleward shift of the mid-latitude jet streams and depressions, during high solar activity. There is no obvious short-term link with cloud fraction.

Solar activity has many manifestations, and all of the means by which it may influence the Earth's climate deserve further investigation. It is no part of our case to suggest that the link between cosmic rays and clouds is the only important solar-climatic mechanism. For the reasons given in this section we nevertheless consider that the preferred interpretation of Figure 5 is the simplest, namely that cloud behaviour is directly influenced by cosmic rays. The opinion is reinforced by recent studies summarised in the next section.

2.5 Improved satellite measurements of clouds

Currently the best continuous satellite observations of cloud properties are from the International Satellite Cloud Climate Project (ISCCP) D2 data, which covers the period from July 1983 to September 1994 [31, 32]. The D2 data are constructed by combining uniform analysis results from several satellites—up to five geostationary satellites and two polar orbiting satellites—to obtain complete global coverage every 3 hours. Cloud measurements are made at visible ($\lambda \sim 0.6$ μm), near infra-red (3.7 μm) and infra-red (IR) wavelengths (10–12 μm). The IR measurements have the advantage that they provide continuous detection through day and night. As well as cloud frequency, the cloud-top temperatures and pressures are also determined. The temperatures and pressures are obtained by assuming an opaque cloud, i.e. an emissivity $\epsilon = 1$, and adjusting the cloud's pressure level (effectively the cloud-top altitude) in the model until the reconstructed outgoing IR flux matches that observed. The clouds are classified into 3 altitude ranges according to the pressure at their top surface: low, >680 hPa (approximately <3.2 km); middle, 680–440 hPa (3.2–6.5 km); and high, <440 hPa (>6.5 km).

[7] Only wavelengths above 300 nm penetrate to the troposphere and the Earth's surface. These show a tiny peak-to-peak variation of less than 0.1% over the solar cycle. However the variation is more pronounced in the UV. Wavelengths below 300 nm, which account for only about 2% of the total solar irradiance, vary by about 5% (200–300 nm) to 50% (100–150 nm), or even more at shorter wavelengths [27]. The UV radiation is absorbed by ozone in the upper stratosphere, which warms as a result. This has the potential to influence large-scale dynamics of the troposphere [28]-[30], although vertical mixing between the stratosphere and troposphere is weak.

The cloud frequency for high, middle and low IR clouds is shown in Fig. 6 together with the cosmic ray variation over the same period [33]. In contrast with the previous analyses [1, 24], these data are spatially and temporally unrestricted; they include clouds over the entire globe, during both day and night. The data indicate the presence of a significant correlation between cosmic ray intensity and the frequency of *low* clouds, below about 3.2 km, but none with clouds at higher altitudes. Since the cosmic ray and ionisation intensities—and their variations over the solar cycle—are largest above about 10 km altitude (Appendix D and Fig. 50), this would suggest mixing from the upper to lower troposphere may be involved. Indeed, vertical mixing is a prominent feature of tropospheric dynamics, where large-scale vertical transport of air, chemical species and ions can occur on timescales as short as a few hours via strong convective updrafts and the accompanying downdrafts.

Figure 7 shows the low IR cloud fraction together with the variations of cosmic ray flux (solid line) and 10.7 cm solar irradiance over this period. The data are smoothed using a 12-month running mean to allow easy comparison with the earlier analysis shown in Fig. 5. The data confirm the presence of a solar cycle modulation of the cloud fraction, and continue to favour the cosmic ray interpretation.

The global map of the low cloud frequency correlation is shown in Fig. 8a) [33]. The fraction of the Earth's surface with a correlation coefficient above 0.6 is 14.2%. Figure 8b) shows the correlation of low IR cloud-top temperature and cosmic ray flux. A strong and continuous band of high correlation (>0.6) extends throughout the tropics, covering 29.6% of the globe. This is a surprising result since the solar modulation of the cosmic ray intensity is a minimum near the geomagnetic equator, with a peak variation about 5% (Fig. 4). No significant correlations are observed between cosmic rays and the cloud-top temperatures of middle and high clouds (these data are not mapped here).

In summary, the ISCCP-D2 IR cloud data show a clear correlation of the cosmic ray intensity with low clouds, below about 3 km altitude (largely comprising stratocumulus and stratus cloud types), and no correlation with higher clouds. (As before, these data could alternatively be interpreted as a possible solar-cloud link via the UV irradiance.) The correlation appears in two distinct parameters: a) the cloud frequency (coverage), and b) the cloud-top temperature. The spatial distribution of the correlation across the globe is different in the two cases; the regions of high correlation of cloud frequency are widely scattered whereas the cloud-top temperature correlation is essentially continuous over the entire tropics. At present the reason for these different spatial distributions is not known, although we note that these are two separate cloud properties. Cloud frequency measures the presence or absence of a cloud, reflecting changes in the cloud lifetimes, cloud sizes, or cloud number. On the other hand, the inferred cloud-top temperature depends on its altitude and on the microphysical properties of existing clouds.

The signs of the two correlations are that more cosmic rays give more clouds and a higher cloud-top temperature. Under the assumption of opaque clouds, the cloud-top temperature effectively measures the altitude at the top of the cloud; a higher cloud-top temperature implies a lower cloud. However the observed properties of low maritime clouds suggest that they are not opaque [34]. If the assumption of opaque clouds is relaxed, an alternative interpretation is that the cloud altitude does not change with increasing cosmic ray flux, but that the emissivity of the cloud increases. The latter could be caused by microphysical changes such as an increase in the droplet number concentration.

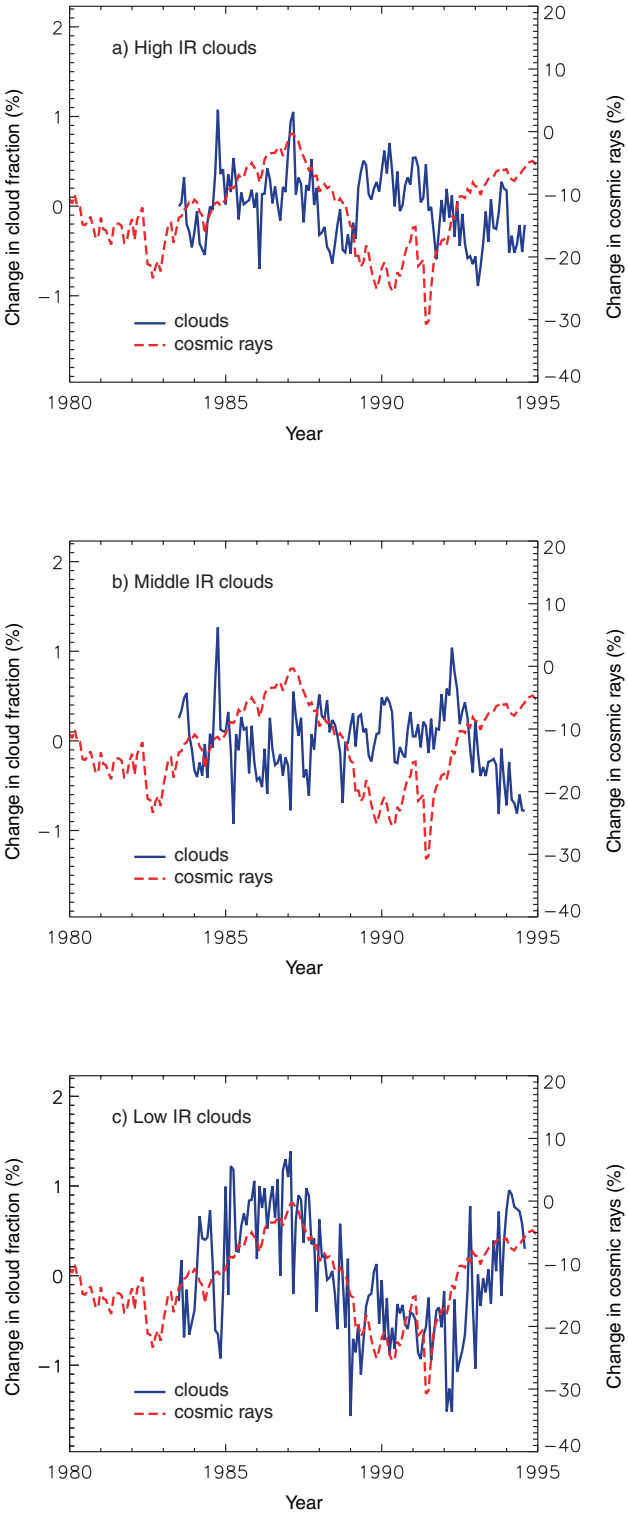

Figure 6: Monthly mean values for the global absolute variations of IR cloud coverage for a) high (<440 hPa), b) middle (440–680 hPa), and c) low (>680 hPa) clouds (solid lines) [33]. Cosmic rays, measured by the Climax neutron monitor, are indicated by the dashed lines, normalised to May 1965. The mean global cloud fraction over this period for high, middle and low IR clouds is 13.5%, 19.9%, and 28.0% respectively. The cloud measurements are obtained from the ISCCP-D2 IR dataset [31, 32].

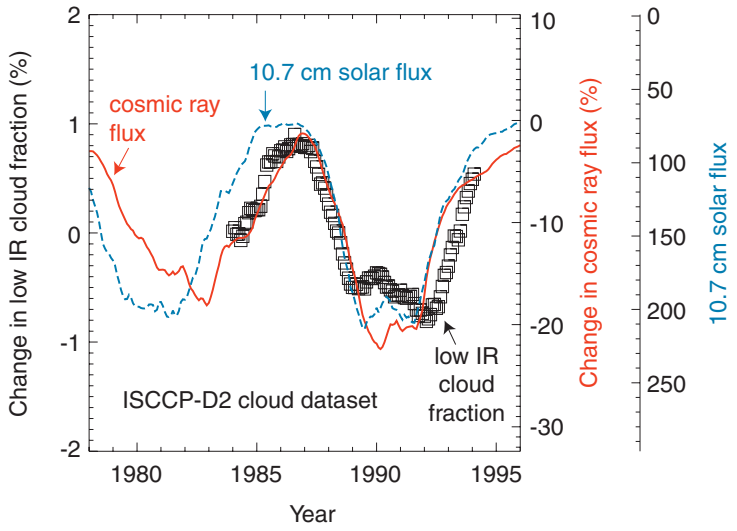

Figure 7: Variation over the period 1983-1994 of the low IR (10–12 μm) cloud fraction in the ISCCP-D2 dataset (from Fig. 6c) in comparison with the changes of cosmic ray flux (solid line) and 10.7 cm solar irradiance (dashed line). The cloud data have complete global coverage, day and night, and are smoothed using a 12-month running mean to allow easy comparison with Fig. 5.

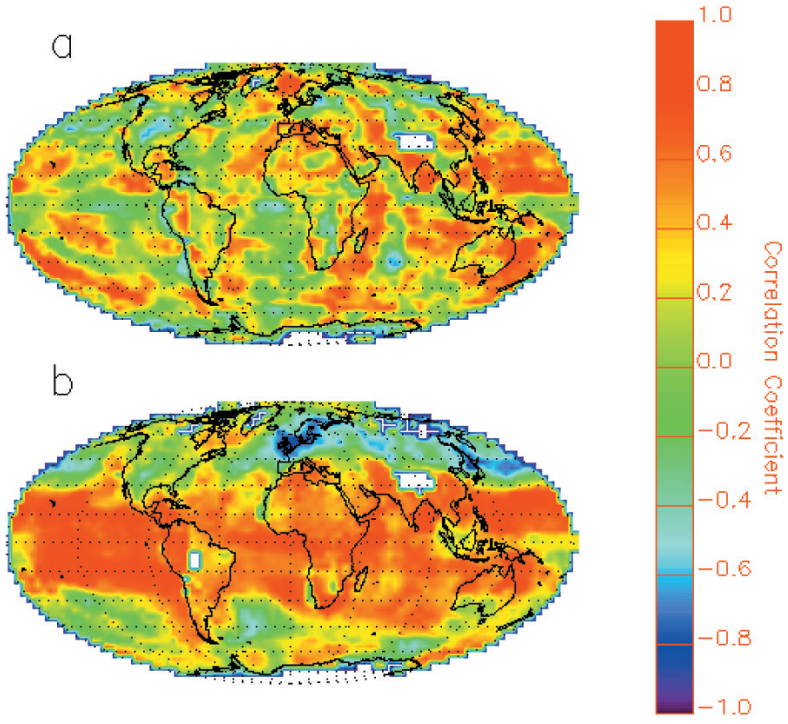

Figure 8: Global maps of the correlation between cosmic ray intensity and a) low IR cloud fraction and b) low IR cloud-top temperature [33]. The low IR cloud fractions are calculated as in Fig. 6c), while the low cloud-top temperatures are obtained from the ISCCP-D2 IR model. White pixels indicate regions with either no data or an incomplete monthly time series. The correlation coefficients are calculated from the 12-month running mean at each grid point. Fractions of the Earth with a correlation coefficient ≥ 0.6 are a) 14.2%, and b) 29.6%, respectively. The probability of obtaining a correlation coefficient ≥ 0.6 from a random signal is $< 0.01\%$ per pixel.

2.6 Effect of clouds on the Earth's radiation energy budget

The net radiative properties of a cloud are mainly dependent on its altitude and optical thickness. Optically-thin clouds at high and middle altitudes cause a net warming due to their relative transparency at short wavelengths but opacity in the IR region, whereas thick clouds produce a net cooling due to the dominance of the increased albedo of shortwave solar radiation. Since the data of Fig. 6 indicate that the solar modulation appears in the low clouds, the *sign* of the cosmic-climate effect is now known: increased cosmic rays are associated with increased low-clouds and therefore with a cooler climate.

Estimates from the Earth Radiation Budget Experiment (ERBE) indicate, overall, that clouds reflect more energy than they trap, leading to a net cooling of about 28 Wm^{-2} from the mean global cloud cover of 63% (Table 1) [35]. The observed absolute variation in low cloud cover of about 2% over a solar cycle (Fig. 6c) corresponds to about 7% relative variation. From Table 1, this would imply a solar maximum-to-minimum change in the Earth's radiation budget of about 1.2 Wm^{-2} (0.3% of the global average incoming solar radiation). This is a significant effect—comparable to the total estimated radiative forcing of 1.5 Wm^{-2} from the increase in CO_2 concentration during the last century.

Table 1: Global annual mean forcing due to various types of clouds, from the Earth Radiation Budget Experiment (ERBE) [35]. The sign is defined so that positive forcing increases the net radiation budget of the Earth and leads to a warming; negative forcing decreases the net radiation and causes a cooling.

Parameter		High clouds		Middle clouds		Low clouds	Total
		Thin	Thick	Thin	Thick	All	
Global fraction	(%)	10.1	8.6	10.7	7.3	26.6	63.3
Forcing (relative to clear sky):							
Albedo (SW radiation)	(Wm^{-2})	-4.1	-15.6	-3.7	-9.9	-20.2	-53.5
Outgoing LW radiation	(Wm^{-2})	6.5	8.6	4.8	2.4	3.5	25.8
Net forcing	(Wm^{-2})	2.4	-7.0	1.1	-7.5	-16.7	-27.7

2.7 History of cosmic rays and climate change

If the periodic 11-year cycles of the sunspots and the associated cosmic ray flux were the end of the story, then it would be of limited concern since there would be no resultant long-term change in the Earth's weather but simply another cyclic "seasonal" change (albeit with a period of 11 years and therefore heavily damped by the thermal mass of the oceans). However there is clear evidence of longer-term and unexplained changes both in the Sun's and in the Earth's magnetic behaviours and these, in turn, seem to have had long-term effects on the Earth's climate.

2.7.1 Global warming during the past century

The light radio-isotope record: Direct measurement of cosmic rays with particle detectors has been systematically carried out only during the last 50 years. However

there exists another reliable record of cosmic ray fluxes on Earth, which stretches back for at least 200 millennia: the light radio-isotope record [22, 36, 23]. Light radio-isotopes are continually created in the atmosphere by spallation of N and O atoms. The spallation interactions are induced mainly by low energy neutrons created in the secondary reactions of cosmic rays: protons, alphas and heavier particles. The two long-lived radioisotopes with the highest production rates are ^{14}C (half life = (5730 ± 40) years, and global mean production rate $\sim$2.5 atoms cm^{-2}s^{-1}) and ^{10}Be (half life = 1.5M years, global mean production rate $\sim 3.5 \times 10^{-2}$ atoms cm^{-2}s^{-1}).

In the case of ^{14}C atoms, they are rapidly oxidised to form $^{14}CO_2$. The turnover time of CO_2 in the atmosphere is quite short—about 4 years—mostly by absorption in the oceans and assimilation in living plants. However, recirculation from the oceans has the result that changes in the ^{14}C fraction on timescales less than a few decades are smoothed out. Plant material originally contains the prevailing atmospheric fraction of ^{14}C and, subsequently, since the material is generally not recycled into the atmosphere, the fraction decreases with the characteristic half life of ^{14}C.

In the case of ^{10}Be, after production it rapidly attaches to aerosols (solid or liquid) and follows the motion of the surrounding air masses. Since the production of ^{10}Be follows the intensity profile of the hadronic cosmic ray showers, about 2/3 is produced in the stratosphere and 1/3 in the troposphere, globally averaged. Due to the tropopause barrier, aerosols in the stratosphere take about 1–2 years to settle to the Earth's surface, whereas the mean residence time in the troposphere is only days or weeks. The removal mechanism is rain and snow, and so seasonal variations of precipitation may distort any measurements on timescales less than a year or so. In summary, despite a factor 100 lower production rate than ^{14}C, the advantages of ^{10}Be are that it settles out relatively rapidly ($\lesssim$ 2 years) and it is not re-circulated into the atmosphere. It is therefore sensitive to changes in the cosmic ray flux on short time scales of only a few years. On the other hand, ^{14}C has the advantages that it is not polar-centric and is independent of precipitation variability.

The change of cosmic ray intensity during the past century: Analysis of the ^{10}Be concentration in a Greenland ice core (Fig. 9) [36] reveals that the cosmic ray flux has been steadily decreasing over the course of the last century; it is weaker today at its *maximum* during the sunspot cycle than it was at its *minimum* around 1900. From refs. [22] and [23], we estimate the global average reduction of cosmic ray intensity to be about 15% over the last century (with a range of 10–25%). This estimate is supported by direct measurements of cosmic rays over the last 40 years made by the Lebedev Physical Institute using balloon-borne detectors (Table 2 and Appendix D.2) [37].

The cause of this systematic decrease in the cosmic ray flux during the last century has been a marked strengthening of the solar wind and the interplanetary magnetic field it carries into the heliosphere. This is revealed by the $<aa>$ geomagnetic index,[8] for which there is a continuous record extending back to 1868, covering 12 sunspot cycles. Lockwood *et al.* [2] have estimated the source magnetic flux, F_s, that leaves the corona and enters the heliosphere, from the level of geomagnetic activity seen at Earth in the $<aa>$ index.

[8]The $<aa>$ geomagnetic index is a sensitive measurement by two antipodal stations of short-term (3-hour interval) variations of the geomagnetic field at the Earth's surface [38], which is affected by the interactions of the solar wind with the Earth's magnetosphere.

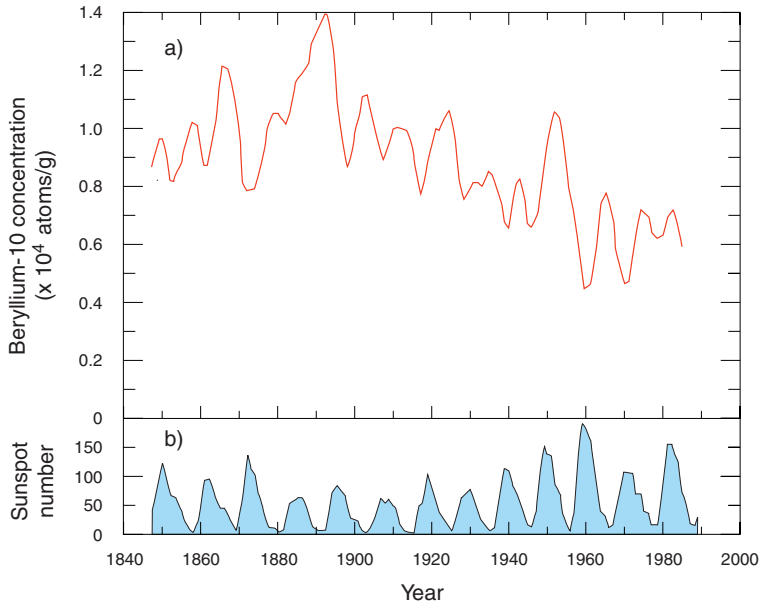

Figure 9: a) Concentration of ^{10}Be in a 300 m ice core from Greenland spanning the last 150 years [36]. The data are smoothed by an approximately 10 year running mean and have been shifted earlier by 2 years to account for settling time. b) The sunspot cycle over the same period, which shows a negative correlation with the short-term ($\sim$ 11 year) modulation of the ^{10}Be concentration.

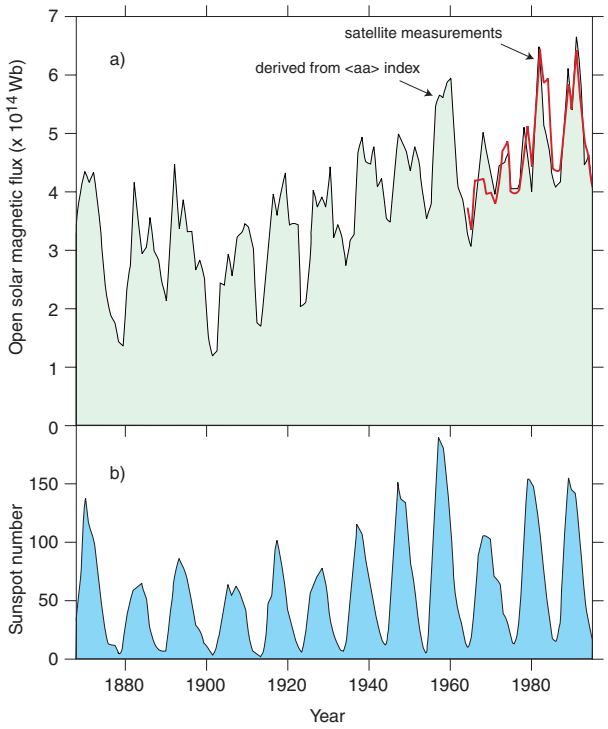

Figure 10: a) The total solar open magnetic flux (coronal source flux) derived from interplanetary observations for 1964–1996 (thick solid line) and derived from the <aa> geomagnetic index for 1868–1996 (shaded curve) [2]. b) The variation of the annual mean sunspot number.

Table 2: Decreases of the galactic cosmic ray intensity measured over the period 1957–1999 from balloon observations by the Lebedev Physical Institute [37]. An ∼11-year smoothing of the data was applied to filter out the periodic solar cycle modulation.

Station	**Location**	**Geomagnetic cutoff rigidity, $\mathbf{R}_c$ [GeV/c]**	**Cosmic ray decrease /10 years**
Murmansk	68.57N, 33.03E	0.6	2.3%
Moscow	55.56N, 37.11E	2.4	1.8%

This method to derive the coronal source flux has been successfully tested against near-Earth interplanetary space measurements made since 1963, during which time the coronal source flux of the Sun has been observed to rise a factor 1.4. In the period since 1901, Lockwood *et al.* [2] calculate the increase to have been a factor 2.3 (Fig. 10). The reason for this dramatic increase in the Sun's magnetic activity is a mystery.

We have estimated the change in cosmic ray intensity over the last 140 years using these coronal source flux data. Scattering, gradient and curvature drifts caused by the heliospheric magnetic field are the major contributor to the shielding of cosmic rays from the Earth and a very strong anti-correlation between cosmic ray fluxes with the heliospheric field near Earth was reported for the recent sunspot cycles 21 and 22 (Fig. 4). Thus an anti-correlation of the source flux F_s with cosmic ray fluxes is expected. This is seen in Fig. 11 which shows monthly mean counts, N, detected by the Climax neutron monitor in the interval 1953-1998 as a function of the annual estimates of F_s made by Lockwood *et al.*. The peak correlation (r = -0.874) is, essentially, 100% significant and is obtained with the cosmic ray fluxes lagged by one month. The line shows a linear regression fit to these data which can be used, along with the F_s data sequence, to extrapolate the cosmic ray flux variation back to 1868. The percent variation of the cosmic ray flux (relative to the average value for solar cycle 21) derived this way is shown by the solid line in Fig. 12. This extrapolation predicts a fall in the average cosmic ray fluxes of about 20% since 1900 for Climax (3 GeV cutoff), which implies about 15%, globally averaged, in agreement with the estimates given above. This change can be compared with the ^{10}Be isotope record in ice sheets. The inferred cosmic ray variation is plotted as a dashed line in Fig. 12 and the long-term changes agrees well with the variation inferred from F_s.

If the cosmic-cloud link is real then this reduction of cosmic ray intensity implies a net positive radiative forcing equivalent to about one solar cycle, i.e. +1.2 Wm^{-2} (Section 2.6) over the past century. In short, a systematic decrease in the cosmic ray flux of the magnitude indicated by the ^{10}Be and coronal magnetic flux measurements could have caused a reduction in cloud cover and consequent warming of the Earth comparable to the observed rise of 0.6°C in global temperatures last century, which is presently attributed predominantly to anthropogenic greenhouse gases.

2.7.2 Climate change over the last millennium

The observations of a correlation between the Sun's activity, cosmic rays and the Earth's climate can be extended to earlier times with either ^{10}Be or ^{14}C data. The latter agree

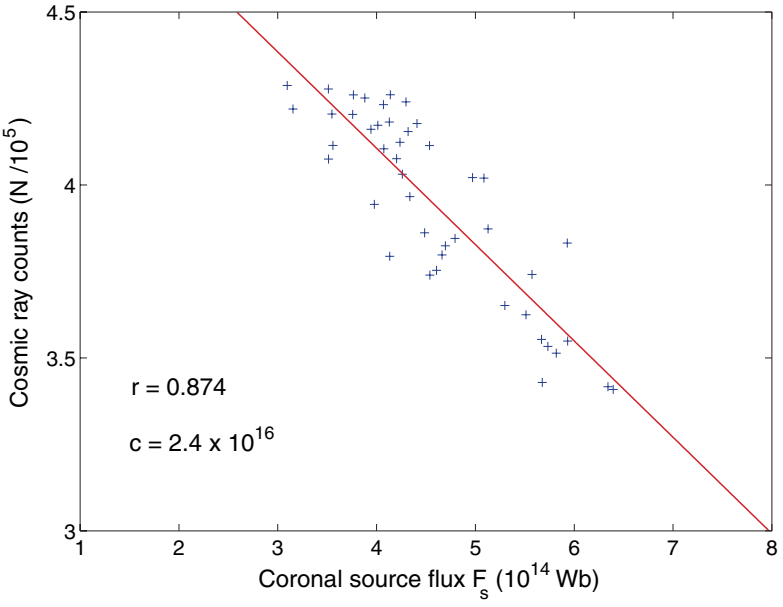

Figure 11: The negative correlation of annual means cosmic ray counts, N, observed at Climax (cut-off 3 GeV) and the coronal source flux, F_s (as estimated from geomagnetic observations). The peak correlation coefficient is $r = -0.874$, with the cosmic ray data lagged by one month. The probability of arriving at this result by chance is $c = 2.4 \cdot 10^{-16}$. The solid line is the best linear regression fit.

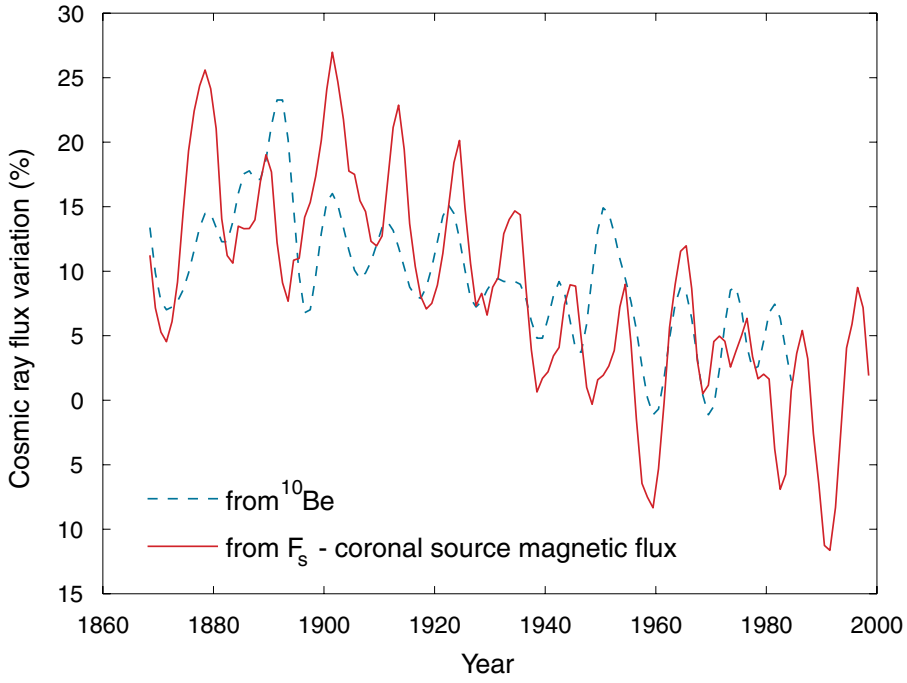

Figure 12: The estimated changes in the cosmic ray flux over the last 140 years. The solid line is the per cent variation (relative to the mean value for solar cycle 21) derived from the linear regression of cosmic ray fluxes with the coronal source flux. The dashed line is the variation derived from observations of the ^{10}Be isotope concentration found in a Greenland ice core.

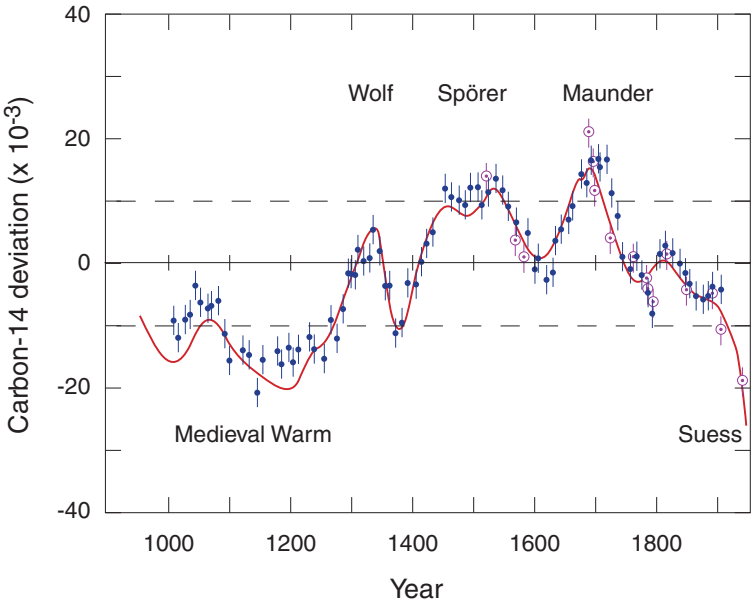

Figure 13: History of deviations in the relative atmospheric ^{14}C concentration from tree-ring analyses for the last millennium [39]. The data points (dots and open circles) are two independent high-precision measurements. The solid curve represents a combined fit to a large number of other measurements of medium precision. The dashed lines indicate ^{14}C deviations of 10 parts per mil. The first four labelled periods correspond to recorded climatic anomalies. The sharp negative ^{14}C deviation during the present century is the Suess effect, due to the burning of ^{14}C-depleted fossil fuels.

well with ^{10}Be data after accounting for a lag of ∼50 years in the ^{14}C data due to the effects of re-circulation from the oceans [36].

By analysing the ^{14}C content in the rings of long-lived trees such the Californian bristlecone pine, a year-by-year record has been assembled of the cosmic ray flux on Earth over the past several thousand years. The data for the last 1000 years are shown in Fig. 13 [39]. The periods where the ^{14}C deviation approaches or exceeds 10 parts per mil correspond to recorded climatic anomalies: a) 1000–1270, the so-called Medieval Warm period, b) 1280–1350, the Wolf minimum, c) 1420–1540, the Spörer minimum, and d) 1645–1715, the Maunder minimum. The warm period that lasted until about 1300 enabled the Vikings to colonise Greenland and wine making to flourish in England. It was followed by a period of about 500 years during which—save for a few short interruptions—the glaciers advanced and a cooler, harsher climate predominated.

The Maunder Minimum, when there was an almost complete absence of sunspots, corresponded to a high cosmic ray flux on Earth and therefore, under the present hypothesis, to an increased cloudiness. This provides a consistent explanation for the exceptionally cold weather during this period. Indeed, in every case the lack (a) or excess (b–d) of ^{14}C is consistent with the hypothesis of a higher cosmic ray flux leading to more clouds and cooler temperatures, and vice versa.

Evidence has recently been presented that this climate pattern extended into the equatorial regions, and is therefore likely to have been a global phenomenon. Figure 14 shows the correlation of the ^{14}C record with the depth and salinity of a lake in equatorial East Africa over the last 1100 years [40]. The reconstruction is based on three indepen-

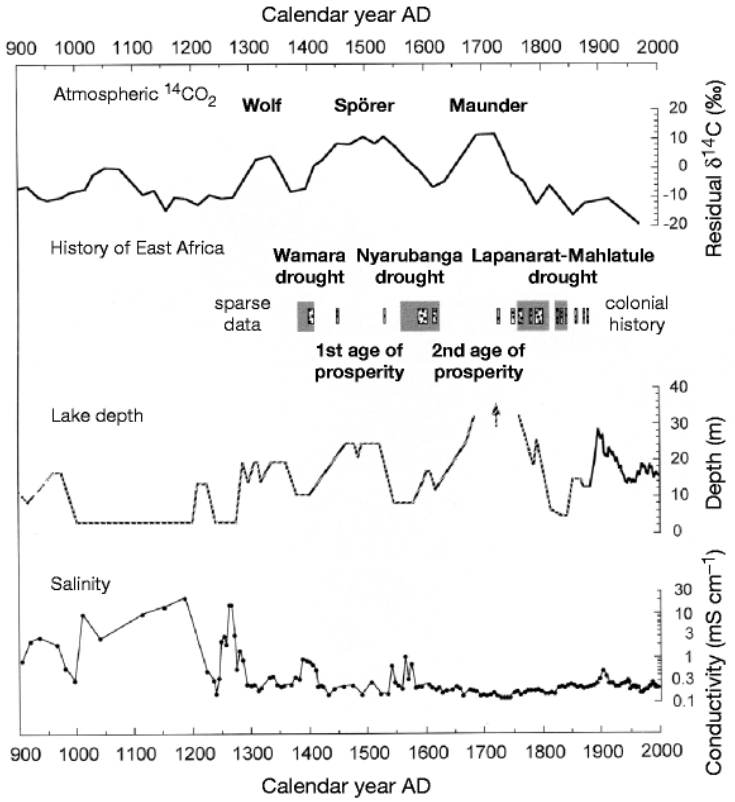

Figure 14: History of rainfall and drought in equatorial east Africa during the last 1100 years [40]. The central and lower figures show the reconstructed depth and salinity, respectively, of Crescent Island Crater lake (Kenya). The radiocarbon dating error for the lake data is ±50 y. The upper figure shows the atmospheric ^{14}C deviation over the same period. Grey bars indicate evidence of drought-related political upheaval recorded in oral tradition, genealogically dated using a 27-yr dynastic generation. Dotted bars compile the evidence of severe drought periods from various archival records.

dent palaeolimnological proxies: sediment stratigraphy and species compositions of fossil diatoms and midges. These data not only confirm the presence of the major climatic anomalies associated with the Medieval Warm period and the Wolf, Spörer and Maunder minima but also identify three extended drought periods between the minima: AD 1390–1420, 1560–1625 and 1760–1840. The agreement with the ^{14}C record is striking. The cultural history of the region, recorded in documents and oral tradition, coincides with the experimental data (see Fig. 14). In the present hypothesis, the periods of high cosmic ray flux would have corresponded to increased cloudiness. Under the assumption that increased cloudiness implies increased cloud lifetime, the rainfall would have decreased but at the same time the evaporative losses would have decreased. Which of these opposing effects would dominate depends on latitude and other regional effects.

These and earlier historical examples of climate anomalies provide strong evidence for solar variability and its coupling with the climate. One possible interpretation of the ^{14}C data is that they provide a proxy for changes in the solar irradiance, and that this was the actual cause of the climate change. The alternative possibility is the mechanism

addressed in this proposal, namely that the coupling is through the solar wind, cosmic rays and clouds. Regardless of the mechanism, however, there is little doubt that the Earth has experienced several extended warm and cold spells over the last 1000 years—and indeed at earlier times—with climate swings comparable to the recent warming but which could not be due to anthropogenic greenhouse gases. Whatever mechanism caused those earlier changes in the climate could perhaps be at work today.

In summary, there are two main conclusions to be drawn from the historical record of cosmic rays and climate change. Firstly, the pattern of systematic change in the global climate over recorded history seems to follow the observed changes of cosmic ray flux; and it is consistent with the explanation that a low cosmic ray flux corresponds to fewer clouds and a warmer climate, and vice versa. Secondly, there has been a systematic decrease of the cosmic ray flux by about 15% over the course of the last century, caused by a doubling of the solar coronal source magnetic flux. The rise of about 0.6°C in global temperatures over the last 100 years is consistent in magnitude and time dependence with the observed changes in cosmic ray flux—and thereby cloud cover—over the same period. If the cosmic-cloud link is confirmed then it provides a new mechanism for climate change that may significantly revise the estimated contribution to global warming from anthropogenic greenhouse gases. A clear and compelling case exists to investigate the causal link between cosmic rays and clouds.

3 Goals of the CLOUD experiment

3.1 Scientific goals

The primary scientific goals of the CLOUD experiment are as follows:

1. To study the link between cosmic rays and the formation of large ions, aerosol particles, cloud droplets, and ice crystals.

2. To understand the microphysical mechanisms connecting cosmic rays to changes in aerosol and cloud particle properties.

3. To simulate the effects of cosmic rays on aerosol and cloud properties under atmospheric conditions.

Concerning the last item, particular care will be taken to assess whether cosmic ray variations could have a significant effect on cloud properties within the natural variability of other factors. Where significant effects are found, we will attempt to provide the climate modelling community with simplified parameterisations of changes in key properties of individual clouds. This will enable the influence of cosmic rays on clouds to be incorporated into GCMs (general circulation models) and an evaluation made of their contribution to the global radiative forcing over the last century (see Fig. 1).

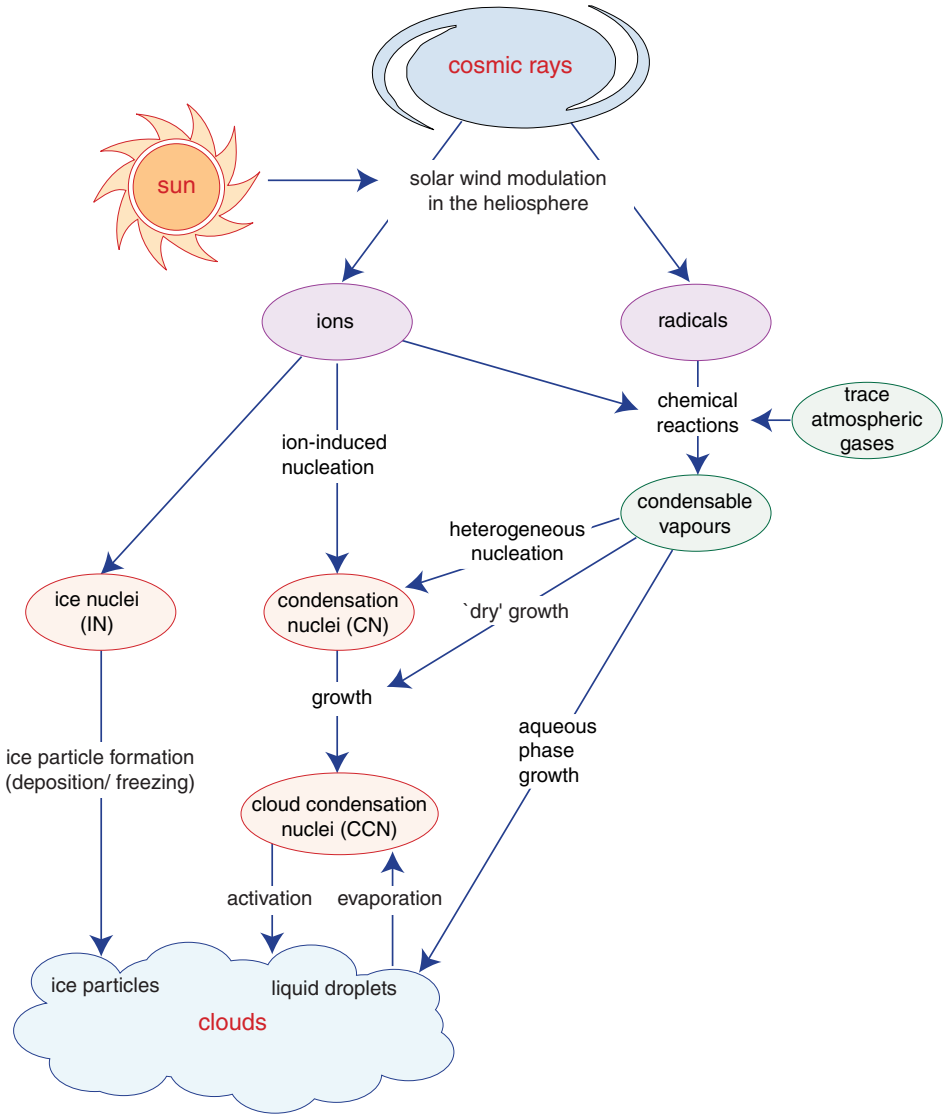

Figure 15: Paths that may connect cosmic rays to clouds and hence link solar and climate variability through the solar wind modulation. The processes are described in Section 3.2.

3.2 Paths connecting cosmic rays and clouds

Atmospheric clouds are highly complex and can be affected by a wide range of environmental parameters. At the simplest level, the development of a single small cumulus cloud is influenced by small changes in the temperature structure of the atmosphere, changes in humidity and surface heating rate. At a more complex level, the number of cloud droplets that form and their size distribution are affected by the composition and sizes of the aerosol particles upon which the water vapour condenses (Appendix A). There is also an enormous variety of cloud types, whose properties depend on the specific environmental conditions under which they form and develop.

This complexity makes it difficult to make a straightforward connection between cosmic ray flux and cloud behaviour. Our approach in the CLOUD experiment is to:

1. Identify a number of key aerosol and cloud properties that might be affected by

cosmic rays.

2. Experimentally determine the effects of cosmic rays under constrained laboratory conditions relevant to the atmosphere.

3. Incorporate the experimental results in computer models of aerosol and cloud processes.

4. Simulate the behaviour of natural clouds with a variable cosmic ray rate to determine which cloud properties are sensitive to these variations.

If aerosols can influence clouds, it is likely to be through their effects on aerosols or on ice nucleation. Aerosols are found throughout the atmosphere and constitute efficient cloud condensation nuclei (CCN) for activation of cloud droplets (Appendix A). The presence of a largely abundant supply of CCN ensures that the maximum water vapour supersaturations in the atmosphere rarely exceed values of about 1% since higher values are arrested by the removal of water vapour during droplet growth.

We have identified four distinct ways in which cosmic ray ionisation could, either directly or indirectly, affect clouds in the troposphere. The mechanisms are summarised in Fig. 15 and described individually in Sections 3.2.1–3.2.4 below. It is also possible that cosmic rays influence aerosol processes in the stratosphere, as discussed in Section 3.2.5.

3.2.1 Enhanced aerosol nucleation and growth into cloud condensation nuclei

Cosmic rays create ions in the troposphere, which may affect aerosol microphysical processes. Figure 16 shows a simplified set of atmospheric pathways that might connect variations of atmospheric ionisation with changes in the CCN abundance. The unbroken arrows indicate processes that are known to occur in the atmosphere. The arrows labelled 'GCR' are processes whose *rate* may be affected by ionisation. The most important processes affected are likely to be aerosol nucleation and aerosol particle growth either by condensation or by coagulation.[9] Clouds that form in air containing high CCN concentrations tend to have high droplet concentrations, which enhances the shortwave (solar) albedo. Increase in the CCN concentration also inhibits rainfall and therefore increases cloud lifetimes (cloud coverage). These effects—which are due to more, smaller droplets at a fixed liquid water content—are particularly significant in marine air, where the CCN concentrations are generally quite low.

The possible cosmic ray influence on CCN abundance indicated in Fig. 16 is similar to, but not the same as, the so-called *aerosol indirect effect* on clouds and climate. The aerosol indirect effect concerns changes in the *supply* of the aerosol material (such as SO_2 in Fig. 16), which subsequently causes a change in the CCN abundance and hence cloud droplet concentrations. In the *cosmic ray–aerosol–cloud* indirect effect, which we propose to study, the cause of a change in CCN abundance would be changes in the *rates* of certain aerosol transformation processes.

It has been long speculated that atmospheric sulphate particles are formed by ion-induced nucleation (see, for example, refs. [41, 42] and references quoted therein). Also,

[9] *Nucleation* refers to the creation from vapours of a small (∼1 nm diameter), stable molecular cluster (aerosol) of a few tens or hundreds of molecules. *Coagulation* is the growth of an aerosol population by particles colliding and sticking together.

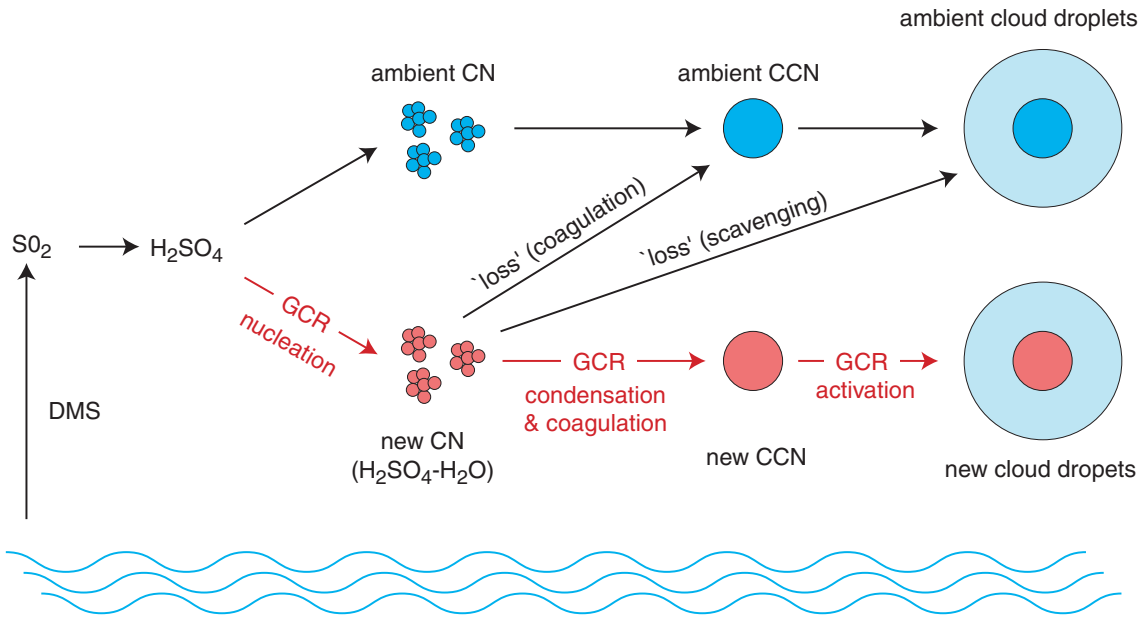

Figure 16: Possible influence of galactic cosmic rays (GCRs) on the nucleation of new condensation nuclei (CN) and on the growth into cloud condensation nuclei (CCN), ultimately causing an increase in the concentration of cloud droplets. The arrows labelled 'GCR' are processes whose rate may be affected by cosmic rays. Dimethyl sulphide (DMS) from plankton is the major source of sulphur dioxide—the precursor of sulphuric acid—in remote marine environments.

processes such as ion-ion recombination have been proposed which lead to the production of stable molecular clusters in the lower stratosphere [43] and in the troposphere [4, 5]. Since the nucleation rate of new aerosols from these processes is proportional to ion concentration, variations of the cosmic ray flux may translate into variations of aerosol particle concentrations and, ultimately, CCN concentrations. Recent experimental data suggest that ions may indeed be involved in gas-to-particle conversion. Hõrrak *et al.* [44] reported the spontaneous formation of bursts of intermediate size ions in urban air, which they suggest may be due to ion-induced nucleation. The Helsinki group has made similar observations of aerosol bursts in unpolluted marine air [45] and in remote continental air [46].

Although the ion-induced nucleation phenomenon has been studied for more than 100 years, it remains poorly understood, both experimentally and theoretically. For example, the classical theory describes the charge effect on nucleation by an electrostatic interaction term between the ion and condensing molecules. However, this term does not explain the ion sign preference exhibited by many molecules (e.g. water molecules nucleate more easily on negative ions) which was experimentally found already by Wilson in 1899 [47]. The sign preference has been attributed to surface orientation of dipolar molecules [48, 49], and a partial theoretical understanding has been proposed [50].

There is new evidence that increases in CCN concentration can indeed suppress rainfall, and hence increase cloud lifetime. A recent study [51] used NOAA satellite data to investigate clouds that formed downwind of industrial sites located in pristine areas.

The otherwise uniform cloud data from these regions was streaked with bright (highly reflective) plumes from the industrial sites. The droplets in these plumes were found to be more numerous than the nearby regions and of a smaller diameter—typically less than 10μm and therefore below the threshold size for them to coalesce efficiently and precipitate. In contrast the droplets outside the plumes measured more than 25 μm in diameter. The high reflectivity of the plumes resulted from the high droplet number density at fixed liquid water content (Fig. 47). Independent analysis of data from the Tropical Rainfall Measuring Mission confirmed that these plumes did indeed produce less rain and therefore had a longer lifetime than clouds in the nearby regions. These observations suggest that, if increases in cosmic ray flux could be translated into increases in CCN abundance, the observed increases in cloudiness (Fig. 7) could be due to decreases in precipitation efficiency.

3.2.2 Enhanced cloud condensation nucleus activation by charge attachment

Aerosol activation is the rapid growth of an existing aerosol into a large ($\gtrsim$1 μm) liquid droplet by condensation of water from a supersaturated vapour. If aerosol charging (induced by cosmic ionisation) could decrease the supersaturation needed for activation, this would lead to an increase in droplet number densities in clouds, with consequences for all cloud microphysical processes.

The possible effect of charges on aerosol activation has usually been ignored since the conventional electrostatic interaction term is expected to be appreciable only for very small aerosols of $\sim$1 nm diameter for small charges (see Appendix C). However, a recent study [52] on heterogeneous nucleation of n-butanol vapour on charged and uncharged insoluble particles shows a surprisingly large charge effect. The charges have a clear effect on the nucleation process even when the seed particles are as large as 90 nm in diameter and the supersaturation is only 0.5%. For these experiments the classical theory predicts that the difference in the nucleating ability of charged and uncharged seed particles should vanish for particle diameters above 20 nm, corresponding to supersaturations of about 100%. If this result is correct, it indicates that charges may play a role in atmospheric cloud drop activation processes, at least when the CCN are partially insoluble (e.g. carbon) and carry multiple charges. Furthermore, the charges could influence the condensation of low vapour pressure trace gases on aerosol particles, and thereby affect the processes transforming CN into CCN.

3.2.3 Formation of condensable vapours and the effect on cloud condensation nuclei

The ions and radicals, together with trace atmospheric gases, may promote the formation of condensable vapours or enhance the condensation of vapours already present, which can lead to the growth of existing aerosols (Appendix B). The condensation may occur on unactivated aerosols or on cloud droplets (aqueous phase growth), which would result in larger aerosol mass after evaporation of the water. Growth of aerosols can lead to a higher CCN number concentration, and to CCN that activate into droplets at lower supersaturations. The free radicals created by cosmic rays may also be able to influence atmospheric chemistry under certain conditions, especially if catalytic reactions are involved or where cosmic rays constitute a significant source of a chemical species [53, 54].

The most important radicals created by cosmic rays are N, O, and OH from the dissociation of the primary active constituents of air: N_2, O_2 and H_2O. The estimated production rates are about 1–2 hydroxyl (OH) molecules per ion-pair [53] and 1.5 nitric oxide (NO) molecules per ion-pair [55, 56, 57]. These rates imply mixing ratios of about 0.7 pptv NO are generated per day by cosmic rays directly in the upper troposphere. After oxidation to nitric acid this may affect the growth of both CN and CCN (Fig. 17).

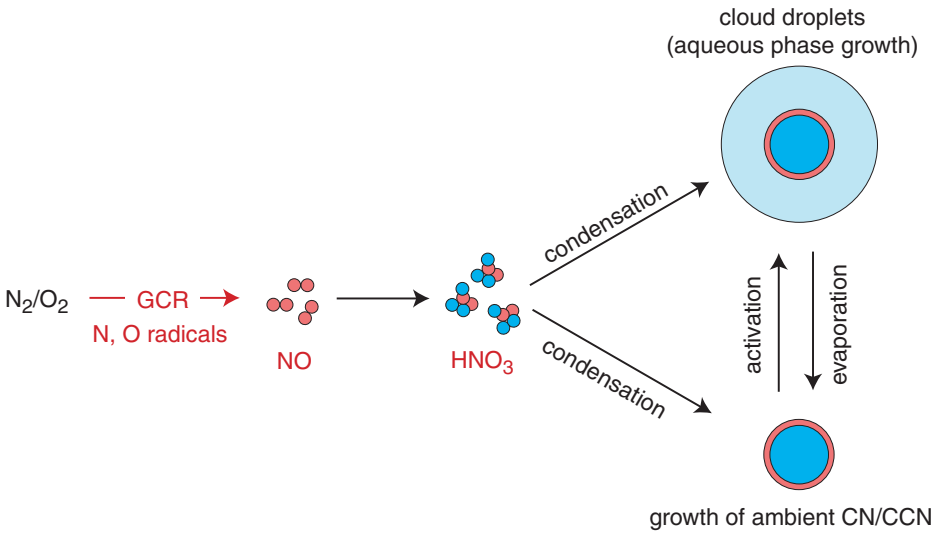

Figure 17: Possible influence of galactic cosmic rays on the production of new condensable vapours and subsequent growth of existing CN and CCN.

Although the production of NO by cosmic rays is small on a global basis, it may be the dominant source in the upper troposphere of remote regions [55, 56]. Experimental evidence for the importance of particle ionising radiation for NO production is demonstrated by a clear nitrate signal in the Greenland ice core associated with solar proton events and the solar cycle [58, 59]. Calculations indicate that galactic cosmic rays may be responsible for about half of the NO in the polar stratosphere, and may be the dominant source during the polar winters when N_2O oxidation is suppressed [54, 56].

3.2.4 Creation of ice nuclei

The presence of ice in clouds has an important influence on their radiative properties and it can also lead to precipitation. However the apparent lack of ice nuclei (IN) in the atmosphere is at present a mystery: there is about 1 IN per litre at 253 K (compared with about 10^6 aerosol particles per litre) whereas the observed concentrations of ice particles in clouds at these temperatures vary between 10 and 300 per litre. Two nucleation processes can lead to ice formation: a) direct sublimation of vapour to the solid phase (deposition nucleation) and b) freezing of a liquid droplet (freezing nucleation). It has been suggested that the ionisation produced by cosmic rays may be able to affect both deposition and freezing nucleation (Fig. 18).

The possible effect of charges on ice nucleation has been studied to some extent (see Pruppacher and Klett [60] for a review), and effects have been seen in a number of experiments. Especially, the ice nucleating ability of various types of seed particles seems

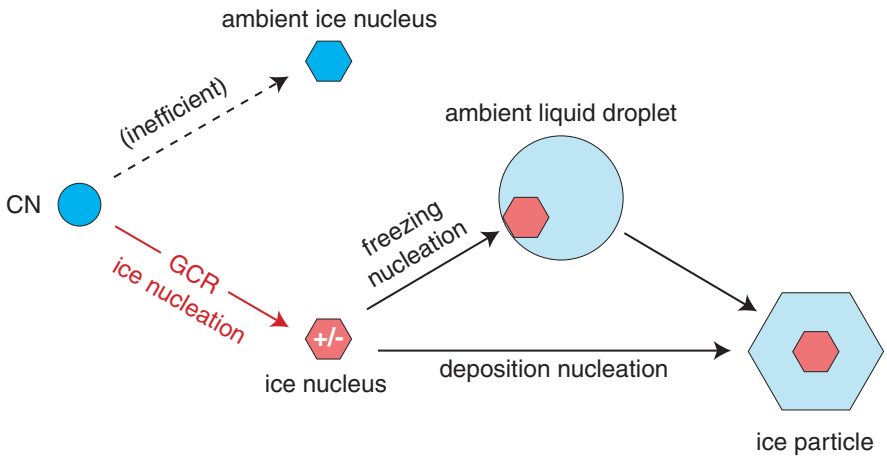

Figure 18: Possible influence of galactic cosmic rays on the creation of ice nuclei (IN) and ice particles at temperatures below 273 K.

to be influenced by ionisation. It is interesting to note that cloud chamber experiments at the University of Missouri-Rolla in 1980 [61] found an enhancement of frozen droplets in the regions where cosmic rays traversed the cloud chamber (Fig. 19)—although it was not possible to determine if the cosmic rays preceded or followed the droplet formation. The presence of ions was observed to raise the threshold temperature for homogeneous ice nucleation by about 2 K.

Enhancing heterogeneous ice nucleation by electrification has been proposed by several workers in the context of solar-terrestrial climate connections. It is supported by very little experimental work so far [60]. If the electrofreezing effect [7] is real, possible influences of cosmic rays on cirrus formation and on the properties of middle clouds are implied. Electrofreezing could also affect glaciation (which triggers rain) in convective clouds. This may in some way be related to the correlation between cosmic rays and precipitation [26].

3.2.5 The effect of cosmic rays on stratospheric clouds and ozone depletion

The previous four processes have concerned aerosols and clouds in the troposphere. However, cosmic ray intensities are even higher in the stratosphere, so it is conceivable that they also have an influence on aerosol processes in that part of the atmosphere [62].

Chemical reactions on stratospheric aerosols are a prerequisite for seasonal ozone depletion in both the Arctic and Antarctic stratosphere [63]. These reactions convert relatively inert inorganic chlorine compounds into photochemically labile forms that can enter into ozone-destroying gas-phase catalytic cycles. The formation of *polar stratospheric clouds* in the low temperature polar stratosphere dramatically accelerates the rate of these reactions, leading to the formation of the ozone hole.

Significant advances have been made in our understanding of polar stratospheric cloud formation in the last 10–15 years [64, 65]. However, there remain important uncertainties that prevent a reliable prognosis of ozone depletion rates in a given winter or in future years. Chief among these uncertainties is what controls the *phase* (liquid or solid) of polar stratospheric cloud particles. At temperatures above the ice frost point the particles may

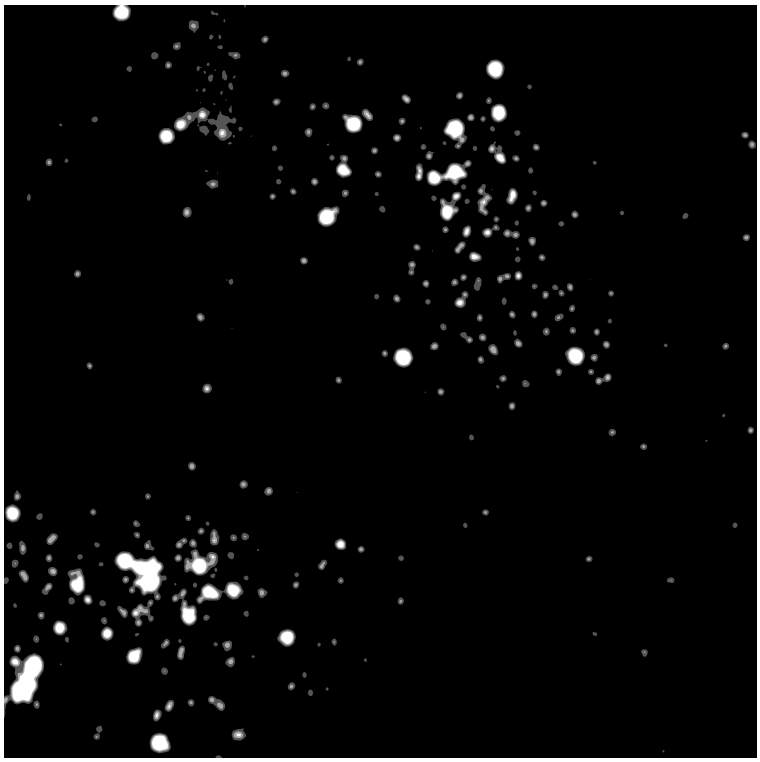

Figure 19: Ice and liquid water droplets observed together in a cloud expansion chamber at 230 K. The two clusters correspond to regions of ionisation due to cosmic rays that crossed roughly along the direction of view. The ice droplets visibly scatter more light than the liquid droplets, and appear larger. In fact the large apparent size of the ice crystals is probably the result of light scattering in the emulsion film. The field of view in this image is about 17 mm across and about 10 mm in depth. The data were obtained at the University of Missouri-Rolla in 1980 [61].

be either liquid solutions of nitric acid, sulphuric acid and water or else solid hydrates of nitric acid. The formation of solid hydrates is important because it allows the selective growth of a small number of particles that subsequently become large enough to sediment out of the stratosphere. This process leads to *denitrification* of the polar stratosphere and often to strongly enhanced ozone loss (see ref. [66] and and references therein).

Several mechanisms are recognised to be important for the formation of solid polar stratospheric clouds particles [64, 67]. However, persistent and optically very thin clouds, often seen over several thousand kilometer regions cannot be explained by any recognised mechanism. These tenuous hydrate clouds appear to be formed by a mechanism that operates on a very large scale with little spatial variability, thus excluding formation mechanisms involving localised cooling [68]. Laboratory experiments also exclude the possibility that these solid particles form by crystallisation of the liquid aerosols [69] by large scale cooling. An intriguing possibility—so far unexplored—is that these clouds form by deposition nucleation of nitric acid and water directly on cosmic ray-generated ions or ion clusters. However, to date, there have been no experiments that can confirm or dispute this possibility. An understanding of such particles appears to be critical to a complete understanding of denitrification and ozone loss.

3.3 Experimental concept

The essential approach of CLOUD is to test the link between cosmic rays and cloud formation under controlled laboratory conditions in a particle beam, which provides an adjustable and collimated source of "cosmic rays". The detector is based on an expansion cloud chamber that is designed to duplicate atmospheric conditions. This requires the capability of producing the very low water vapour supersaturations[10]—typically a few tenths of a percent—found in clouds, so that the precise cloud-forming properties of the air parcel under study can be measured.

The advantage of this approach is that all the experimental conditions can be precisely controlled and measured. In particular, by comparing measurements at several beam intensities from zero up to high values, we can determine if there is a causal relationship between ionising radiation and cloud formation. Such measurements are difficult to perform with cosmic rays in the atmosphere since the natural intensity variations are modest and they follow the slow 11-year solar cycle. Furthermore, the CLOUD experiment provides full control of the initial gas mixture and aerosol content and, in addition, complete physical and chemical analysis of the final products after beam exposure. This will greatly facilitate an understanding of the microphysics and chemistry of any observed effects. The challenges of the laboratory-based approach are to precisely duplicate the atmospheric conditions and to ensure that the finite volume (walls) of the cloud chamber does not affect the measurements.

Surprisingly, cloud chamber data under atmospheric conditions in a particle beam have never been previously obtained. C.T.R. Wilson's cloud chamber[11] [70, 71] was extensively used for experimental particle physics in the first half of the 20th century, but was mostly operated under conditions far removed from those of the atmosphere. In order to grow droplets on the small ions produced by ionising radiation, Wilson cloud chambers were operated with water vapour supersaturations of 500–600%, to be compared with maximum values of about 1% in atmospheric clouds (see Appendices A and C). However, it is interesting to note observations made in cloud chambers in the 1960's of backgrounds due to "hypersensitive condensation nuclei" [72]. These activated into droplets at very low water vapour supersaturations—of order 1%—and were attributed to trace amounts of NO_2 vapour created by electrostatic discharges.

3.4 Initial experimental programme

The initial CLOUD experimental programme and operating conditions are summarised in Table 3. It is important to note that our experimental search is quite broad since at

[10]Water vapour supersaturation, $SS = S - 1 = p/p_0 - 1$, where S is the saturation ratio, p is the ambient partial pressure of water vapour and p_0 is the saturated vapour pressure over a plane surface of water at this temperature. Supersaturation is frequently expressed as a percentage.

[11]Wilson had the inspiration for the cloud chamber while observing meteorological phenomena on the mountain of Ben Nevis in 1894. The phenomena were not particle tracks, however, but "coronas" around the Sun and glories, where the Sun glows around shadows in the mist. He developed the cloud chamber to try to reproduce these effects in the laboratory. Although his expansion cloud chamber was crucial to the development of nuclear and particle physics for the next half century and earned him the 1927 Nobel Prize in Physics, Wilson remained fascinated by atmospheric phenomena throughout his life [71]. Indeed, he devoted a large part of his later research life to seeking a connection between cosmic rays and clouds. We are therefore glad to propose a Wilson cloud chamber for this experiment.

Table 3: Initial CLOUD experimental programme and operating conditions.

	Experiment	**Aerosols[†] / Trace gases**	**Size [nm] or Conc. [ppb]**	**P [mb]**	**T [K]**	**H_2O**
I. Creation & growth of aerosols:						
1.	Sulphuric acid	H_2SO_4	0.0001-1 ppb	1000	270-300	20-80[‡]
2.	" + Ammonia	" + NH_3	+0.001-0.1 ppb	1000	270-300	20-80[‡]
3.	Sulphur dioxide	SO_2	0.0001-1 ppb	1000	270-300	20-80[‡]
4.	Sodium chloride	NaCl	5-50 nm	500-1000	260-300	0.1-1[§]
5.	Ammonium sulphate	$(NH_4)_2SO_4$	5-50 nm	500-1000	260-300	0.1-1[§]
6.	" + Nitric acid	" + HNO_3	0.1-100 ppb	500-1000	260-300	0.1-1[§]
II. Activation of aerosols into droplets:						
7.	Sodium chloride	NaCl	50-100 nm	500-1000	260-300	0.1-1[§]
8.	Ammonium sulphate	$(NH_4)_2SO_4$	50-100 nm	500-1000	260-300	0.1-1[§]
9.	" + Nitric acid	" + HNO_3	0.1-100 ppb	500-1000	260-300	0.1-1[§]
III. Formation of condensable vapours:						
10.	NO_x	N_2:0_2	pure 80%:20%	500-1000	260-300	0.1-500[§]
IV. Creation of ice nuclei:						
11.	Pure water	none	10 μm droplets	200-1000	213-273	1-50[⋆]
12.	Ammonium sulphate	$(NH_4)_2SO_4$	10 μm droplets	200-1000	213-273	1-50[⋆]
13.	Sulphuric acid	H_2SO_4	10 μm droplets	200-1000	213-273	1-50[⋆]
V. Stratospheric aerosols:						
14.	Nitric acid	HNO_3	10-20 ppb	10-100	190-200	5 ppm

[†] Aerosol number concentration: $\sim$500 cm^{-3}.
[§] Supersaturation [%] relative to liquid water, during activation.
[‡] Relative humidity [%] during beam exposure.
[⋆] Supersaturation [%] relative to ice.

present there is no clear microphysical explanation of the possible cosmic-cloud link. We therefore expect to adapt our investigations according to our experimental observations and to the current experimental and theoretical developments at the time of taking data. The initial experimental programme described here should therefore be considered as representative rather than definitive.

Each experiment will in general be performed with two different carrier gases: a) pure Ar (inert carrier), b) pure artificial air (80% N_2, 20% 0_2). The cloud-forming properties and other physical and chemical characteristics of the aerosols will be measured under beam/no-beam conditions using a range of equipment described in Section 4.

In the following subsections we outline some of the experiments required to explore the mechanisms described in Sections 3.2.1–3.2.5.

3.4.1 Aerosol nucleation and growth experiments

These studies concern the formation of aerosols from the vapour phase, via ion-induced nucleation, and their subsequent growth by vapour condensation and coagulation.

We will investigate the clustering of trace gas molecules onto ions. The trace gas molecules will either be formed by the ionising particle beam in pure artificial air or be introduced directly into the chamber. Such trace gas molecules include, in particular, H_2O, H_2SO_4, HNO_3, NH_3 and certain volatile organic compounds. These trace gases will be measured by CIMS (Chemical Ionisation Mass Spectrometry), and the ions will be measured by ion mass spectrometers and ion mobility analysers. During activation measurements in the cloud chamber a fairly high supersaturation (large expansion) will be required, depending on the size and nature of the nucleated aerosols.

A major goal of these studies is to find out what fraction of the small ions created by ionising radiation become stable aerosol particles. This fraction f will increase with decreasing temperature T and with increasing abundance of the clustering trace gas molecules. For example, in the case of H_2SO_4/H_2O ion clusters, f is expected to increase with increasing relative humidity and relative acidity. However, for low H_2SO_4 concentrations a kinetic limitation becomes important which is related to the limited ion-ion recombination lifetime t_{IR}. It is therefore important to work under well-controlled conditions with respect to the total ion concentrations n_i and thereby t_{IR} on the one hand and the sulphuric acid concentration $[H_2SO_4]$ on the other. Both n_i and $[H_2SO_4]$, along with $[H_2O]$ and T, must be precisely known and adjustable.

The link proposed in section 3.2.1 between aerosols and clouds includes also a charge-enhanced growth of aerosols from small size (Aitken mode, 20–100 nm diameter) into the cloud-condensation nuclei (CCN) mode ($\gtrsim$100 nm) where they can efficiently activate to form cloud droplets. We will start with a study of aerosols that are common in the atmosphere and known to be important in cloud formation such as NaCl, $(NH_4)_2SO_4$ and H_2SO_4. Both "dry" and aqueous-phase growth will be studied. We will begin with well-known, simple systems to first confirm that the apparatus is well understood. This involves measurements with monodisperse NaCl or $(NH_4)_2SO_4$ aerosols of diameter 10 nm, followed by 20 nm and then 40 nm. Then a second or third vapour component will be added and more complex systems studied.

Comparisons will be made with and without beam. Since diffusion of small ions is significant for beam exposures longer than about a minute (Section 5.4.3), the with/without

beam measurements will be made in separate runs. Because of their relatively small mobility, the loss of aerosol particles to the walls of the cloud chamber is rather slow (Section 5.4.2) and, depending on the specific conditions, growth processes lasting 1–10 hours or more can be studied.

We will also investigate aqueous phase growth by taking measurements with several activation $\rightleftharpoons$ evaporation (expansion $\rightleftharpoons$ compression) cycles. The possibility that negative ions cause faster growth and condensation rates than positive ions will be investigated by selecting the ion charges with the field-cage of the cloud chamber (Section 5.3).

3.4.2 Cloud condensation nuclei activation experiments

These studies concern the growth of aerosols into cloud droplets at relative humidities greater than 100%. Such aerosols, known as cloud condensation nuclei, have typical sizes in the atmosphere of 50-100 μm. Aerosols of a well defined size and with typical atmospheric composition (NaCl, $(NH_4)_2SO_4$, H_2SO_4) can be produced with standard aerosol generation techniques (Section 4.4.3). Experiments will be performed to examine the activation of these aerosols into cloud droplets. The cooling of the cloud chamber by expansion will be sufficiently precise to be able to induce supersaturations with respect to water that are typical of the full range of values observed in natural clouds (Section 4.1).

Experiments with and without beam will enable the effect of aerosol charging on activation to be investigated. The charge distribution on the aerosols will be measured using a uniform electric field created by a field cage. In particular, we wish to know whether aerosol charging can reduce the critical supersaturation required to activate an aerosol particle into a water droplet. This can be investigated by counting the number of activated droplets as the supersaturation is gradually increased in separate experiments.

3.4.3 Condensable vapour formation experiments

These experiments will first quantify the poorly-known production rates of a) nitric oxide (NO) and b) hydroxyl radicals (OH) by cosmic radiation. The former will involve pure artificial air and the latter will involve argon and water vapour. Subsequently we will investigate the effects of these vapours on the nucleation and growth of aerosols.

3.4.4 Ice nuclei formation experiments

These studies concern the formation of ice nuclei in supercooled vapours at low temperatures. The expansion chamber will be used to create a supercooled cloud by expansion and growth of drops at temperatures below 260 K. The temperature of the drops can be controlled by the initial temperature of the chamber before expansion. The beam will be pulsed through the supercooled cloud and data recorded. The presence of an ice crystal in a cloud of drops is easily identified since an ice crystal scatters much more light than a water drop (Fig. 19) [61]. The charge distribution on the ice nuclei will be measured using a uniform electric field created by the field cage. In addition to experiments with supercooled liquid droplets already present (freezing nucleation), we will also investigate ice nucleation without pre-existing droplets (deposition nucleation).

3.4.5 Stratospheric cloud formation experiments

These experiments concern the deposition nucleation of nitric acid and water vapours onto ion clusters to form nitric acid hydrates. Particles composed of such hydrates are thought to be the principal component of the polar stratospheric clouds that initiate the destruction of ozone.

The temperature of the cloud chamber will be reduced to typical polar stratospheric values of between 190 and 200 K. Nitric acid and water vapour will be introduced into the chamber at partial pressures representative of the stratosphere (10^{-4} Pa for nitric acid vapour and 5×10^{-2} Pa for water vapour). At these pressures and temperatures the nitric acid hydrates become supersaturated and can condense as crystals provided a suitable nucleus is present. We seek to establish whether ion clusters can serve as these nuclei just as they can for the formation of sulphuric acid droplets in the stratosphere [3]. A background air mixture composed of water, nitric acid and sulphuric acid vapours will be used to represent the species most likely to contribute to initial ion cluster formation.

4 CLOUD detector

4.1 Design considerations

Choice of expansion cloud chamber: The expansion cloud chamber has several important advantages over other nucleation devices[12] for the studies proposed here. In particular, previous measurements with expansion chambers by our collaboration (Helsinki, Missouri-Rolla, and Vienna) have verified that the thermodynamic conditions after an expansion are precisely known and reproducible, provided that the initial conditions are well-known and the expansion ratio (pressure change) is well-measured. Moreover the expansion chamber can provide a large volume with uniform thermodynamic conditions where, for example, relatively slow processes can be measured. Expansion chambers may in fact be the only devices that can achieve the necessary thermodynamic stability and precision to study aerosol activation in the laboratory at the very small water vapour supersaturations (few $\times$ 0.1%) found in clouds and, in addition, cover the full range of supersaturations up to those required to activate small ions and nanometre-sized aerosols.

Size of cloud chamber: A large cloud chamber ($\sim$50 cm diameter) achieves the longest time of known thermodynamic conditions in the fiducial volume[13] of the chamber. The sensitive time[14] ranges from about a second for expansions that produce high enough supersaturations in water vapour to activate ions (a large difference in temperature between the walls and the gas) to several tens or even hundreds of seconds for the activation and growth of large aerosols (a small difference in temperature) (Section 5.2). The sensitive

[12]Besides the expansion cloud chamber, other experimental devices for studying nucleation include the thermal diffusion cloud chamber, cooled-wall expansion chamber, shock tubes and turbulent mixing chambers.

[13]The fiducial volume is the central region of the chamber where the thermodynamic and other conditions are well known, and where the measurements are made.

[14]The sensitive time following an expansion refers to the period during which no significant changes of thermodynamic conditions occur in the central part of the chamber caused by the heating influences of the walls.

time of an expansion chamber increases steeply with its size since it is proportional to the square of the ratio of the volume to wall area, which re-heats the gas following an adiabatic expansion. In addition a chamber size of about 50 cm ensures that diffusion losses of the aerosols to the walls are not significant for measurements lasting up to several hours with a single fill (see Section 5.4.2).

Water vapour supersaturation: The cloud chamber is required to operate at water vapour supersaturations (SS) from below zero (unsaturated) up to about 700%. An important requirement is to provide precise simulation of the conditions found in clouds, for which $0.1\% \lesssim SS \lesssim 1\%$ (Appendix A). This supersaturation range corresponds to a broad activation range of aerosols, namely radii from about 1 μm (at 0.1% SS) down to about 50 nm (at 1% SS). In order to probe the aerosol size distribution with sufficient resolution, the chamber needs to achieve a SS precision after expansion of about 0.1% in the range $0 < SS < 1\%$. Furthermore, the cloud chamber also needs to measure condensation nuclei down to small ion dimensions (0.2 nm), which requires large expansions producing supersaturations of up to 500%. The precision of the large SS values is, however, less demanding than for the small values.

Expansion time: The time duration of the expansion pulse needs to be short compared with the droplet growth time so that the start time is the same for all activated aerosols. This is especially important for experiments involving a broad size distribution of aerosols (to represent atmospheric aerosols), which activate over a relatively wide range of supersaturations. A rapid expansion ensures that the larger aerosols do not deplete the water vapour and prevent activation of the smaller aerosols. In practise the fastest required expansion time is about 200 ms. For comparison, the expansion time for the 25 cm Vienna chamber is 20-30 ms and, for the 38 cm Missouri-Rolla chamber, it is 200 ms.

Temperature and pressure operating range: The cloud chamber is required to operate over the full range of temperatures and pressures encountered by clouds in the troposphere and stratosphere, namely 173 K $< T <$ 293 K and $0 < P <$ 101 kPa. The maximum pressure of the chamber is actually 150 kPa, in order to allow measurements to be made at 1 atm following a large expansion. It is important to note that the full range of pressure change can be addressed with our chamber design (Section 4.2.2). In a typical expansion chamber the pressure of the gas in the sensitive volume is used to drive the piston. For low pressures this becomes ineffective. In the cloud chamber proposed here, the piston is moved by a hydraulic system and thus a fast and precise expansion and re-compression can be achieved regardless of the pressure change in the chamber.

Temperature and pressure stability: The requirement of a precision of 0.1% on the supersaturation places demanding requirements on the temperature control of the cloud chamber. Taking a design value for the supersaturation error of one half this value, i.e. 0.05%, implies the need for a temperature stability $\Delta T = 0.01$ K and a pressure stability $\Delta P/P = 1.3 \cdot 10^{-4}$ or, equivalently, a volume stability $\Delta V/V = 0.9 \cdot 10^{-4}$ (see Section 5.1, Eq. 6). Note that these are *stability* requirements; the absolute precisions of the temperature and pressure are less demanding.

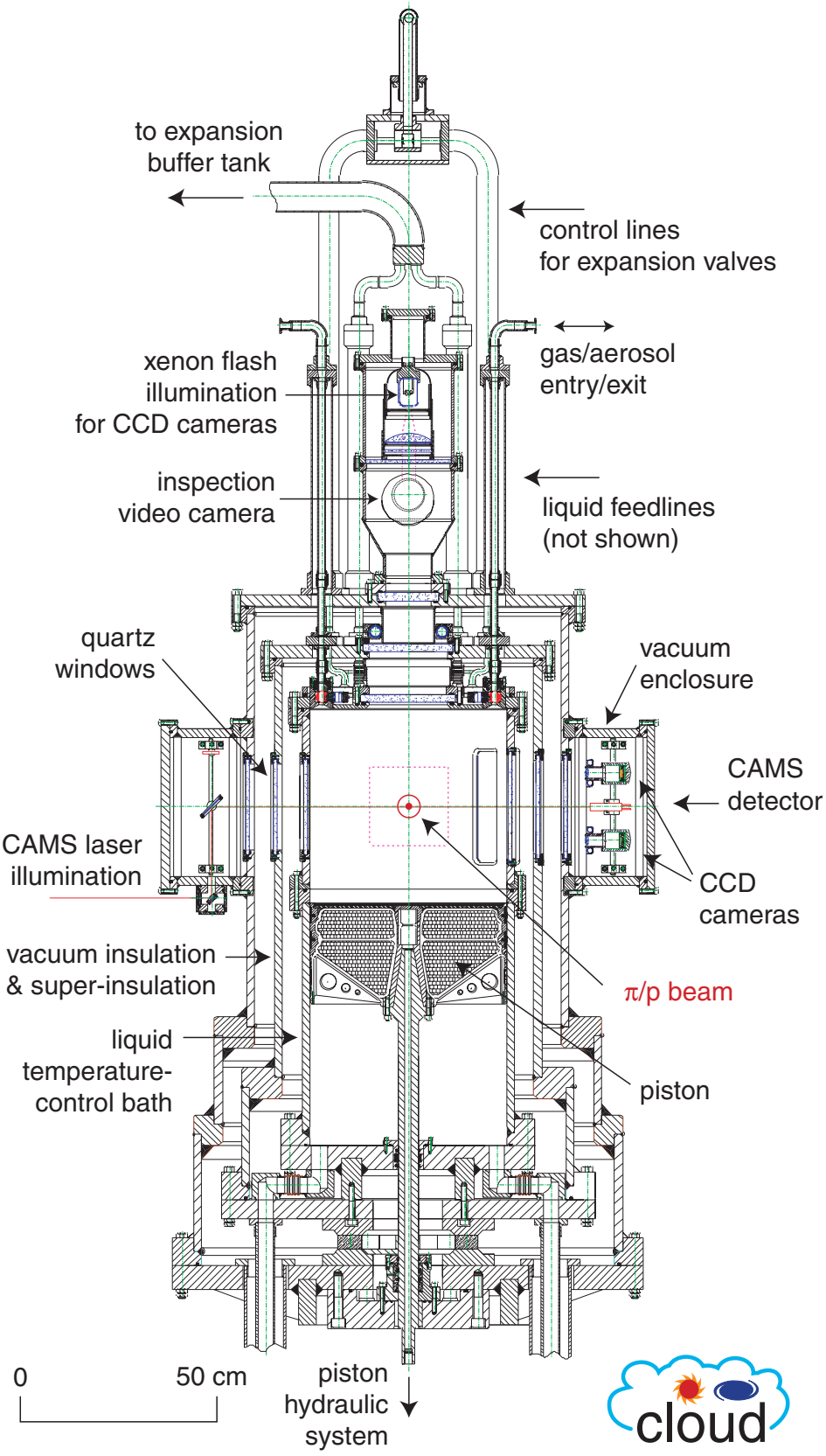

Figure 20: Vertical section through the CLOUD detector.

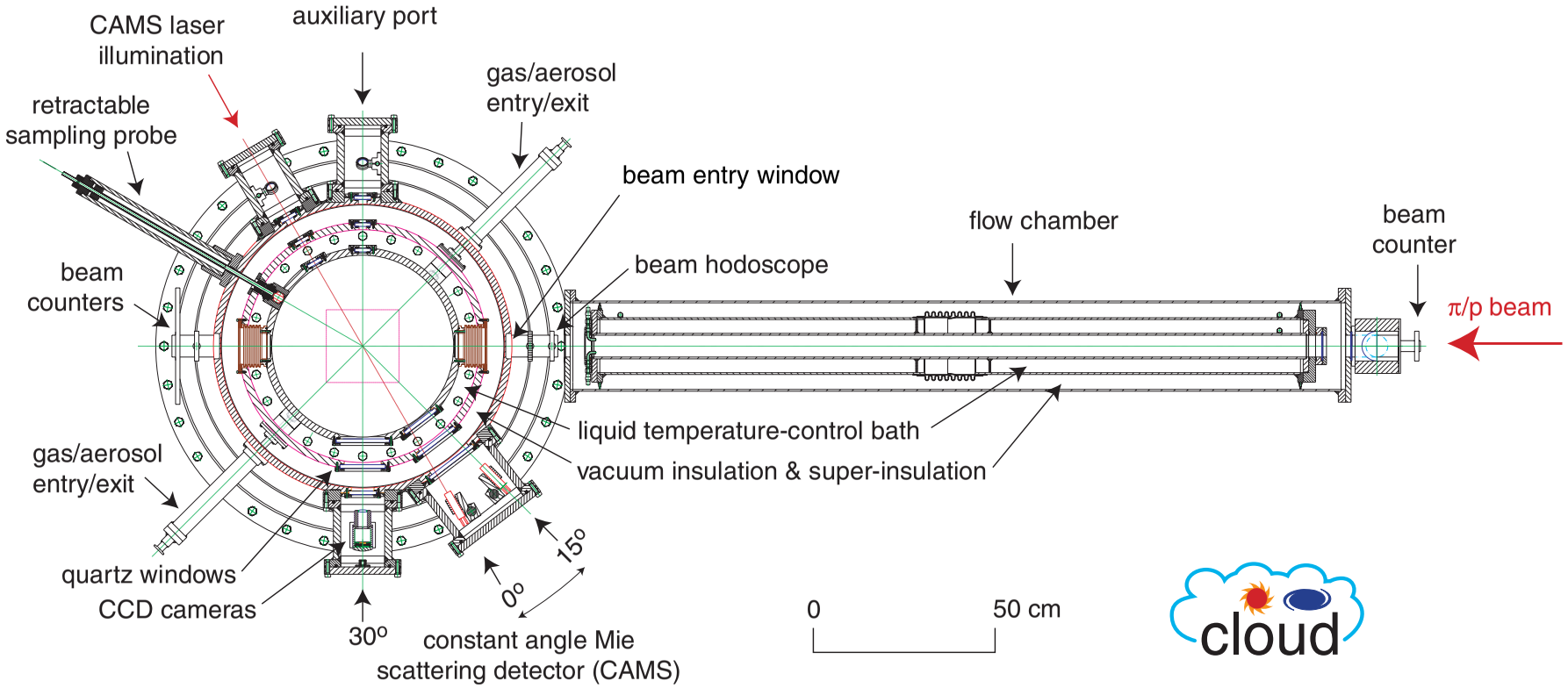

Figure 21: Horizontal section through the CLOUD detector. The CAMS detectors all lie in the same plane whereas the CCD cameras are displaced above and below the plane of the figure.

4.2 Cloud chamber

4.2.1 Overview

The CLOUD detector is shown in Figs. 20 and 21. The active volume is a cylinder of dimensions 50 cm (height) × 50 cm (diameter) and the fiducial volume is the central region of linear dimensions about 10–20 cm. The chamber is completely surrounded by a liquid bath which maintains precise temperature control. An outer vacuum enclosure, together with super insulation, maintains the thermal insulation of the inner detector. The cloud chamber volume is equipped with an electrode structure (field cage) to provide a clearing field or the possibility to drift and measure charged aerosols. It also allows a method to select positive or negative charges for separate study.

Expansions are made by two techniques: a piston and a buffer expansion tank. The former is operated by a hydraulic system similar in design to the Big European Bubble Chamber (BEBC). The buffer expansion tank involves an external tank with a volume ten times larger than that of the cloud chamber. Expansions are effected by first reducing the pressure in the external tank to the desired value and then opening fast-acting valves connecting the external tank to the cloud chamber.

The optical readout of the cloud chamber comprises two systems: a) a constant angle Mie scattering (CAMS) detector and b) a stereo pair of CCD cameras. The two systems are complementary but, nevertheless, have a broad region of overlap where they can provide mutual cross-checks. The CAMS system can measure very high droplet number densities ($\sim$10–10^7 cm^{-3}) whereas the CCD cameras operate best in a lower range ($\sim$0.1–10^5 cm^{-3}). The CAMS system provides a high-resolution measurement of mean droplet radii vs. time, whereas the CCD cameras provide a measurement of droplet size in coarser time intervals, using pulse height information. Finally, the CAMS detector integrates over all illuminated droplets whereas the CCD cameras reconstruct the 3-dimensional spatial positions of individual droplets, and tracks their movements. This is important for identifying ice nuclei (Section 3.4.4) and for measuring droplet drift velocities (large droplet sizes).

The illumination system comprises: a) a laser for illumination of a narrow region for the CAMS detector (and, in parallel, for the CCD cameras) and b) a xenon flash tube for the CCD cameras, mounted at the top window (an auxiliary xenon flash system is also mounted close to the CCD cameras). A video camera is also mounted at the top window in order to provide a visual inspection of the chamber volume and piston surface. The video camera and xenon illumination share the same window by means of a partially reflecting mirror (Fig. 20). The side windows are designed to allow simultaneous viewing of both the beam- and no-beam regions of the chamber. All windows are made of optical quality quartz. The use of quartz allows for the possibility of including UV irradiation to investigate reactions involving photochemical processes.

Cleaning of the chamber is very important to ensure reliable results. The upper window is designed to be removable to allow cleaning access to the inside of the chamber and to minimise the transition time between different chamber fills. The chamber is also cleanable by vacuum baking. Vacuum evacuation is also an effective and rapid technique for removing a gas/aerosol mixture before refilling. Finally, large chamber expansions with a pure carrier gas can be used to confirm the cleanliness of the chamber before filling with a new mixture. Indeed, droplet activation and sedimentation is a proven technique

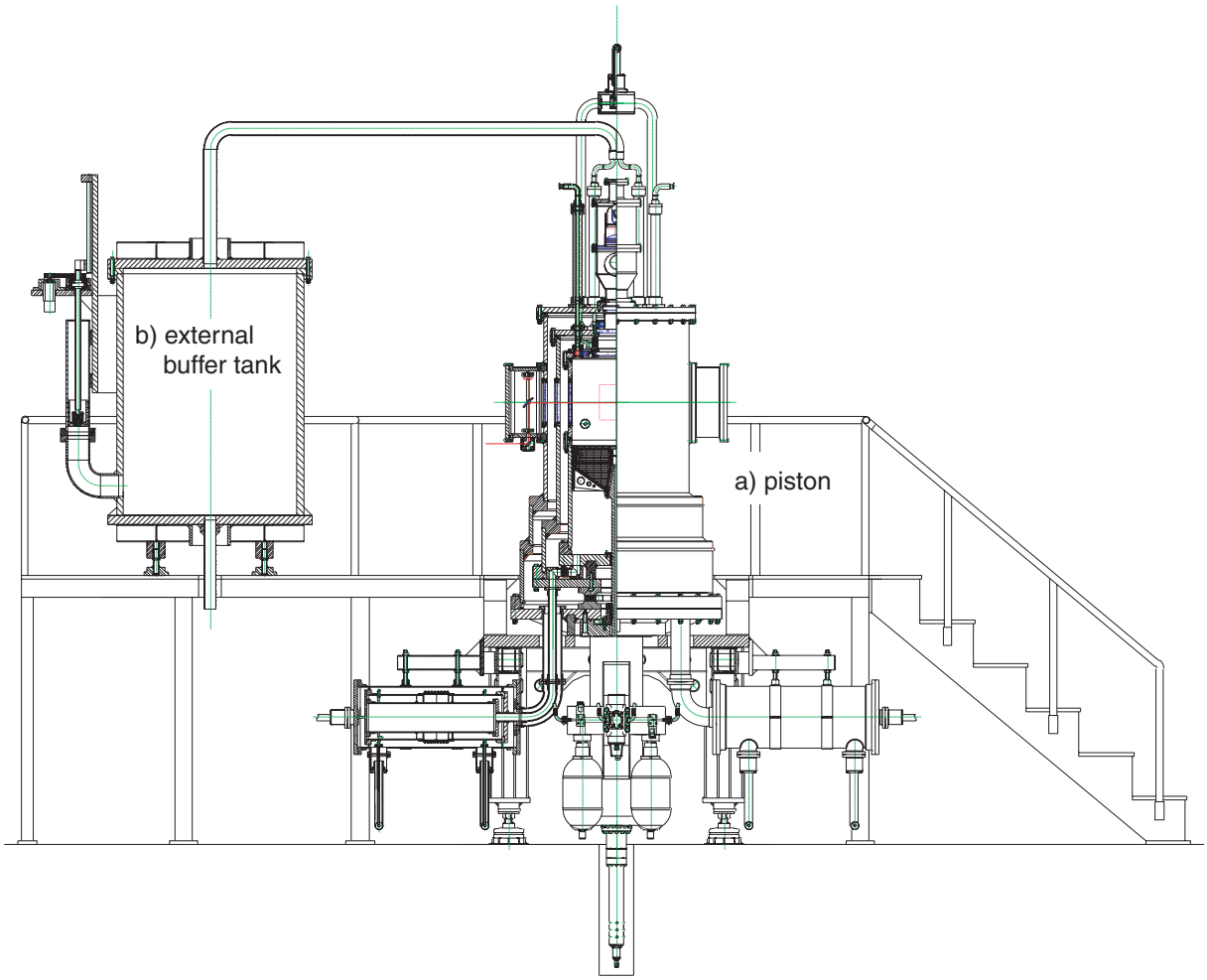

Figure 22: Cloud chamber expansion systems: a) piston and b) external buffer tank.

to clean the cloud chamber to ultra low levels of contamination.

The chamber is equipped with two sampling probes. These provide the possibility of extracting gas and aerosols from the fiducial region of the cloud chamber. They also provide the possibility for special measurements such as, for example, injection of a special gas into a limited region at the centre of the chamber. The probe tubes are straight and have a large diameter inner bore. All valves and pipes leading to and from the chamber are designed to provide efficient transmission of aerosols (large diameters and gentle curves).

A flow chamber (2m-length $\times$ 6cm-diameter) is integrated with the cloud chamber assembly and exposed to the same beam as the cloud chamber. It provides the source for external measurements of the physical and chemical properties of the trace gases, aerosols and ions with mass spectrometers, ion detectors, condensation particle counters (CPC) and differential mobility particle sizers (DMPS).

4.2.2 Expansion techniques

The cloud chamber has a flexible choice of expansion techniques and expansion/ re-compression cycles. There are two expansion techniques (Fig. 22):

a) Piston: Piston movement involves active control of the piston connecting rod by means of a hydraulic system similar in design to that used for the Big European Bubble Chamber (BEBC). An important advantage of piston expansions is that they minimise the gas turbulence, an effect that becomes more significant as the expansion ratio increases. The piston also provides a flexible choice of precise expansion and re-compression cycles, with piston movements reproducible to very high precision—better than 5 μm. The range of piston movement is 5 μm to 200 mm i.e. volume expansion ratios of between 10^{-5} and 0.4. The very small expansions will provide supersaturations characteristic of those found in atmospheric clouds, while the largest expansions will activate aerosols of molecular/small-ion dimensions. The largest expansions also provide an effective method to clean trace condensation impurities from the cloud chamber by activation and then sedimentation.

b) External buffer tank: This is a second method to produce small expansions. It involves a tank with a volume $\sim$10 times larger than the active volume of the cloud chamber, i.e. $\sim$1 m^3. The tank is not cooled but has good thermal insulation to ensure that any temperature fluctuations are slow over the period of a particular measurement. It is directly connected to the active gas volume via synchronised fast-acting valves at the top of the chamber. Expansions are effected by first achieving a pressure equilibrium with the valves open, then closing the valves, reducing the pressure in the buffer tank by the required (small) amount and finally re-opening the valves. The valves are left open during the sensitive time of the cloud chamber. The piston remains in a fixed location throughout. An important advantage of this method is that it extends the sensitive time since it provides passive compensation for the pressure rise following an adiabatic expansion. The pressure rise occurs due to heating of the layer of gas near the walls and it causes a temperature rise throughout the volume by an adiabatic re-compression of the gas.

4.2.3 Operational experience with cloud chambers

Some operational experience of our collaboration with cloud expansion chambers is summarised below:

1. *Reproducibility:* The expansion ratio is determined from the initial and final pressures, since these quantities can be measured precisely—better than 10^{-4} absolute. Other quantities such as temperature change and supersaturation are calculated from the pressure change and the known initial conditions. In the 38 cm Missouri-Rolla chamber the pressure change is highly reproducible from pulse to pulse (a spread of about $2 \cdot 10^{-4}$ for a large pressure change of 90 kPa).

2. *Cycle time:* The 25 cm Vienna chamber requires about 1 hr between expansions to allow time for thermodynamic equilibrium to be re-established. The 38 cm Rolla chamber requires about 5 min for equilibrium to be re-established following a deep expansion producing a temperature change ΔT = -40 K, during continual operation. The cycle time is largely determined by how quickly the walls of the chamber can be brought back to the operational temperature following an expansion cycle.

3. *Conditioning time:* The 25 cm Vienna chamber requires 1–2 days conditioning prior to taking data.

4. *Chamber cleaning:* Based on 20 years experience with the operation of expansion cloud chambers at Missouri-Rolla, the following technique will clean a cloud chamber sufficiently for the demanding requirements of homogeneous nucleation measurements:

    - The chamber is first fogged with liberal quantities of pure high quality water to dilute and remove water soluble components,. A fog nozzle sprays water drops over the chamber so that all surfaces are wetted and water runs down the walls. (In the CLOUD chamber the water will be injected through the sampling probe tubes.) After the application of about 4 litres, the water at the bottom of the chamber is removed with a tube suction device. After about 3 applications, a vacuum is applied to remove residual water.
    - Acetone is then applied and is very effective at removing the last traces of water (particularly any water that has a surfactant preventing evaporation) as well as traces of any hydrocarbons etc., for which it is an excellent solvent. The acetone is removed from the bottom of the chamber and the remaining (high vapour pressure) acetone is removed by vacuum evaporation.
    - Finally, the chamber is warmed under vacuum to remove the residual volatile contamination.

4.2.4 Piston and hydraulic system

The piston expansion system comprises two main parts: the main piston and connecting rod, and the hydraulic system (Fig. 22a). The latter is based on the same design as was used to control the 2 m-diameter piston of BEBC [73].

The main piston head is made of a stainless steel envelope containing an inner stiffening structure. The piston has several grooves for holding spring-loaded PTFE seals which provide the gas seal with the walls of the cylinder. The upper surface of the piston is light-absorbing to reduce reflections from the top-window illumination (Section 4.3.2). The outer region of the upper surface of the piston is shaped to provide a film of water for establishing 100% relative humidity in the active chamber volume. The inner structure of the piston is a sandwich assembly made of honeycomb and resin polymer plates reinforced with carbon fibre. This provides a good structural rigidity while maintaining a low mass. A low mass is important since the required acceleration rates are large (up to 30 g) to achieve a fast expansion time for piston strokes up to the maximum of 200 mm. The main piston rod is made of stainless steel. The upper end of the rod is linked to the piston through a kernel which is dismountable for assembly and maintenance purposes. The lower end of the rod is fitted with a hydraulic piston which is driven by the servo-mechanism.

The servo-mechanism (Fig. 23) is made of several main components: a servovalve, a hydraulic pump, and high pressure and low pressure accumulators [74]. There are three circuits containing liquid hydraulic oil: high pressure circuit (220 bar), low pressure circuit (20 bar), and the control circuit (running at a nominal pressure of 160 bar). All circuits

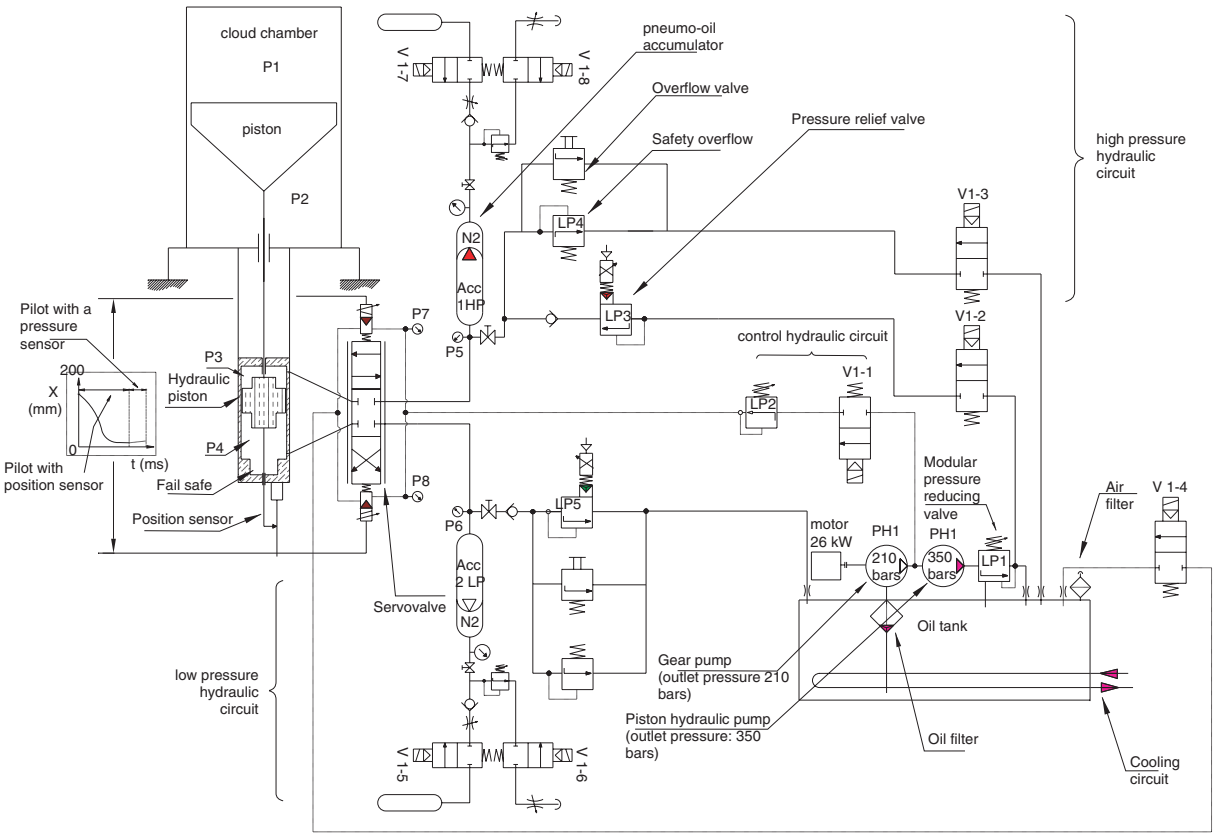

Figure 23: Schematic diagram of the hydraulic system for piston expansions and re-compressions.

are supplied by a hydraulic pump delivering an outlet pressure of 350 bar and a nominal flow rate of 20 l/min for a rotation speed of 1500 rpm. The power consumption is about 26 kW. The high pressure circuit feeds the high pressure accumulator (10 l capacity), which serves as an energy tank for the expansion. A low pressure accumulator (which is normally not present in these systems) is also included to avoid any shocks in the circuits or back effects at the end of the piston travel. Each of the circuits is equipped with pressure relief valves, with recuperation into a 100 l tank, and flow rate regulating valves.

The control circuit drives the most critical component of the hydraulic system: the servovalve (Fig. 24). Depending on the electrical signal (± 10 V) delivered by a computer, the spool slides inside the bushing of the control stage. The power stage spool is then moved, and the inlet/outlet connect the expansion chamber of the hydraulic piston with the high and low pressure accumulators. Any movement of the latter has then a direct effect on the main piston rod. The nominal control flow rate of the servovalve (control stage) is 28 l/min, and the opening time is about 6 ms. The power flow rate through the servovalve can reach 1500 l/min, which leads to an expansion time of about 150 ms for the maximum stroke of 200 mm. Shorter piston strokes are more rapid; for example, the expansion time is below 10 ms for a 5 mm expansion (which produces a supersaturation of about 6%). The limiting parameter is the ability of the main piston head to withstand acceleration. The hydraulic system provides complete flexibility for the choice of expansion and re-compression cycles, which are determined by the analogue voltage pulse

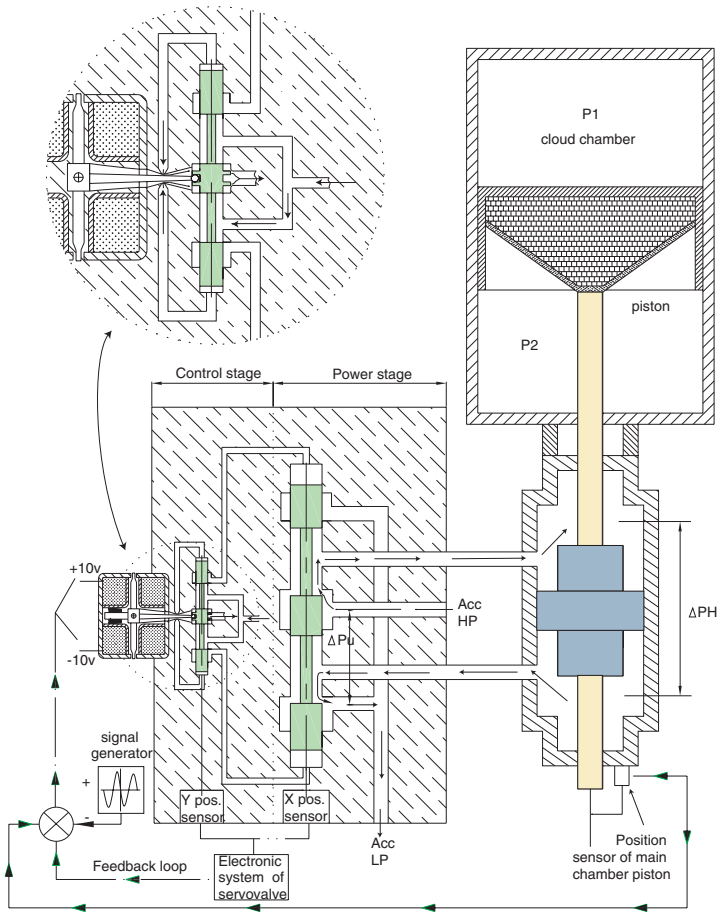

Figure 24: Principle of the servovalve for controlling the piston expansions and re-compressions.

shape delivered by the control computer. The system also delivers an extremely precise (± 5 μm) and reproducible (better than ± 5 μm) movement of the piston.

The hydraulic piston (100 mm diameter) has no seal and its fit within the cylinder is of prime importance. A prototype of the main piston, hydraulic piston and servovalve system is required in order to validate the study and fix the parameters for the final installation, such as the pressure loss in the circuits and the leaks to be compensated. The maximal allowable acceleration of the piston is another important issue that requires evaluation with the prototype.

4.2.5 Liquid cooling system

The liquid cooling and temperature control system for CLOUD (Fig. 25) involves a closed circuit system, insulated throughout by vacuum. The liquid coolant flows through a jacket surrounding the cloud chamber and maintains the inner wall and piston at a precisely-controlled temperature. The gas inside the cloud chamber is allowed to reach thermal equilibrium with the walls before taking any measurements. A fluorocarbon liquid is used, such as FC87 (C_5F_{12}), which is liquid in the range 163 K–303 K at atmospheric pressure. The fluorocarbon is transparent to visible and UV wavelengths down to about 180 nm. Consequently the liquid can circulate between the windows to obtain the optimum thermal jacket, without compromising the optical measurements or the option of UV irradiation

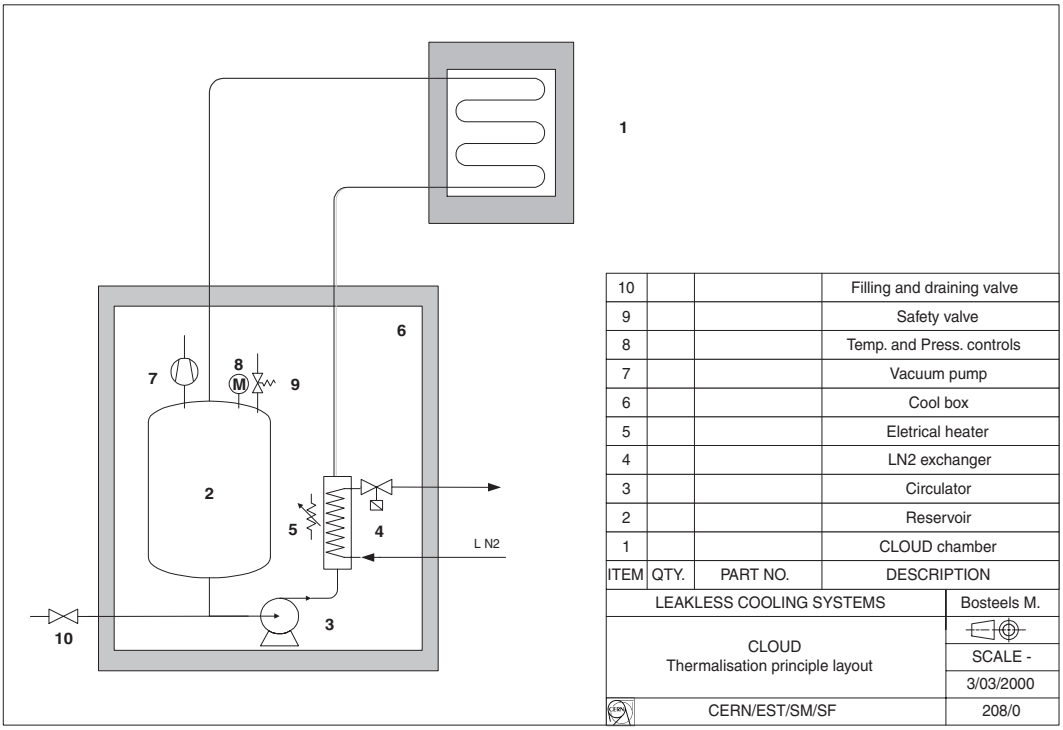

Figure 25: The liquid cooling and temperature control system.

of the active volume.

A coolant reservoir, circulation pump and heat exchanger are placed in a cold box. The temperature of the circulating fluorocarbon liquid is adjustable in the range from 173 K–293 K. Temperatures are measured with Pt1000 platinum resistance thermometers which provide measurements stable to 0.001 K. The fluorocarbon is cooled by liquid nitrogen evaporating at a constant pressure, and re-heated by an electrical heater. This allows fine temperature control and higher stability than can be obtained with a refrigerator unit. Our experience of similar liquid cooling systems for particle physics detectors shows that temperature stabilities of 0.1 K can be achieved for relatively large, non-insulated detectors involving internal heat sources and located in experimental halls without air-conditioning. In comparison, the CLOUD system is relatively compact, insulated throughout by a vacuum layer, and without any internal parasitic heat loads. This indicates that, with careful design, a temperature stability of 0.01 K can be achieved.

4.2.6 Field cage

The walls of the cloud chamber are equipped with a field cage which provides an electric field inside the active volume. The functions of the electric field are as follows:

- To clear ions and charged aerosols from the active volume.
- To allow measurements at *below* atmospheric ion concentrations. The typical ion concentration at the top of the troposphere is a few 1000 cm^{-3} (Section D.1); the

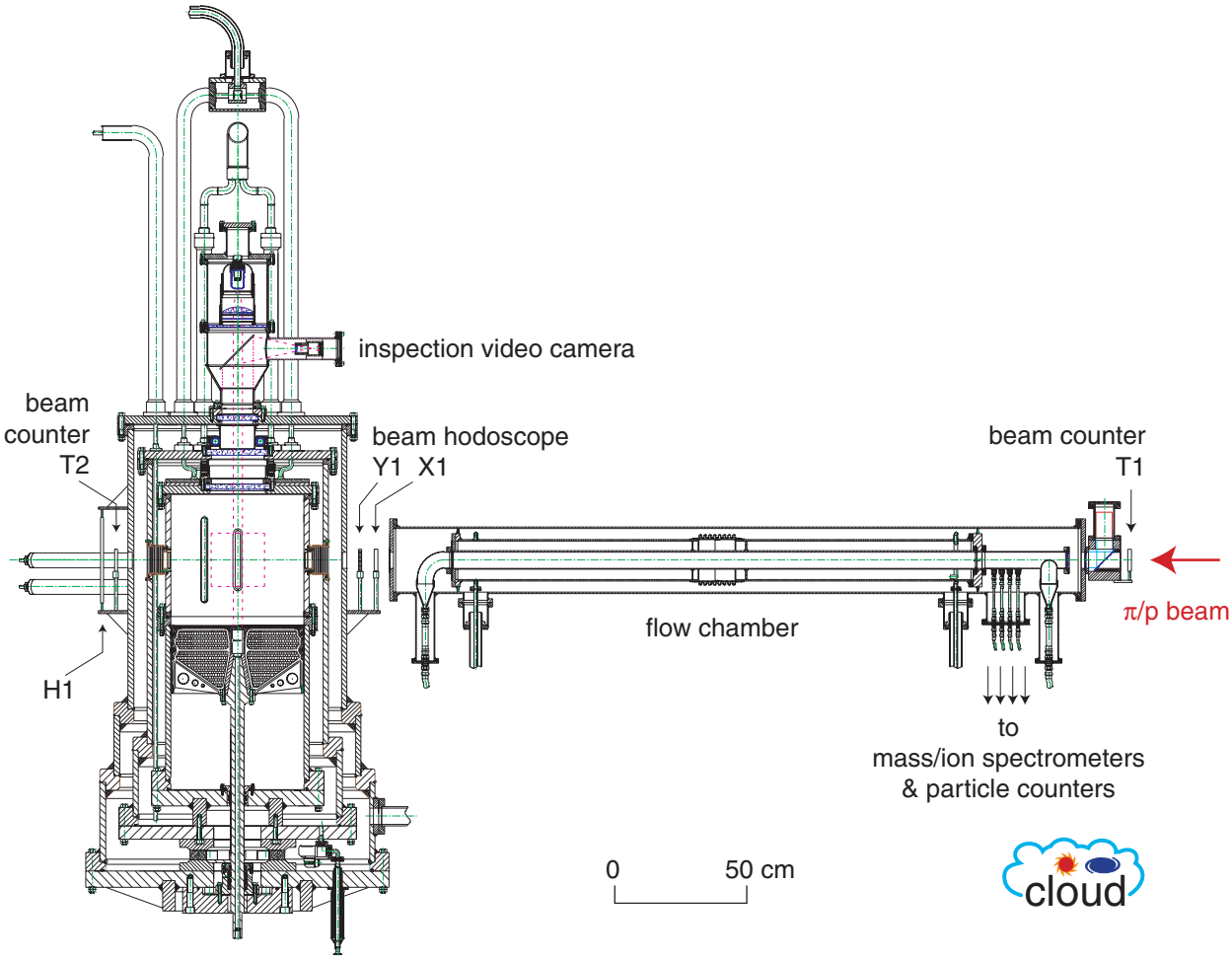

Figure 26: Vertical section showing the flow chamber and beam counter system.

clearing field can lower the small ion concentration in the cloud chamber to near zero in about 2 s (Section 5.3).

- To separate positive and negative ions and charged aerosols in order to measure their properties separately. In addition, this will allow a technique for slowing charge neutralisation by +/- ion recombination.

- To allow an approximate measurement of the aerosol size/charge distributions by measurement of the electrical mobility before activation. This is done by allowing the ions and charged aerosols to drift in a uniform field for a known time before the expansion pulse. The resulting droplets effectively freeze the final locations of the charged particles and allow their drift paths to be estimated and hence also their electrical mobilities. This provides a technique to check for consistency with the more precise mobility measurements provided by external detectors.

The field cage involves circular electrodes laid down on an 800 μm-thick ceramic insulating layer which lines the inside of the cloud chamber. The electrodes are continued across the chamber windows by means of thin, vacuum-deposited traces; these result in a negligible loss of light intensity for the optical readout systems. A layer of electrodes

at the top of the cylinder completes the field cage. Except in the region of the windows, the electrodes are covered with a layer of black teflon, which is in contact with the gas in the active volume. The teflon has a small conductivity in order to avoid charge buildup and consequent field distortion. The cloud chamber walls and piston are grounded, and the field wire potentials are appropriately set relative to this ground, up to a maximum of 500 V. The performance of the field cage is summarised in Section 5.3.

4.2.7 Flow chamber

A flow chamber of dimensions 2 m length × 6cm-diameter is integrated with the cloud chamber assembly (Fig. 26). It is filled with the same gas/aerosol mixture as the cloud chamber, and exposed to the same particle beam and, where required, to the same UV irradiation. Furthermore it is operated at the same temperature and pressure, but without the need for the same high precision on temperature and pressure stability. The exhaust gas from the flow chamber is analysed using condensation particle counters (CPC), differential mobility particle sizers (DMPS), mass spectrometers and ion mobility detectors (see Fig. 32 and Sections 4.4 and 4.5).

4.3 Optical readout

4.3.1 Constant angle Mie scattering (CAMS) detector

The CAMS detection method allows simultaneous measurement of number concentration and size of growing droplets. This method has been successfully applied in various experimental studies of nucleation and condensation processes [75, 76, 77]. A detailed description of theoretical and experimental aspects of the CAMS detection method can be found elsewhere [78, 79]. The general schematic layout of a CAMS system is show in Fig. 27 and the geometry for CLOUD is shown in Fig. 21. In the following the main features of CAMS are presented as they are relevant for the proposed research project.

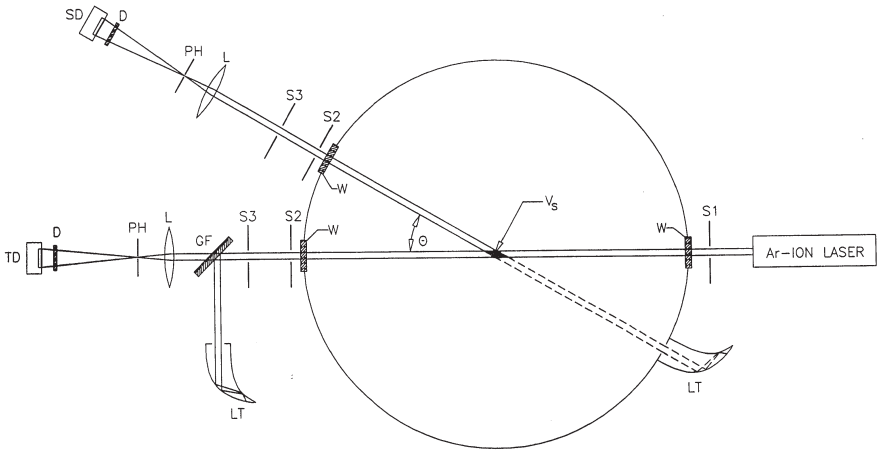

Figure 27: Schematic diagram showing the experimental arrangement for the CAMS detection method.

The CAMS detection method is based on light scattering. Growing spherical particles are illuminated by a monochromatic, parallel light beam, e.g. a laser beam (Fig. 27). The light flux Φ_{trans} transmitted through the measuring chamber is monitored during the particle growth process by means of photodetector TD. Simultaneously, the light flux Φ_{sca} scattered at a selectable constant scattering angle Θ is monitored by means of photodetector SD. The observation cones of the detectors are defined by corresponding lens-pinhole arrangements L-PH. The actual sensitive volume V_S inside the measuring chamber is determined by the intersection of laser beam and observation cone of detector SD for scattered light.

Our measurements from a typical CAMS experiment are shown in Fig. 28. Here simultaneous growth of liquid drops in supersaturated vapour was observed. The vapour supersaturation was achieved by means of an adiabatic pressure jump in an initially saturated system. This pressure step is indicated by the upper curve in Fig. 28. The middle curve in Fig. 28 shows (inverted) the transmitted light flux Φ_{trans} as a function of time during the droplet growth process. The lowest curve shows the scattered light flux Φ_{sca} as a function of time. In the experiment considered a forward scattering angle $\Theta = 15°$ was chosen, the incident laser beam was linearly polarized perpendicular to the plane of observation.

As can be seen from Fig. 28, the experimental scattered light flux vs. time curve shows a series of maxima and minima. These extrema are connected to light diffraction and can be uniquely identified, as will be shown below. Thereby the particle size can be determined at each of the experimental extrema. In the absence of multiple light scattering the experimental scattered light flux will be proportional to the number of particles inside the scattering volume. Accordingly, the droplet number concentration can be evaluated from the height of the experimental light scattering maxima independent of the determination of particle size.

The middle curve in Fig. 28 (inverted in the figure) shows that the transmitted light flux Φ_{trans} decreases significantly during the droplet growth process. Thus it can be concluded that considerable light extinction can occur inside the measuring chamber, particularly at later stages of the particle growth process. This light extinction will be increasingly pronounced for increasing particle number concentrations. Obviously the experimental scattered light flux will be reduced due to light extinction in the measuring chamber as well. Thereby the values of the particle number concentrations, as determined directly from the height of the experimental light scattering maxima, will generally be somewhat smaller than the actual concentrations. A correction for this light extinction effect would require the knowledge of the actual particle number concentration. Fortunately, the reduction of the scattered light flux due to light extinction can be taken into account in the following way. As seen from Fig. 28, the scattered light flux Φ_{sca} will suffer approximately the same light extinction as the transmitted light flux Φ_{trans}, if the scattering volume V_S is restricted to the central part of the measuring chamber. Thus the effect of light extinction on the scattered light flux can be compensated by normalising the scattered relative to the transmitted light flux. Accordingly, a linear relation between the *normalised* scattered light flux Φ_{sca}/Φ_{trans} and the particle number concentration can be expected over a wide concentration range.

In order to achieve a unique quantitative interpretation of the light scattering curves as obtained from CAMS experiments, it is important to calculate the normalised scattered

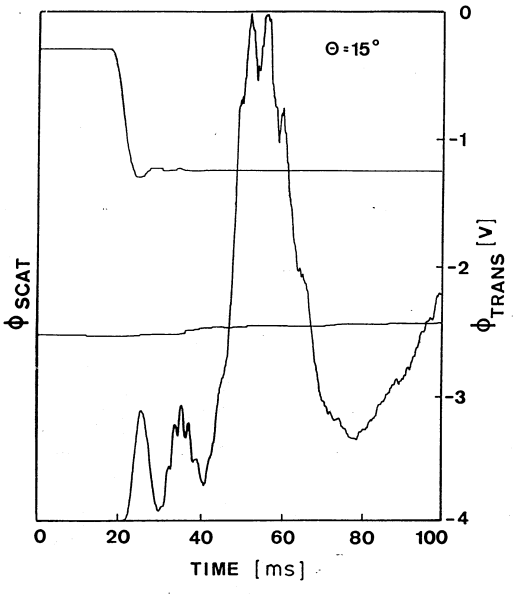

Figure 28: Result of a typical single CAMS experiments at Vienna for a forward scattering angle $\Theta = 15°$. The uppermost curve shows the pressure step in the expansion cloud chamber. The middle curve shows the (inverted) transmitted light flux, and the lowest curve shows the scattered light flux.

light flux Φ_{sca}/Φ_{trans} as a function of droplet size for various constant scattering angles. The theory of light scattering by spherical particles has been derived by Mie [80] and Debye [81]; a recent treatise by Bohren and Huffmann [82] includes efficient numerical methods for evaluation of the relevant light scattering functions. Fig. 29 shows a comparison of experimental scattered light flux vs. time curves with theoretical scattered light flux vs. size curves for forward scattering angle $\Theta = 15°$. Satisfactory agreement between experimental and theoretical data can be observed allowing to establish a one-to-one correspondence of experimental and theoretical light scattering extrema.

The morphology of the light scattering curves depends on the size distribution of the growing droplets. As can be seen from Fig. 30, the resonant ripple structure of the light scattering curves tends to disappear with increasing width of the drop size distribution. Thus CAMS measurements require sufficiently narrow drop size distributions to identify unambiguously a single peak in isolation. However it can be seen that the first scattering maximum at the forward scattering angle $\Theta = 15°$ is not very sensitive to changes of the width of the drop size distribution.

When a unique correspondence between experimental and theoretical light scattering extrema is established, the particle sizes at specific times during the growth process can be obtained from the positions of the extrema of the experimental normalised light scattering curves relative to the time axis. Independently, the droplet number concentrations at specific times during the growth process can be determined from the heights of the maxima of the experimental normalised light scattering curve by comparison to the corresponding theoretical curve. In this connection it is important to note that, as mentioned above, the normalised scattered light flux Φ_{sca}/Φ_{trans} is linearly related to the droplet number concentration. Determination of the droplet number concentration can

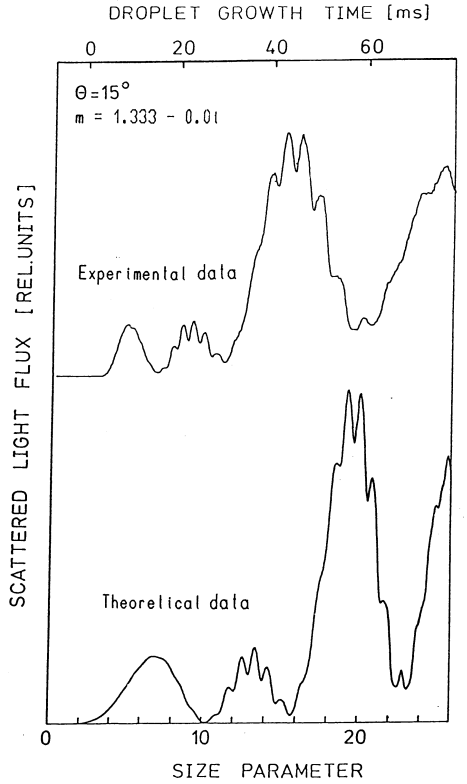

Figure 29: Comparison of experimental scattered light flux vs. time curves to theoretical scattered light flux vs. size curves for forward scattering angle $\Theta = 15°$.

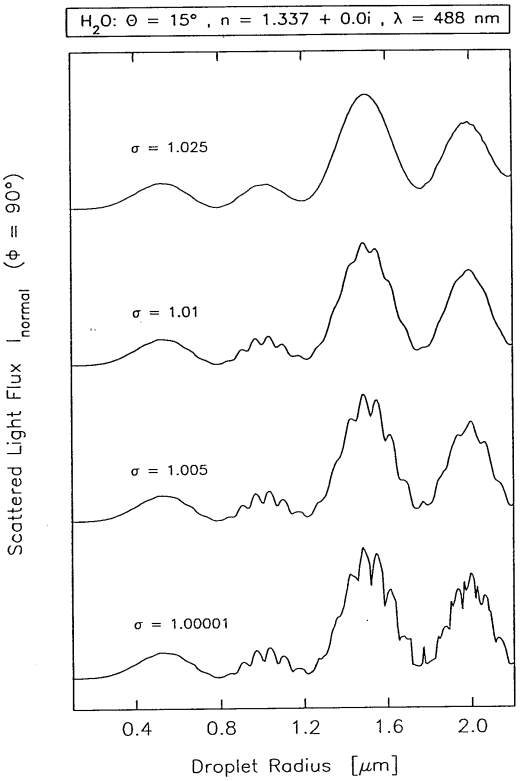

Figure 30: Influence of drop size distribution on scattered light flux for forward scattering angle $\Theta = 15°$. The curves are labelled according to the relative spread, σ, of the droplet radii.

thus be performed by measurement of the ratio Φ_{sca}/Φ_{trans} of scattered and transmitted light flux. To this end it is necessary to perform a mutual calibration of the detectors TD and SD for transmitted and scattered light fluxes, respectively. This calibration can be avoided by quantitatively considering the light extinction inside the measuring chamber. From measurements of the light extinction at certain droplet sizes the droplet number concentration can be determined independently.

The choice of appropriate scattering angles depends on the actual measurements to be performed. For determination of particle concentrations it is advantageous to use comparatively small forward scattering angles, because the corresponding light scattering curves exhibit a rather simple structure with few broad maxima, which can easily be identified even for comparatively broad droplet size distributions. Furthermore, comparatively high scattered light fluxes occur, allowing accurate measurements of the heights of the observed light scattering maxima. For measurements of drop growth rates, however, somewhat larger scattering angles are advantageous, because the corresponding light scattering curves show a somewhat more complex structure, providing detailed information on drop growth.

In summary the CAMS detection method is applicable to the observation of growing spherical particles (droplets) with known refractive index. The droplet size distribution

needs to be sufficiently narrow so that distinct extrema can be observed in the experimental light scattering curves. Measurements over a comparatively wide range of droplet number concentrations can be performed. The lower limit of the concentration measuring range depends on the actual sensitive volume V_S as determined by the incident laser beam and the observation cone of the detector SD for scattered light. In order to allow a unique evaluation of the experimental scattered light curves, generally more than about 5 particles must be simultaneously present inside the sensitive volume during particle growth. The upper limit of the particle concentration range will depend primarily on the amount of multiple scattering inside the measuring chamber [79]. As shown recently [83], CAMS measurements show a linear concentration response over a range of concentrations up to as much as several 10^7 particles per cm^3. Finally it should be noted that the CAMS detection method is a non-invasive method for absolute measurement of drop size and number concentration. No empirical calibration referring to external reference standards is required.

4.3.2 CCD cameras and optics

CCD cameras and readout: The Rutherford Appleton Laboratory has designed and built a very fast, twin channel CCD imaging system for the August 1999 total solar eclipse, which is available for CLOUD. The SECIS (Solar Eclipse Coronal Imaging System) was successfully used to obtain in excess of 12,000 images during totality (i.e. in a period of less than 3 minutes) from a site close to the Black Sea in Bulgaria.

In essence, SECIS is an extremely fast, high-resolution imaging system. It is a considerable advance over previous systems in both frame rate and photometric accuracy. To meet the requirements of the solar eclipse observation, consecutive large area images needed to be stored at a very fast rate that was not until recently possible in any existing system but now is technically feasible using new developments in CCD cameras and memory storage units. Currently, SECIS uses two small-area CCDs to obtain fast images and large on-line processing arrays to handle the image data. The computer system, interfaces and camera power supplies fit in a medium-sized, portable PC enclosure. Extra cooling is built into the enclosure to allow operation in hotter environments than normal. An uninterruptible power supply provides power for the whole system. Each frame of data is time-tagged for subsequent individual access from the PC.

The solar eclipse experiment required the capability of storing a large number (several thousand) consecutive frames of data without interruption. The two CCD cameras used are state-of-the-art digital cameras. Each has a 512×512 format with 15×15 μm^2 pixels. The data is digitised to 12 bits and clocked out at a frame rate of 55 Hz (which is well above the 10 Hz rate required for CLOUD). These images are "grabbed" by a specially-adapted PC, with dual Pentium processors. The PC has two PCI cards which provide the two camera interfaces; the cards are linked to ensure that there is no variation in timing between the two cameras. Exposure time and frequency are derived from programmable crystal-based oscillators. The operating system is Microsoft Windows NT Workstation. The computer system captures two synchronised video streams from the two CCD cameras. It then reconstitutes the video images and stores them on a computer network for detailed off-line analysis. The data is buffered and sent to the computer via differential parallel cables. These also carry camera control signals generated by the computer to

start and stop the light collection on the CCDs and to trigger the data transfer. The exposure time and frequency can therefore be selected by the operator.

The video data is packed by the PCI cards and temporarily stored in two buffer sets in main memory. As the buffers become full, the data is transferred to four SCSI disk drives, each 9 Gb in size. This is sufficient for about 36 min continuous operation at the full rate of 1 Gbyte/min (50 Hz). Each image is divided into 4 and each quarter image is stored on a separate hard drive. For data analysis, the reverse process takes the quarter images from each hard drive in the correct sequence and rebuilds the original full frame. These frames are then written out to the network disk as FITS images for compatibility with many different software packages. During normal operations, the workload is shared by the two processors. Two small live images can be displayed together with the buffer-filling status to allow the computer operator to monitor the performance of the system.

This system currently exists and is available for the CLOUD experiment. However, we are planning to upgrade the cameras to use newer CCD chips with a smaller pixel size and more pixels per chip.

Optics for the cloud chamber: For the performance figures presented in this section, we will assume that each CCD camera has an upgraded chip of 1024 (h) $\times$ 2048 (v) pixels, with a pixel size of 8×8 μm^2 and an active area of 8.2 (h) $\times$ 16.2 (v) mm^2. Since many CCD chips are already on the market with higher specifications,[15] the figures presented here should be considered as conservative.

The CCD cameras are arranged in a stereo pair as indicated in Fig. 31. The optics are adjustable between a wide field-of-view and a narrow one. The former can be used to simultaneously measure regions of the chamber exposed to beam and not exposed. This requires a wide illumination field, which is provided by a xenon flash lamps mounted at the top window. This produces dark-field-illumination, i.e bright droplet images on a dark background. The flashlamps provide 100 J/pulse at up to 10 Hz; the power source is a 100 μF capacitor-bank charged to 1500 V. Experience with the 38 cm Missouri-Rolla chamber has shown, for xenon flash illumination, the scattered light intensity from a droplet is directly proportional to its radius in the range 2–20 μm. (This was the limit of the measurement; the proportionality probably continues either side of this range.) This indicates that the pulse height information from the CCD will provide measurements of the radii of individual droplets.

An alternative illumination scheme is provided by xenon flashlamps along the viewing direction ("ringflash" in Fig. 31). UV-absorbing filters ($\lambda_{min} = 450$ nm) are used to avoid photo-ionisation reactions inside the chamber. To obtain the best sensitivity at high droplet number densities, only the shallow region corresponding to the depth-of-focus of the CCD cameras is illuminated (see Table 4). This is achieved by focusing light from the upper xenon lamp with a cylindrical lens and collimating the beam with slits. The narrow field-of-view optics is optimised for measurements recorded at the same time as the CAMS detector, where a small volume within the acceptance of the cameras is illuminated by a narrow laser beam.

Some representative choices of the optical parameters are indicated in Table 4. For all

[15] An example is the Kodak KAF-6303 which has 3072×2048 pixels, with a pixel size of 9×9 μm^2 and an active area of 27.6×18.5 mm^2.

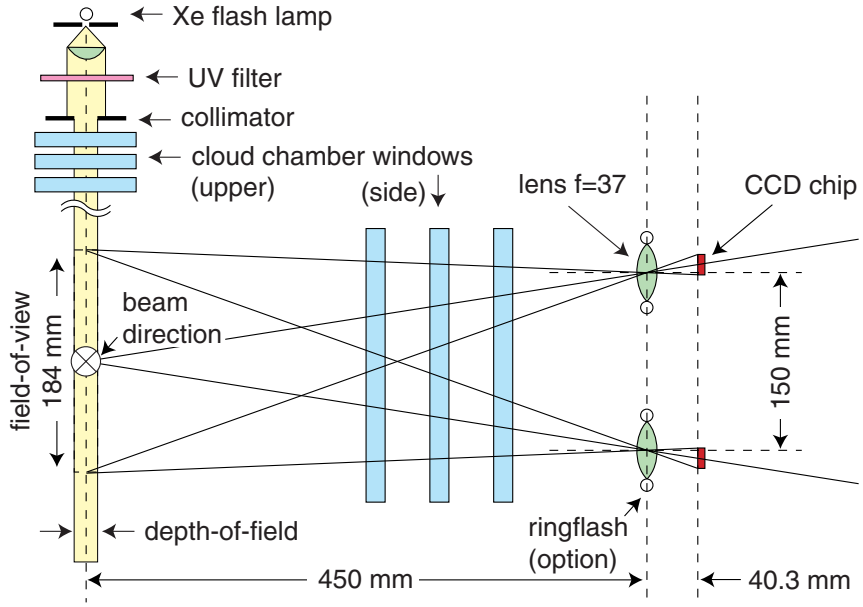

Figure 31: CCD camera optics and xenon flash illumination for the wide field-of-view.

Table 4: Optical parameters of the CCD camera system. The figures assume a CCD chip of 1024 (h) × 2048 (v) pixels, with a pixel size of 8 × 8 μm^2 and an active area of 8.2 (h) × 16.2 (v) mm^2.

Parameter		**Wide field-of-view**		**Narrow field-of-view**
Lens focal length	[mm]	37		200
De-magnification (object/image distance)		11.2		1.25
Transverse field-of-view in chamber (h × v)	[mm^2]	92 × 184		10 × 20
Lens aperture (f-number)		3.5	5.6	5.6
Lens useful diameter	[mm]	11	6.6	36
Depth-of-field in object space (chamber)	[mm]	10	26	0.8
Diffraction resolution limit of image[§]	[μm]	4.2	6.8	6.8
Diffraction resolution limit in object space[†]	[μm]	90	90	10
2-droplet resolution[⋆]	[μm]	180	180	20
Maximum droplet number concentration[‡]	[cm^{-3}]	1250	500	2×10^5

[§] Full width of diffraction spot, at wavelength $\lambda = 500$ nm.
[†] Limited by pixel size, not image diffraction.
[⋆] Assuming a centre-to-centre droplet separation of two pixels.
[‡] Assuming 10% pixel occupancy. For the wide field-of-view optics, we assume the xenon flashlamp is collimated to illuminate the depth-of-field region. For the narrow field-of-view optics we assume CAMS laser beam illumination, with 20 mm of beam path subtended by the observation cone.

lens apertures larger than F5.6, the 8 μm pixel determines the size of a droplet image; this is larger than the diffraction limit of lens and the physical droplet size, for diameters below 10 μm. The wide field-of-view has a transverse size of about 9.2 (h) $\times$ 18.4 (v) cm^2 and a depth-of-focus of 11–26 mm. A large field-of-view limits the maximum droplet number density to values of about 10^3 cm^{-3}, which is adequate for most studies. If necessary, slightly higher values can be achieved by restricting the illumination to a shallower depth-of-field. In contrast, a narrow field-of-view allows measurements up to much higher droplet number densities of about 10^5 cm^{-3}.

4.4 Gas and aerosol systems

4.4.1 Overview

A schematic of the gas and aerosol supply and analysis systems is shown in Fig. 32. The supply system involves four components: carrier gas, water vapour, aerosols and trace gases. The carrier gas is either pure artificial air (80% N_2, 20% O_2) or argon. Water vapour, aerosols and trace gases are mixed into this stream at the desired levels (see Table 3). The water vapour and aerosol systems are described in more detail below.

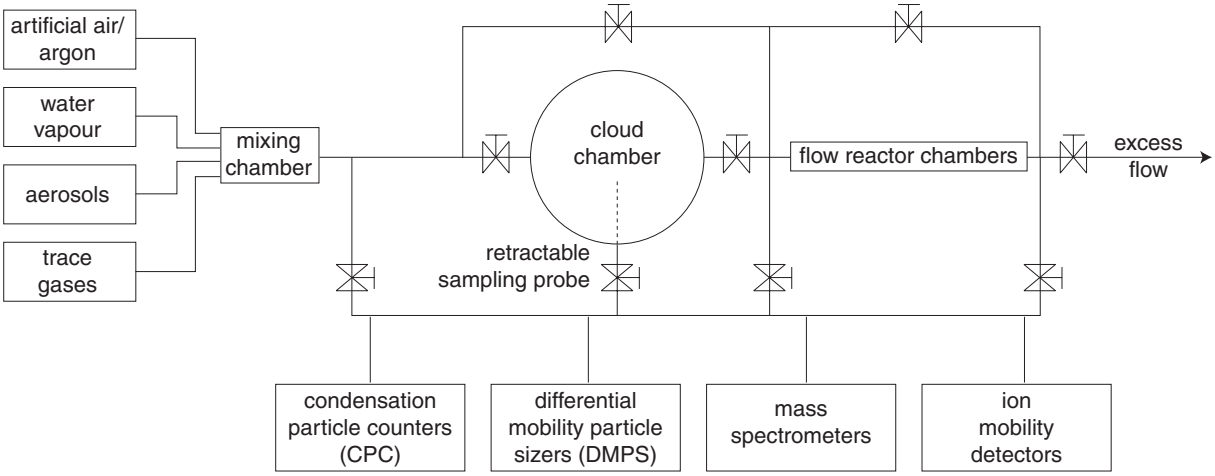

Figure 32: Schematic showing the elements of the gas and aerosol supply systems and the physical and chemical analysis systems.

4.4.2 Water vapour system

The water vapour content in the chamber will be set by two techniques: a) a liquid or ice film on the top of the piston and b) vapour and carrier gas introduced from an external humidifier. For most experiments, the saturation ratio before expansion will be $p/p_0 = (100.00 \pm 0.05)\%$, where p is the partial pressure of the water vapour and p_0 is the saturated vapour pressure over a plane surface of water (or ice) at this temperature. (The error of 0.05% corresponds to a temperature variation of 0.01 K.) The vapour will be provided by a liquid or ice film covering most of the top of the piston and maintained at the precise ambient temperature. This design has several important advantages: a)

the amount of liquid needed is low and thus can be high purity and also be changed easily if contamination of the liquid film is suspected, b) it allows the introduction of liquids other than water if needed, and c) the film will cover most of the piston top but will not touch the walls, thus eliminating problems that might occur when the liquid film (water) freezes.

For experiments that require initial saturation ratios in the range $50\% < p/p_0 < 100\%$, an external humidifier will be used. A straightforward method to produce a very precise water vapour content from an external source is to use the saturated vapour and carrier gas from a liquid pool that is very well temperature regulated, as indicated above. The vapour and carrier gas can then be accurately diluted to produce a known (water) vapour concentration. In order to avoid any problems due to contamination of the surface of the water with surfactants, the surface is continually renewed by flowing the water over many glass rods in a tower structure through which the carrier gas flows.

4.4.3 Aerosol system

Particle generation: Aerosol particle generation for the project will depend on the particle size required. To generate submicron particles for laboratory experiments, two standard techniques are available. Nebulizers are used to generate particles in the size range of 10–1000 nm. In a nebulizer, a small liquid flow is introduced into a pressurised air flow through a nozzle. The liquid flow is distributed into small droplets, which can be made to evaporate after the nozzle by adjusting the fraction of the volatile compound in the liquid. The final particle size is set by the fraction of residual non-volatile component in each droplet [84, 85]. When a slightly smaller size range is needed e.g. particle diameter 3–200 nm, a technique based on evaporation and condensation of either salts or metals can be used [86].

Determination of number concentration of particles: Detection of submicron particles is usually carried out by use of condensation particle counters (CPC) or faraday cup electrometers (FCE). The most appropriate instruments are commercial CPCs by TSI. One model is used to determine number concentration of particles with diameters exceeding 10 nm [87]. Another instrument, especially suitable for ultrafine particles can be used for particles with diameters exceeding 3 nm [88]. A CPC connected with a pulse height analyser can also, in certain conditions, measure the size distribution in a very narrow size range of 3–10 nm [89]. Smaller sizes can only be measured in the main cloud chamber.

Size classification of particles: The above particle counters (CPC 3010 and CPC 3010) can be used in combination with a size classification method, based on the electrical mobility of particles, to provide a differential mobility particle sizer, DMPS [90, 91]. Alternatively, as a more novel technique, they can be used in a scanning mode as a scanning mobility particle sizer (SMPS). High performance of these instruments requires a well controlled flow arrangement [92], determination of size resolution of the size classification [93] and control of the artificial electrical charging of particles [94, 95]. The mobility spectrum obtained from these measurements can be inverted to obtain the number size distribution of the particles [96] with a time resolution of 1-10 min.

Transmission efficiency: In general, submicron particles are quite efficiently transported in small tubes by standard carrier gas flows. The main mechanisms for transport losses are deposition onto tubing walls by diffusion, gravitational settling of particles in the tubing, as well as inertial losses of particles at sharp tube bends. Diffusion losses are only significant for particles smaller than approximately 20 nm [97]. These remaining processes are usually significant only for particles sizes exceeding about 100 nm [84, 85]. For particle size range of 10-1000 nm, usually no other processes affect the transmission in flow tubes. However if high electrical fields or large thermal gradients are present in the tubing, then electrical precipitation and thermophoretic effects may become important.

4.5 Analysis of trace gases and ions

4.5.1 Overview

We will analyse the trace chemical species and ions expected from the flow chamber, as well as any new chemicals that may be formed. Trace gas analysis will be performed by two mass spectrometers. A third mass spectrometer (PITMAS) will determine the chemical composition of ions, and ion mass and mobility spectrometers will detect growth processes, which are crucial for the observation of ion-assisted particle production.

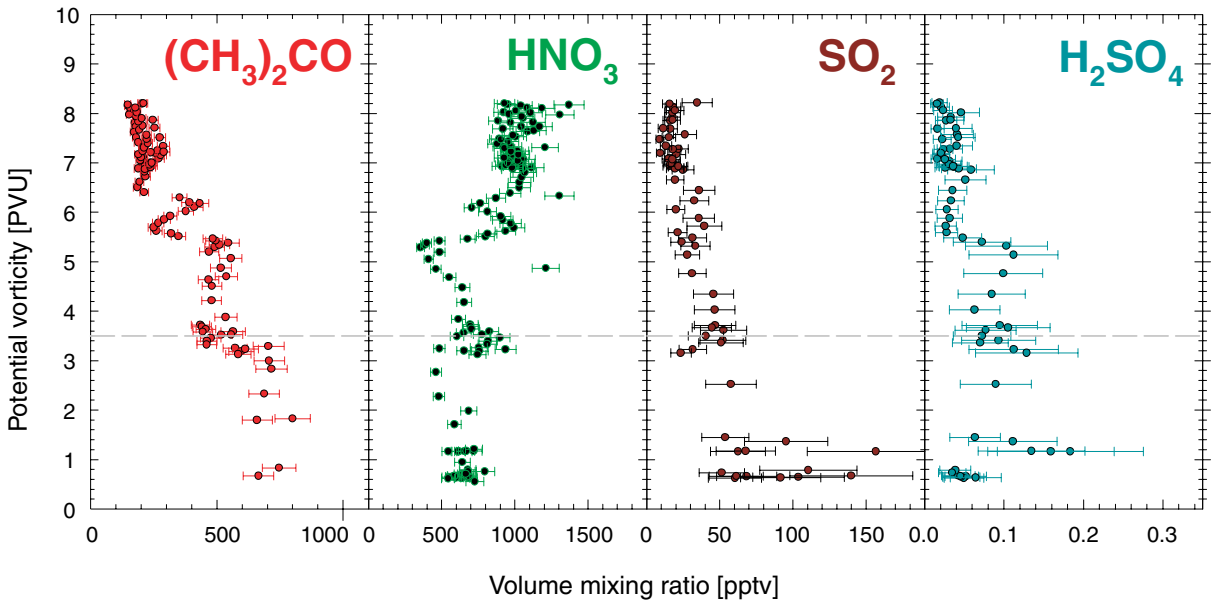

Figure 33: Measurements made with an aircraft-based Chemical Ionisation Mass Spectrometer (CIMS) by MPIK-Heidelberg. The data show vertical profiles of the mixing ratios of $(CH_3)_2CO$ (acetone), HNO_3, SO_2 and gaseous H_2SO_4 over central Europe in December 1995. The altitude is indicated as potential vorticity (PV) [103]. Typically the tropopause is located around 3.5 PVU.

4.5.2 Chemical ionisation mass spectrometer

The MPIK-Heidelberg Chemical Ionisation Mass Spectrometer (CIMS) measures trace gases with high sensitivity (typical detection limit $\sim$ 1 pptv[16]) and fast time response ($\sim$ 10 s). The CIMS-instrument consists of an ion flow reactor coupled to an efficiently-pumped linear quadrupole mass spectrometer. The instruments used have been developed and successfully employed by the MPIK-Heidelberg group for atmospheric measurements at ground level as well as on research balloons, rockets, and aircraft [98]–[102]. A typical measurement is shown in Fig. 33. In a recent development, the linear quadrupole mass spectrometer has been replaced by a quadrupole ion trap mass spectrometer (PITMAS) which has been modified for the application to measurements of trace gases in the atmosphere [104]. The high duty cycle which is offered by this instrument is of advantage for the measurements of trace gases down to the sub-pptv range. In the CLOUD experiment, CIMS will be used for measurements of the following trace gases: H_2SO_4, SO_2, HNO_3 and NH_3. These are potentially important with respect to ion-induced aerosol formation under tropospheric conditions. Typical volume mixing ratios of these gases in the "clean" upper troposphere are the following: 0.05–0.5 pptv (H_2SO_4), 10-1000 pptv (SO_2), and 100–1000 pptv (HNO_3). For upper tropospheric conditions the CIMS-detection limits for measurement of these trace gases are currently estimated to be 0.05 pptv (H_2SO_4, 1 minute time resolution), 1 pptv (SO_2, 30 s time resolution), and 50 pptv (HNO_3, 10 s time resolution).

4.5.3 Time-of-flight (ToF) mass spectrometer

The ToF ion mass spectrometer developed by St. Petersburg-Aarhus uses pulsed electron impact ionisation of a gas sample, extraction by an electric field of the produced ions, and subsequent drift of the ions to a detector that counts the ions as a function of the time of arrival. The instrument will be used to measure changes of the chemical composition of the gas mixture from the flow reactor chambers or the cloud chamber (extracted with the sampling probes). The main advantage of ToF mass/charge analysis in comparison with other methods is the possibility to register simultaneously ions over a very wide range of masses and with relatively high mass/charge resolution. The measurements are made on-line and the results are available in real-time. The ToF analysis includes the following steps:

1. *Taking a gas sample:* A large reduction of pressure is necessary because a pressure of less than 10^{-4} Torr is required by the ToF spectrometer. Two techniques are planned for use. The first is short sampling, synchronised and delayed relative to the particle beam for studies of the time dependence of chemical processes. The second is sampling into a buffer volume with long-term analysis to increase sensitivity to trace gases. In both cases there is a problem of maintaining the initial composition of gas mixture. Therefore teflon or proper plastic with non-nucleating surface can be chosen in the valves.

2. *Ionisation of gas sample:* Electron impact ionisation at single collision conditions is planned. In many cases non-dissociative ionisation prevails or dissociation fractions

[16] *pptv* denotes parts per trillion by volume.

are known. In some specific cases the identification of the initial composition of molecules will be verified by calibration experiments with mixtures having known composition.

3. *Registration of ion signals:* Ions are registered in current or in counting mode. Both will be used to provide at the same time high sensitivity for weak lines (counting mode) and the ability to deal with the large number of ions in the strong lines (current mode). This is facilitated by the fact that the intense lines correspond to masses less than 40 amu and the interesting trace lines to larger masses.

The ToF spectrometer has the following performance:

- Ion mass range 1-2000 a.m.u.
- Mass/charge resolution power $M/\Delta M = 200$.
- Maximum ratio of ion line intensities at simultaneous registration: 10^4.
- Minimum ion line signal intensity (equal to background counting rate): 0.01 Hz.

The mass range and the resolving power can be improved if necessary. A typical experimental spectrum is shown in Fig. 34 [105]. It shows on semi-logarithmic scale the composition of ions formed by ionisation of ambient air and Ar. As can be seen in Fig. 34 there are lines corresponding to formation of singly and multiply charged ions of different gases, molecular ions and their dissociation fragment and also to isotopes of ^{36}Ar and ^{38}Ar having low relative concentrations (about 0.34% and 0.06% respectively).

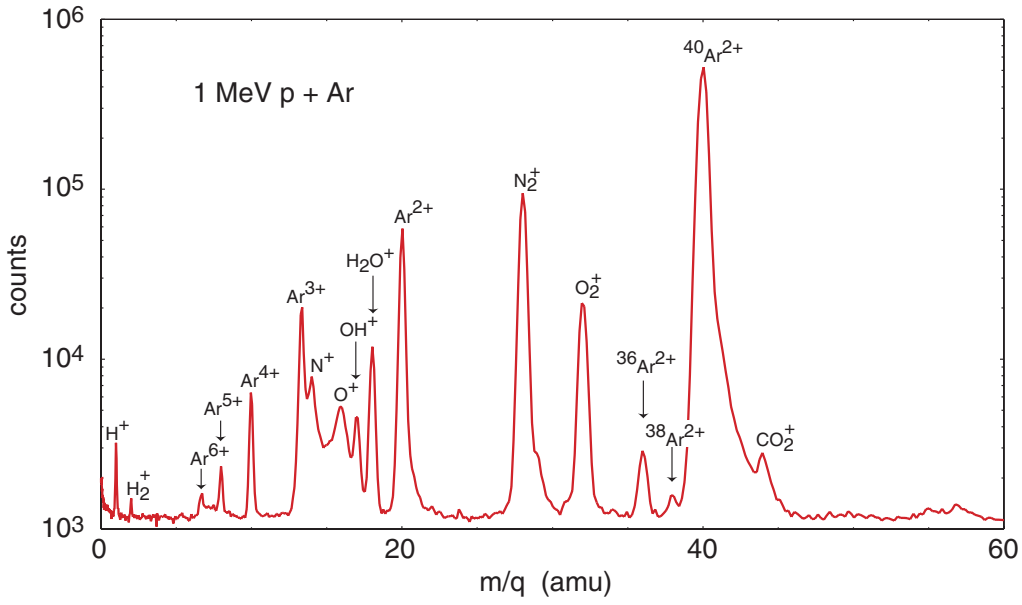

Figure 34: Time-of-flight mass spectrometer measurements of the ions formed in Ar and residual gas by 1 MeV protons [105].

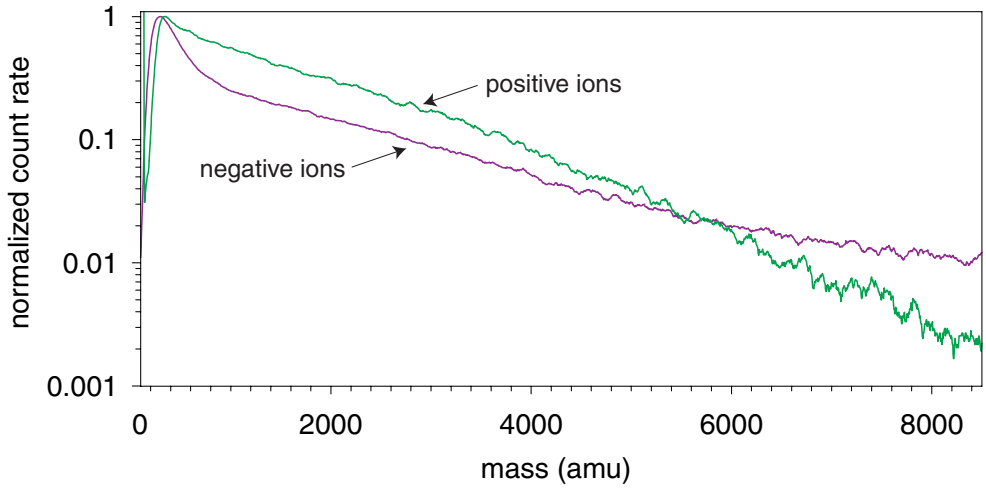

Figure 35: Measurements made with an Ion Mass Spectrometer (IOMAS) by MPIK-Heidelberg. The data show high-pass-mode mass spectra of positive and negative ions measured in the exhaust of a jet aircraft on the ground. The plume age is around 0.1 s, with 2 mg/kg fuel sulphur content, 30% engine power setting and 2.2 m distance between the exit of the engine and the sampling point. The initial rise of the ion signal is a well known instrumental effect. The spectra indicate the presence of very massive ions, above even 8500 amu. The fractions of ions with masses exceeding 8500 are 0.0023 (for positive ions) and 0.01 (for negative ions).

4.5.4 Ion mass spectrometers

The MPIK-Heidelberg IOMAS (Ion Mass Spectrometer) and quadrupole ion trap mass spectrometer (PITMAS) instruments measure the mass distribution of positive and negative ions with mass numbers $m \leq 10\,000$ (IOMAS) and $m \leq 4000$ (PITMAS). IOMAS is a linear quadrupole mass spectrometer which is usually operated in a high-pass-mode (HPM). The HPM is very sensitive and particularly well suited for situations with numerous ion species each having only a small fractional abundance. The present mass range of IOMAS extends from gaseous molecules having mass numbers of several hundred up to very massive ions having diameters in the range of several nm. Therefore it covers the mass range of small clusters which are formed subsequently during the initial steps of nucleation. These clusters, however, are too small to be detectable by condensation nucleus counters (CPCs)—although they are of course readily detected in the CLOUD expansion chamber when operated with a relatively large expansion. The performance of IOMAS has been demonstrated recently in flow reactor experiments made at MPIK-Heidelberg [106]. In these experiments large cluster ions have been produced by adding of sulphur dioxide and water vapour into a flow reactor where ions and OH radicals were produced. By varying the amounts of sulphur dioxide and water vapour, efficient growth of cluster ions consisting of numerous H_2SO_4/H_2O molecules could be observed. In addition, our measurements of the exhaust from jet aircraft made both on the ground and in flight show that very massive ions with mass numbers exceeding 10000 are present [107, 108] (Fig. 35). These measurements confirm the importance of ions in the formation of volatile aerosols in the exhaust from jet aircraft, which has been suggested recently

[109, 110]. Evidence for the existence of "chemiions" in the exhaust of jet aircraft also comes from measurements of the total ion concentration in the exhaust of a jet aircraft recently made by MPIK-Heidelberg [111], and from mass spectrometer measurements of negative chemiions with mass numbers larger than 450 [112].

In addition, the MPIK-Heidelberg PITMAS instrument would be available for chemical identification of complex ions produced in the CLOUD experiment. PITMAS offers a particularly attractive addition on the analytical potential, namely fragmentation studies of mass-selected ions. PITMAS can be operated in two modes. The first of these is a standard mode that produces ion mass spectra with a very high mass resolution and a large mass range (up to $m = 4000$). Provided that the intensity of an ion signal is sufficient, the second mode allows for specific fragmentation studies of mass-selected ions with mass number up to 2000. In this mode only ions of a single mass are trapped. The kinetic energy of the trapped ions is increased and leads to collision-induced dissociation (CID) through collisions with He atoms that are introduced into the spectrometer. For complex ions or cluster ions, usually several different fragment ion species are produced. The fragment ion pattern is, in most cases, characteristic of a parent ion species. In a second CID step, one of the different fragment ion species can be trapped and a CID study can be made leading to second generation fragment ions. In the same way even higher order generations of fragment ions can be produced [113]. Consider, for example, an ion with $m = 2000\,\mathrm{amu}$. If measured by a conventional ion mass spectrometer giving only m, an identification of the ion will be extremely difficult, if not impossible. By contrast PITMAS has the potential to pin down the identity of the ion. Another application of PITMAS involves trapping of ions with one m and subsequent interaction of the trapped ions with a reagent gas which is introduced into the trap. Thereby ions may be identified due to their different chemical reactivity leading to characteristic product ions.

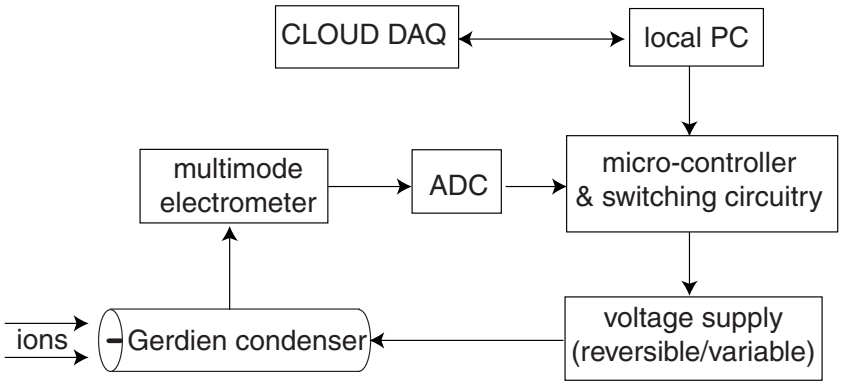

Figure 36: Schematic of the programmable ion mobility spectrometer (PIMS) using a Gerdien condenser.

4.5.5 Ion mobility spectrometer

Mobility-selective ion measurements are required in order to follow the time evolution of small ions through complex clusters into aerosol particles. A flow-driven programmable ion mobility spectrometer (PIMS) [114] based on a classical mobility-selective detector

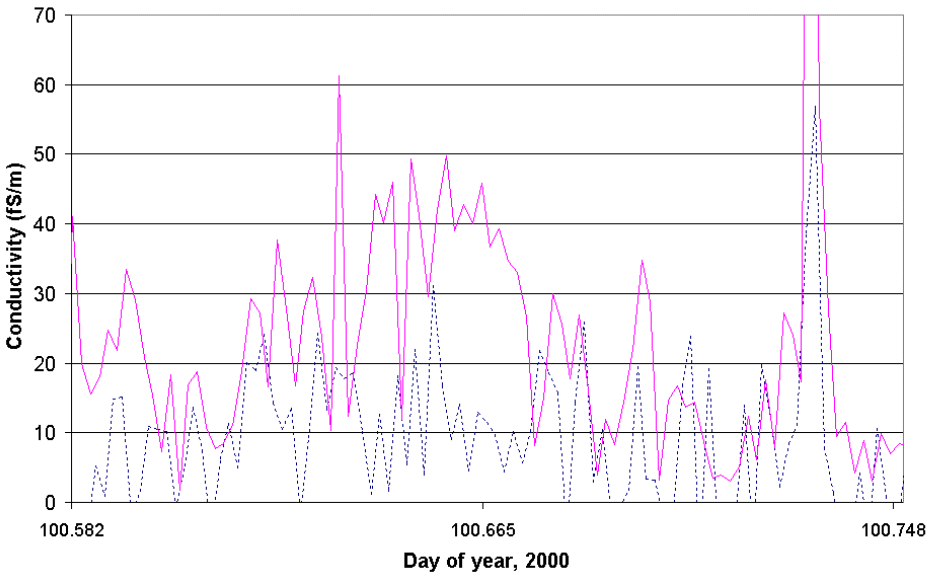

Figure 37: A comparison of air conductivity (which is directly proportional to the ion concentration) measured sequentially using the two modes of a PIMS under fair weather conditions at Reading between 1400 and 1800 BST on 9 April 2000. The solid trace is total conductivity (from positive and negative ions) and the dotted trace is the negative ion conductivity (which is approximately half the total).

(Gerdien condenser) will be employed (Fig. 36). The Gerdien condenser is a metal cylinder that is open at each end and contains an axial electrode set at either a positive or negative potential. The cylinder is enclosed in another metal cylinder which provides a shield. Air containing the ions under analysis is flowed through the cylinder at a known rate and the current is recorded with a femtoammeter.

The PIMS uses technology developed at Reading to measure the low ion concentrations found in the atmosphere at ground level [115]. The Reading ion spectrometer is a fully programmable device which can measure ions self-consistently in two independent modes, as shown in Fig. 37. The PIMS can also be operated dynamically to utilise mobility cut-offs appropriate to the ions produced, which will allow the evolution of the whole ion spectrum to be examined, before the particle measurement system. In addition, the PIMS can measure the total ion concentration, which will permit calculation of absolute concentrations from the ion mass spectrometers.

The ion counters for CLOUD are miniaturised versions of the recent Reading design [115], constructed in a cylindrical geometry from stainless steel and PTFE, with a central platinum wire electrode. In the flow chamber, a cross section of 1 cm will be used to reduce the volume flow rate through the instrument. Adjustment of the bias voltage depending on the flow rate is a simple procedure. Several PIMS detectors measuring different ion mobilities will be arranged sequentially to minimise the flow rate, and to ensure the same sample of air is measured. Techniques have already been developed to reliably measure the very small ion currents involved [116, 117].

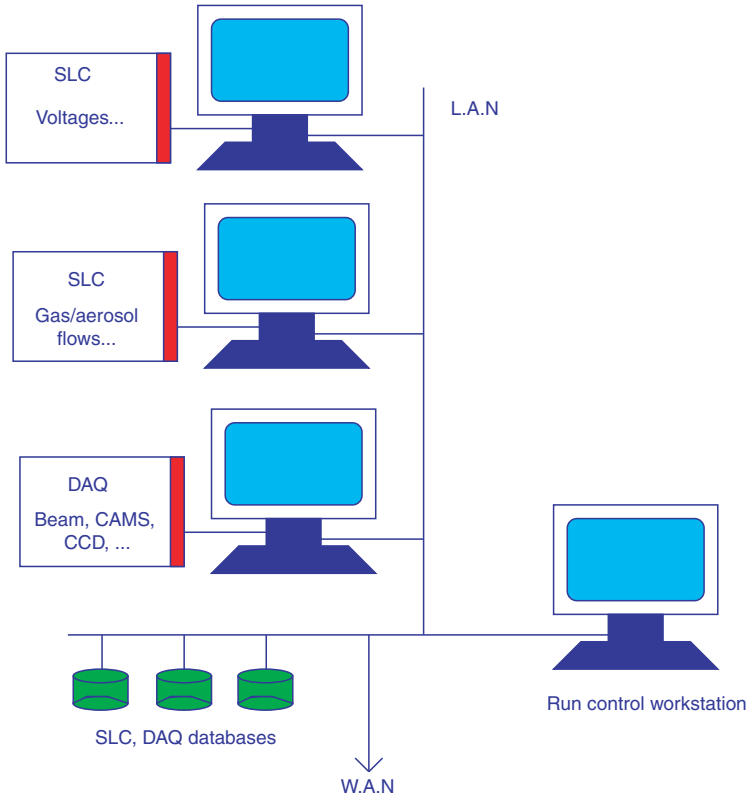

Figure 38: Schematic diagram of the data acquisition (DAQ) and slow control (SLC) systems for CLOUD.

4.6 Data acquisition and offline analysis

4.6.1 Data acquisition and slow control

The CLOUD data acquisition (DAQ) system (Fig. 38) is designed to collect and record a) the operating parameters of the cloud chamber and other detector systems and b) the data from the optical readout systems and other equipment during the periods of beam exposure and droplet growth. It must be be highly flexible in order to accommodate the many different run conditions necessary for the various experiments.

The slow control (SLC) system[17] is responsible for the software control of all operating conditions for the experiment. It includes defining the timing and pressure cycle for the piston expansion/compression, operating the gas valves, controlling the gas and aerosol flow rates, setting the voltages for the field cage electrodes, and setting voltages and other parameters for each of the detector systems.

Functions: The functions of the DAQ and SLC systems are to:

- Provide a user-friendly control of the run conditions, (beam on/off, beam energy, etc.) and of the parameters for the cloud chamber and other detectors.

[17]It is called *slow control* in particle physics terminology since it typically involves timescales of a few seconds rather than the nanosecond or microsecond timescales characteristic of fast logic and data acquisition.

- Implement a readout selection according to the run conditions.
- Digitise, read out and assemble the data of the different detectors into sub-data blocks.
- Assemble the sub-data blocks into full events.
- Monitor the data quality, detect malfunctions and warn the operator.
- Record the events onto permanent storage.
- Monitor and record the parameters of the cloud chamber and other detectors.

Data components: The cloud chamber and detectors produce data which are divided into two different data streams according to their readout period.

- The DAQ data with a readout period ∼msec are generated by the CAMS detector, CCD cameras, aerosol counters, mass spectrometers, ion mobility detector and the beam counter systems. This stream will also include the temperature and pressure sensors for the active volume of the cloud chamber, and the piston hydraulic control and position monitor.
- The SLC data with a readout period ∼sec/min are generated by equipment such as gas flow monitors and the voltage sensors for the field cage.

For each data stream an event builder collects the data and transfers them to disks for permanent storage. Data reduction and formatting can be applied during transfer in order to reduce the event size and therefore the amount of disk space required.

Central control and monitoring: All the control functions of the CLOUD detector will be integrated in order to:

- Support distributed and heterogeneous components.
- Store, retrieve and modify the experimental configuration.
- Store, retrieve and modify the CLOUD detector monitoring parameters.

The CLOUD DAQ and SLC requirements are modest compared with a typical particle physics experiment and can be implemented with standard commercial products. Standard CERN software is available to perform the system integration.

4.6.2 Offline analysis

Implementation of the offline computing environment for CLOUD (Fig. 39) also poses no special difficulties in comparison with present particle physics experiments.

The central part of the environment is a multi-CPU machine, or alternatively a small cluster of several single/double-CPU machines. The platform of choice will be a PC running Linux in view of the high performance and low cost trends. This machine is responsible for:

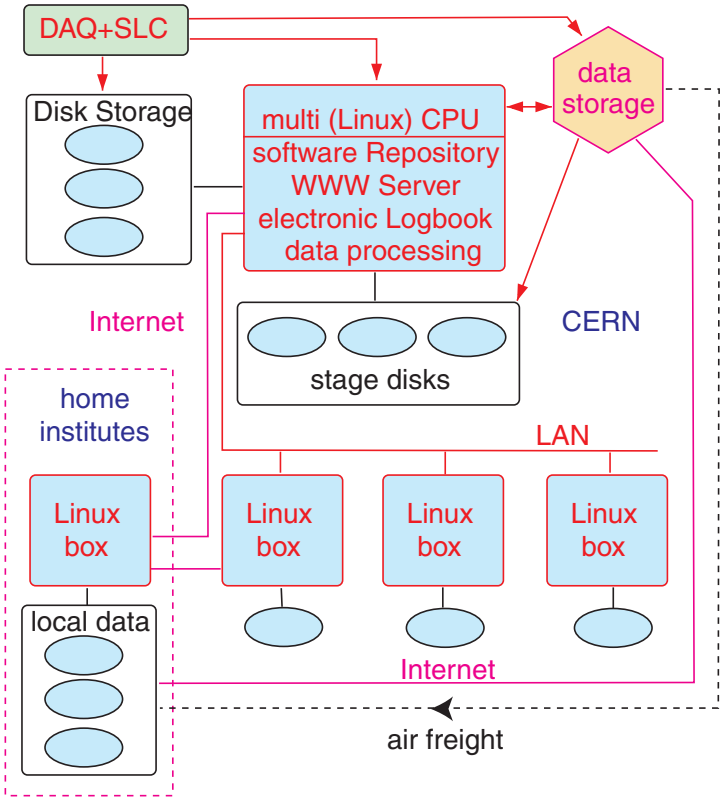

Figure 39: Schematic diagram of the offline computing environment.

- Data processing.
- Maintaining the database of the detector ("electronic logbook").
- Providing a powerful web server which will be linked with the data storage and the database.

The data flowing from the DAQ and SLC will be stored in a mass storage system and also on temporary disks attached to the central machine. This will execute the necessary processing steps, such as reconstruction of information from single sub-detectors and then combined event reconstruction from the whole detector system. The central machine will also manage storage of the processed data onto the same mass storage system.

Stage disks attached to the central machine will provide processed data and, if needed, raw data for the end-user. End-user analysis will be carried out either with a fraction of the CPU of the central machine or with local desktop Linux machines. Home institutions will be equipped by scalable Linux facilities, with a sufficient amount of disk space to fetch—either over the network or by air freight—a subset or else the full data sample for local analyses.

We plan to benefit as much as possible from the ongoing effort of the HEP community in general and of the LHC community in particular towards modern computing solutions, even given the relative smallness of our data sample. As an example the integration with the currently proposed solution for persistency and software architecture will be among the first software development tasks. End-user data analyses will also centre around the software tools of the new generation of experiments, such as ROOT[118] and LHC++[119].

5 Detector performance

5.1 Droplet growth time

5.1.1 Principles of droplet growth

An aerosol will grow by condensation if the water vapour supersaturation exceeds a critical value, which depends on the size and nature of the aerosol (Appendix A.1). Once the growth process has started, it continues since the equilibrium vapour pressure decreases with increasing droplet size. Eventually the growth stops when sufficient water vapour has been removed that the supersaturation is reduced.

The driving force that determines the rate at which liquid mass condenses onto the droplet is the supersaturation relative to the equilibrium value, $SS(r)$:

$$SS(r) \;=\; (S-1) - \frac{a}{r} + \frac{b}{r^3} \tag{1}$$

where S is the water vapour saturation ratio with respect to the vapour pressure over a plane surface of water, and r is the radius of the droplet. The a/r term corresponds to the effect of curvature (Kelvin's equation) and the b/r^3 term corresponds to the effect of dissolved solute (Raoult's law). This is the form of the Köhler equation (Fig. 46).

The growth process of a droplet occurs by diffusion of water molecules from the vapour onto its surface. Associated with the condensation is the release of latent heat, which tends to raise the temperature of the droplet above its surroundings. This increases the rate of evaporation and decreases the rate of growth. The size of this effect is determined by the rate at which heat is conducted away from the droplet by the surrounding gas. The resulting growth rate is given by [120]:

$$r\frac{dr}{dt} \;=\; \frac{SS(r)}{[F_k + F_d]} \tag{2}$$

where F_k represents the latent heat term and F_d the vapour diffusion term. When the droplet becomes sufficiently large, the a/r and b/r^3 terms in Eq. 1 are negligible compared with $(S-1)$, so that $SS(r) = SS$. Integrating Eq. 2 then gives

$$r_t^2 \;=\; r_0^2 + 2\xi t \tag{3}$$

$$\text{where } \xi \;=\; \frac{SS}{[F_K + F_d]} \tag{4}$$

Equations 3 and 4 illustrate the essential feature that the time for a droplet to grow to a radius r_t is $t \propto r_t^2/SS$. A more rigorous calculation of droplet growth is presented below.

5.1.2 Simulation of droplet growth

We have studied the formation and growth of the cloud droplets using a simple convection model describing a rising cloud parcel. We have assumed a constant updraft velocity without entrainment, since we are primarily interested in droplet formation. The air parcel contains aerosol particles, water and the other condensable vapours (nitric acid, hydrochloric acid and ammonia). The aerosol particle distribution is described using four

log-normal size distributions. The first distribution consists of less hygroscopic Aitken mode[18] particles, the second of more hygroscopic Aitken mode particles, the third of less hygroscopic accumulation mode particles and the fourth of more hygroscopic accumulation mode particles.

In the beginning of a simulation (at the cloud base) dry particles are allowed to take up water and the other condensing vapours and reach equilibrium with the ambient air. The air parcel starts to rise and cool adiabatically, the saturation ratio increases, and the vapours begin to condense into the haze particles. The saturation ratio of water vapour rises typically slightly over unity, after which it decreases to a value near unity. Although the water vapour saturation ratio decreases, some particles continue to grow, because they have been activated and a cloud droplet population has formed.

Condensation model: In the model the condensation of the vapours is simulated by numerically integrating a set of ordinary differential equations, based on the model used by Kulmala *et al.* [121]. In the present study we have slightly changed the differential equations describing the change of the masses of the species in the droplet. The rate of change of the mass of the condensing species j in the droplet size class p is obtained from the equation

$$\frac{dm_{j,p}}{dt} \equiv I_{j,p},$$

where the mass flux $I_{j,p}$ is the rate at which the mass of species j transports through a surface area of a droplet in the size-class p. The mass fluxes can be calculated from the matrix equation

$$\begin{pmatrix} B_{11}-1 & B_{12} & \cdots & B_{15} \\ B_{21} & B_{22}-1 & & \vdots \\ \vdots & & \ddots & \\ B_{51} & \cdots & & B_{55}-1 \end{pmatrix} \begin{pmatrix} I_1 \\ I_2 \\ \vdots \\ I_5 \end{pmatrix} = \begin{pmatrix} A_1(S_{1a}-S_1) \\ A_2(S_{2a}-S_2) \\ \vdots \\ A_5(S_{5a}-S_n) \end{pmatrix},$$

where

$$A_j = \frac{4\pi a_p M_j \beta_{Mj} D_{Ij}}{RT_\infty} p_{s,j}(T_\infty)$$
$$B_{ji} = -S_{ja} \frac{M_j L_j}{RT_\infty^2} \frac{L_i}{4\pi a_p \beta_T k} A_j.$$

In the preceding expressions M_j is the molecular mass of species j, L_j is the latent heat of vapourisation, a_p is the droplet radius in the size class p, D_{Ij} is the binary vapour diffusion coefficient of species j in the carrier gas, S_j is the gas phase activity, S_{ja} is the activity over droplet surface (i.e. liquid phase activity $\times$ Kelvin effect), $p_{s,j}$ is the saturation vapour pressure at the ambient temperature T_∞ and k is thermal conductivity of gas mixture. We have adopted the transition coefficients for mass transfer β_{Mj} and for heat transfer β_T from ref. [122]. The preceding equation may be solved by computer using the Gauss elimination method or LU factorisation [123]. The equation couples heat and mass transfer of water and other condensing vapours [124].

[18] Aitken mode aerosols are in the 20–100 nm diameter range whereas accumulation mode aerosols are larger, with diameters of 100–1000 nm.

Droplet growth results in the cloud chamber: Using the condensation models described above we have performed several model studies which have been verified using data measured in Vienna [125]. We have assumed initial aerosol particles of radius about 25 nm. To grow these into droplets of radius 1 μm when the saturation ratio, S, is 1.2 takes less than 100 ms. If $S = 1.02$ it takes about 1 s and if $S = 1.002$ it takes about 10 s. These values can be scaled to other droplet radii and other supersaturations since the growth time $t \propto r_t^2/SS$ (Eqs. 3 and 4), where $SS = S - 1$.

5.2 Sensitive time of the cloud chamber

After an expansion has taken place, heat gradually leaks into the chamber, the supersaturation diminishes and after a certain time (termed the *sensitive time*) condensation can no longer take place on the activated droplets. It is therefore important that the sensitive time is sufficiently long to allow activated droplets to grow at least to the minimum detectable size (about 1 μm diameter).

Immediately after the expansion, the gas temperature has fallen but the walls of the chamber remains at the equilibrium temperature value prior to the expansion. The gas layer close to the walls then begins to heat up, expand and rise by convection. The expansion of the boundary layer causes the gas inside to re-compress adiabatically, which warms it and causes the supersaturation to fall. Because of the low thermal conductivity of air, heat conduction is an insignificant process for re-heating of the central gas volume.

This sensitive time of a cloud chamber, t_s, due to this re-compression process is calculated [126] to have the following dependencies:

$$t_s \propto \frac{L^2 \cdot P}{(\Delta V/V)^2 \cdot T^2} \tag{5}$$

where L is the linear dimension of the cloud chamber, $\Delta V/V$ is the volume expansion ratio, P the pressure and T the temperature. This expression shows that long sensitive times require large chambers since the sensitive time increases as the square of the linear dimension (i.e. as the square of the ratio of volume/surface area, $(V/A)^2$).

The sensitive time is expected to be proportional to P/T^2 (Eq. 5). Since low pressures and low temperatures occur together in the troposphere, these effects partially compensate. However the reduction in pressure dominates and so t_s decreases, e.g. it is reduced by a factor of about two for the conditions corresponding to 10 km altitude.

Equation 5 indicates that the sensitive time increases for smaller expansions (which give rise to smaller temperature differences between the walls and the gas). For small expansion ratios, there is a linear relationship with the resultant supersaturation, e.g. at 298 K (Table 5):

$$\Delta P/P = \gamma \cdot \Delta V/V = [\gamma/(\gamma - 1)] \cdot \Delta T/T = 0.25 \cdot SS, \tag{6}$$

where $\gamma = 1.4$ is the ratio of the ratio of the specific heats for an air-water vapour mixture, and the supersaturation SS is expressed as a fraction. Therefore $t_s \propto 1/SS^2$. Since the droplet growth time $\propto 1/SS$, this increase in the sensitive time at low supersaturations more than compensates for the longer growth time.

Our experience with the 25 cm Vienna chamber indicates a sensitive time of at least 10 s at 2% supersaturation and stp. Droplet number concentrations typically did not

Table 5: Values of the temperature drop, ΔT, and water vapour supersaturation, SS, resulting from a small pressure expansion ratio, $\Delta P/P$. The volume expansion ratio $\Delta V/V = 0.71 \cdot \Delta P/P$. The initial conditions are P = 101 kPa and T = 298 K and $SS = 0\%$ (100% relative humidity).

$\Delta P/P$ [$\times 10^{-3}$]	ΔT [K]	SS [%]	$\Delta P/P$ [$\times 10^{-3}$]	ΔT [K]	SS [%]
0.1	0.009	0.04	1.0	0.085	0.40
0.2	0.017	0.08	2.0	0.170	0.81
0.4	0.034	0.16	3.0	0.255	1.22
0.6	0.051	0.24	4.0	0.341	1.63
0.8	0.068	0.32	5.0	0.426	2.04

exceed 5000 cm^{-3}. Vapour depletion and latent heat production during growth, however, must be quantitatively accounted for, even for growth times less than 10 s. From Eq. 5, the 50 cm CLOUD expansion chamber should therefore have about a factor 4 longer sensitive time under the same conditions. At lower supersaturations, the sensitive time should further increase, proportionally to $1/SS^2$, e.g. by a factor 100 at 0.2% supersaturation. Under these very low supersaturations, the expected sensitive time is therefore above ten minutes. In conclusion, we expect that the sensitive time of the 50 cm CLOUD expansion chamber is sufficient to observe droplet growth at all thermodynamic and water vapour conditions of interest.

5.3 Electric field and charged particle drift

We have made a preliminary study with the GARFIELD program [127] of the electric field produced by of the field cage. The equipotentials are shown in Fig. 40 when the uppermost electrode is set at +500 V and the piston at 0 V, and a linear voltage division is provided for the intermediate electrodes. An electric field of about 1000 Vm^{-1} is produced within the chamber volume, and is sufficiently uniform to perform the required functions, as described in Section 4.2.6.

The drift velocity, v_D [ms^{-1}], of a particle with charge ne [C] in and electric field E [Vm^{-1}] is given by

$$\begin{aligned} v_D &= \mu E, \\ \text{and } \mu &= neB \end{aligned}$$

where μ [$m^2V^{-1}s^{-1}$] is the electrical mobility and B [$mN^{-1}s^{-1}$] is the mechanical mobility. Some values of these quantities for particles of various sizes are given in Table 6.

The drift characteristics of charged particles in this electric field are shown in Fig.41. Small ions can be efficiently cleared from the cloud chamber in about 2 s. Charged aerosols, however, drift much more slowly. In the example shown, 10 nm-diameter aerosols with unit electric charge are swept from the chamber in about 2 minutes. These large

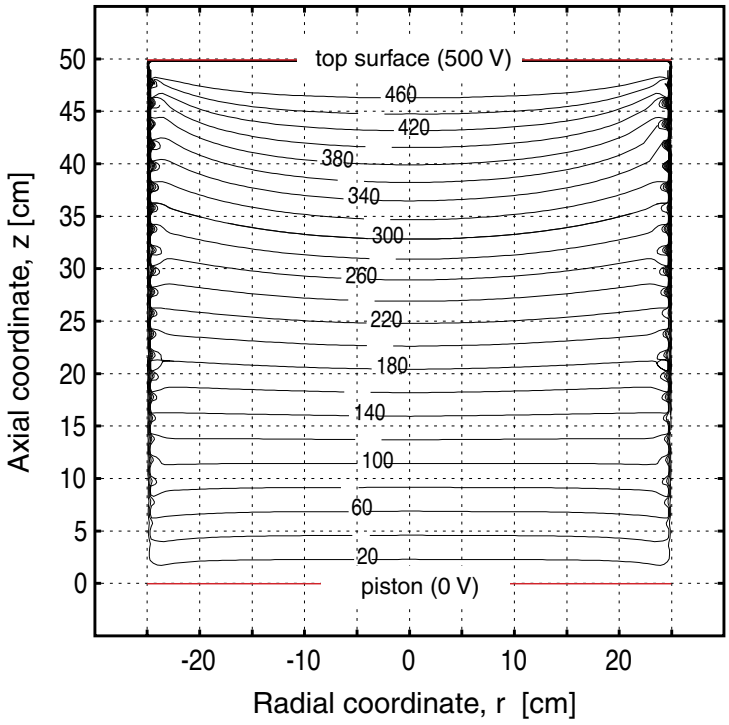

Figure 40: Equipotential contours inside the cloud chamber for linear voltage gradient on the electrodes, and the uppermost electrode at 500 V.

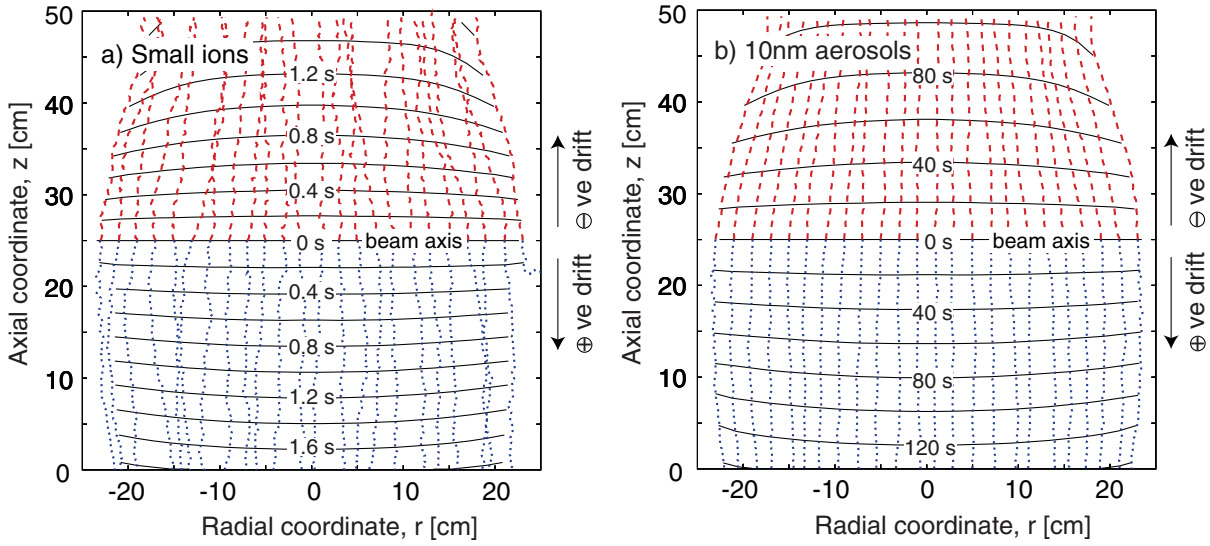

Figure 41: Drift paths and isochronous contours for a) small ions, and b) 10 nm diameter aerosols in air at 293 K and 101 kPa pressure. A total of 24 pairs of particles with unit positive and negative electric charge, respectively, are uniformly generated along the beam axis ($z = 25$ cm) at $t = 0$ s. The electric field is shown in Fig. 40. The scattering of the drift paths is due to Brownian diffusion.

Table 6: Mobilities and diffusion parameters for ions and aerosol particles at 293 K and 101 kPa [84]. The electrical mobility assumes unit charge. Since each of these quantities is approximately inversely proportional to pressure, the values at another pressure P [kPa] can be estimated by multiplying the numbers in the table by 101/P.

Particle diameter d [μm]	**Electrical mobility** μ [$m^2V^{-1}s^{-1}$]	**Mechanical mobility** B [$mN^{-1}s^{-1}$]	**Diffusion coefficient** D [m^2s^{-1}]	**Slip cor. factor** C_c
0.00037†		$4.9 \cdot 10^{15}$	$2.0 \cdot 10^{-5}$	
$\ominus$ve air ion	$1.6 \cdot 10^{-4}$			
$\oplus$ve air ion	$1.4 \cdot 10^{-4}$			
0.001	$1.6 \cdot 10^{-4}$	$1.0 \cdot 10^{15}$	$4.2 \cdot 10^{-6}$	200
0.003	$2.3 \cdot 10^{-5}$	$1.4 \cdot 10^{14}$	$5.8 \cdot 10^{-7}$	73
0.010	$2.1 \cdot 10^{-6}$	$1.3 \cdot 10^{13}$	$5.3 \cdot 10^{-8}$	22
0.030	$2.5 \cdot 10^{-7}$	$1.5 \cdot 10^{12}$	$6.3 \cdot 10^{-9}$	7.9
0.100	$2.7 \cdot 10^{-8}$	$1.7 \cdot 10^{11}$	$6.9 \cdot 10^{-10}$	2.9
0.300	$4.9 \cdot 10^{-9}$	$3.1 \cdot 10^{10}$	$1.2 \cdot 10^{-10}$	1.6
1.000	$1.1 \cdot 10^{-9}$	$6.8 \cdot 10^{9}$	$2.7 \cdot 10^{-11}$	1.2

† Diameter of an air molecule.

differences in electrical mobility can be usefully applied as an experimental tool to provide, for example, mobility measurements inside the chamber, or selective removal of light charged particles while leaving heavier particles. Because of their low mobilities (Table 6), aerosols larger than a few tens of μm in diameter are most efficiently cleared from the cloud chamber either by activation and sedimentation or else by vacuum evacuation of the chamber and then refilling.

5.4 Diffusion effects

5.4.1 Principles of diffusion

In the absence of an electric field, ions and aerosol particles migrate through the cloud chamber by diffusion and sedimentation (gravitational settling). The latter can be completely neglected for the size of aerosol particles under consideration. For example, a 0.1 μm diameter aerosol has a settling velocity of about 1 μm s^{-1} at stp.

The ions and aerosols will diffuse a projected distance

$$x_{rms} = \sqrt{2Dt}$$

in a time t, where D [m^2s^{-1}] is the diffusion coefficient. The diffusion coefficient and the

mechanical mobility B are simply related:

$$\begin{aligned} D &= kTB, \\ \text{and } B &= \frac{C_c}{3\pi\eta d} \end{aligned}$$

where k [JK^{-1}] is Boltzmann's constant, T [K] is the temperature, η [Pa s] is the viscosity of air and d [m] is the particle diameter. The quantity C_c is a dimensionless slip correction factor [84] which is close to unity for particles above 1 μm diameter but increases in magnitude for smaller particles. Values of these quantities for various sizes of particle are given in Table 6.

5.4.2 Ion and aerosol losses to the walls

The finite size of the cloud chamber will result in the loss of charged particles and aerosols to the walls by diffusion. When an aerosol touches a wall, it attaches by van der Waals forces and is lost. For the purposes of the study described here we have also assumed that a small ion is lost (or, equivalently, its charge is neutralised) if it collides with a wall.

We have estimated diffusional losses in the cloud chamber by a 2-dimensional Monte Carlo simulation. Two atmospheric conditions were considered: a) standard conditions (T = 293 K and P = 101 kPa), and b) 10 km altitude (223 K and 26 kPa). In the case of small ions (Figs. 42a and b), the fiducial region in the centre of the chamber is unaffected for periods of about one minute for the 10 km conditions, and for longer periods at ground level conditions. This is to be compared with ion-ion recombination lifetimes in the atmosphere (i.e. for small ion concentrations of a few $\times 1000$ cm^{-3}) of about 5 minutes or less (Section D.1). Since copious small ions can be replenished inside the cloud chamber by the particle beam each 14.4 s of the PS accelerator cycle, these losses of small ions can easily be accounted for and compensated. We also note that these calculations assume small ions, whereas the actual mobilities of the ions will be reduced due to the rapid attachment of molecules and conversion to complex ions (Appendix D).

Aerosols have much smaller mobilities than small ions (Table 6) and so they are expected to be less affected by wall losses. This can be seen in Figs. 42c) and d), which show the losses of 10 nm-diameter aerosols after a period of 1 hr. The losses are relatively modest, even for the 10 km conditions (the 50% loss region is a distance of about 2.5 cm from the walls). Since the width of the loss region scales quite slowly with time as $\sqrt{t}$, the cloud chamber dimensions are sufficient for measuring long aerosol growth processes that may last several hours, without appreciable loss of aerosol particles. In summary, therefore, we conclude that the 50 cm dimension for the cloud chamber is a suitable choice from considerations of diffusional losses of ions and charged aerosols.

5.4.3 Diffusion of beam ionisation

We have also studied the diffusion of ionisation from the beam region of the cloud chamber. The results of a 2-dimensional simulation (Fig. 43) indicate that distinct beam and no-beam regions of the chamber exist only for exposure times less than about one minute. Beyond that time, small ions will be spread throughout the chamber (although, if required, they can be rapidly cleared in a few seconds by application of the clearing field). Therefore

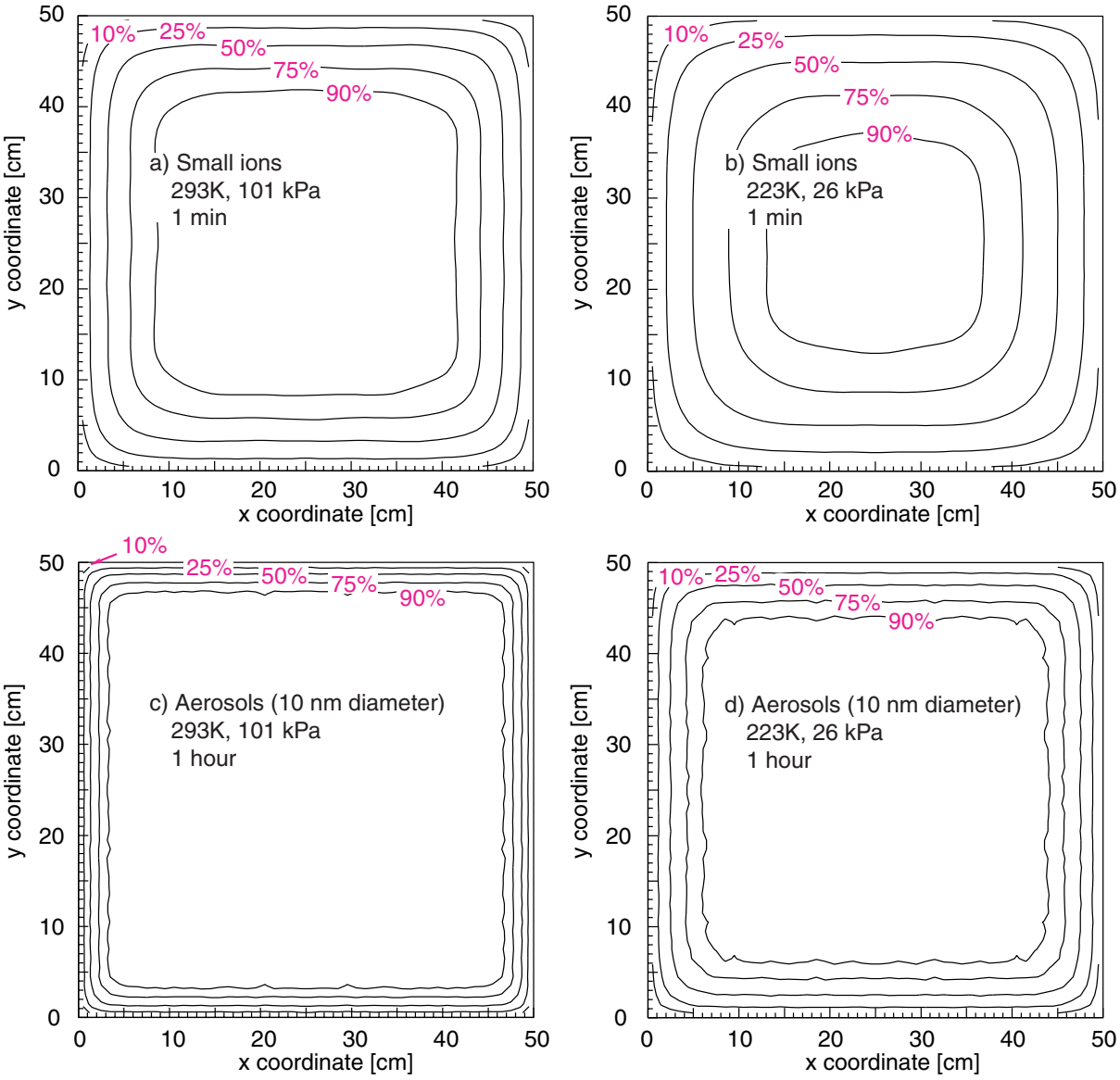

Figure 42: Wall losses of particles in the cloud chamber due to thermal diffusion. The upper plots show the number density of small ions after a time $t = 1$ minute at a) 293 K and 101 kPa (standard conditions) and b) 223 K and 26 kPa (10 km altitude). The lower plots show the number density of 10 nm-diameter aerosols after a time of 1 hour at c) 293 K and 101 kPa and d) 223 K and 26 kPa. A particle is assumed to be lost if it touches one of the walls (which are located at the boundaries of the plots). The initial charged particle distributions were generated uniformly in x and y in the range $0 < x, y < 50$ cm. The contours indicate the fraction of the original number density of particles remaining after the indicated times. The losses can be estimated at other times by scaling the distance between a contour and its nearby wall as $\sqrt{t}$.

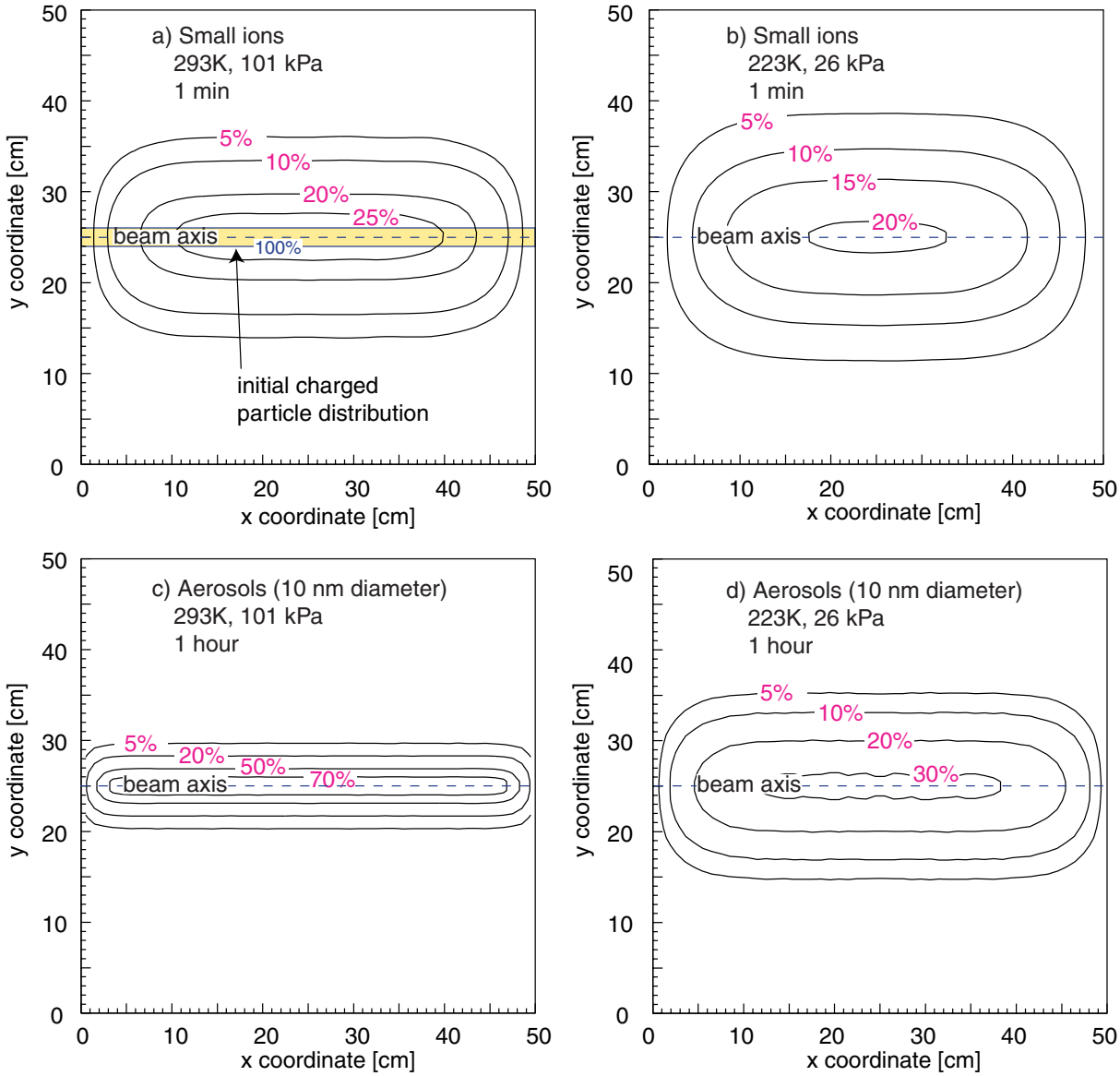

Figure 43: The spreading of charged particles from the beam region of the cloud chamber due to thermal diffusion. The upper plots show the number density of small ions after a time $t = 1$ minute at a) 293 K and 101 kPa (standard conditions) and b) 223 K and 26 kPa (10 km altitude). The lower plots show the number density of 10 nm-diameter charged aerosols after a time of 1 hour at c) 293 K and 101 kPa and d) 223 K and 26 kPa. The initial charged particle distributions were generated according to the beam profile: a Gaussian distribution in the y projection, centred on $y = 25$ cm and with $\sigma_y = 0.4$ cm, and a uniform distribution in the x projection. The contours indicate the number density of charged particles after the indicated times. A figure of 100% corresponds to the original particle density at $t = 0$, averaged over a 2-cm-wide bin centred on the beam axis (as shown in panel a)).

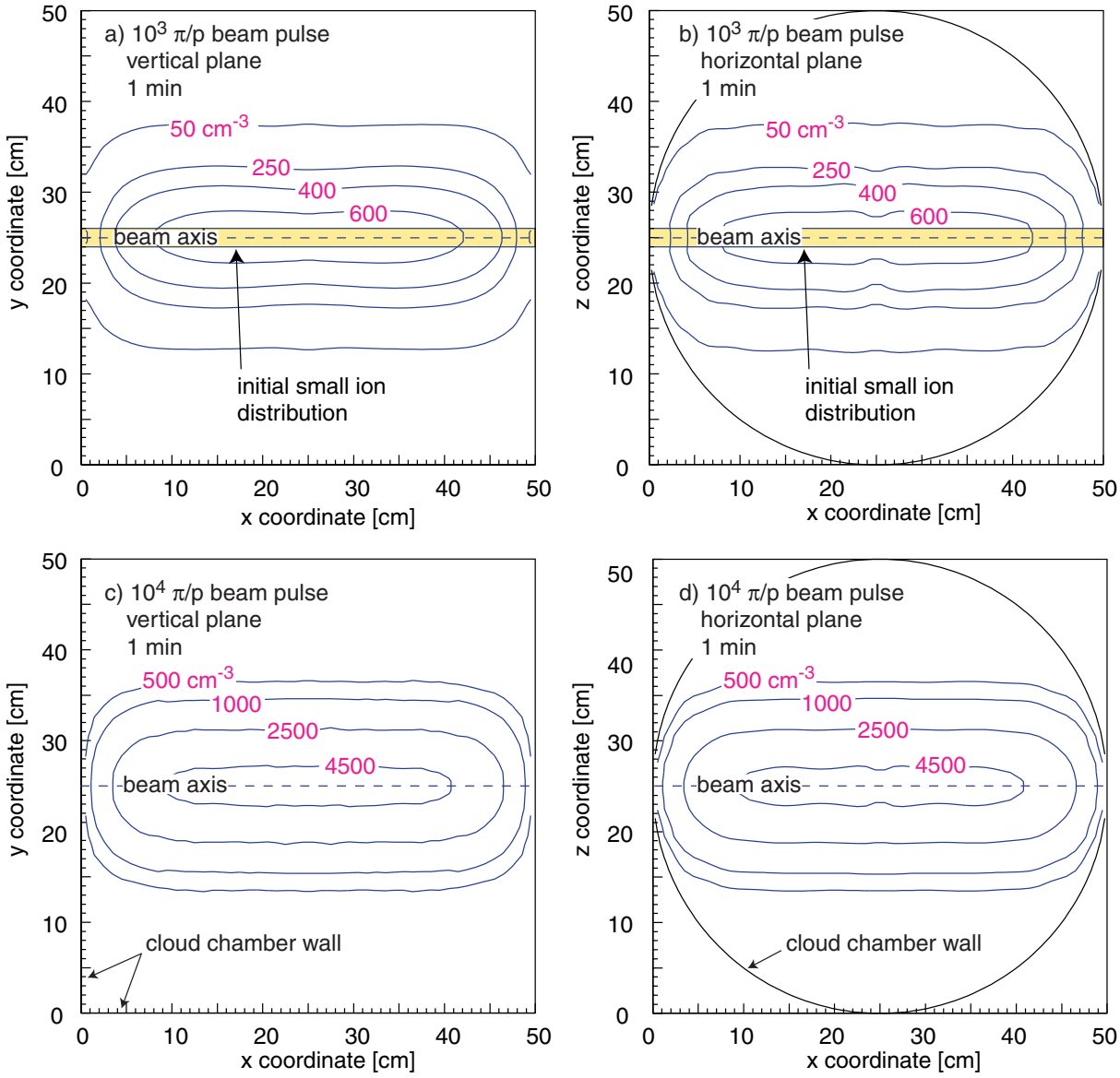

Figure 44: The small ion concentrations (ion pairs cm^{-3}) in the cloud chamber one minute after the passage of a beam pulse, at 293K and 101 kPa (standard conditions). The upper figures correspond to a beam pulse of 10^3 π/p and show the concentrations in a) the vertical (xy) plane and b) the horizontal (xz) plane through the beam axis. The lower figures correspond to a beam pulse of 10^4 π/p in c) the xy plane and d) the xz plane. Both thermal diffusion and ion-ion recombination effects are included. The initial small ion distributions were generated according to the beam profile as described in the caption for Fig. 43.

experiments that involve beam exposure times of more than about one minute will require separate runs for the beam/no-beam measurements. We note that the charged particle and ion profiles inside the chamber can be measured experimentally with deep piston expansions that activate all particles and small ions into droplets.

In order to determine the beam intensity required to reproduce natural levels of ionisation, we have performed a 3-dimensional simulation including the effects of ion-ion recombination. Figures 44 c) and d) show that the ion-pair concentration in the region around the beam about one minutes after a single pulse of 10^4 π/p is similar to the natural concentration at 15 km altitude (i.e. a few $\times 10^3$ i.p. cm^{-3}, see Fig. 50). The effects of ion-ion recombination losses can be seen by comparing the results at a factor 10 lower beam intensity (Figs. 44 a) and b)), which indicate a smaller reduction (factor 7.5) in ionisation concentration.

6 Data interpretation and cloud modelling

The purpose of these investigations is twofold. Firstly, we will use the laboratory results to incorporate ion-mediated aerosol and cloud processes into models. Secondly, we wish to establish whether the experimental results have important consequences for the behaviour of aerosols and clouds in the atmosphere.

Although it is clear that atmospheric ion formation has the potential to influence aerosol and cloud processes, the significance of cosmic rays must be evaluated within the natural variability of other parameters that influence aerosols and clouds. Ultimately, modelling within the CLOUD project must address these issues and, specifically, should:

1. *Obtain a quantitative understanding of the effects of ionisation on aerosols and cloud droplets, including ice formation.* This will be achieved by comparing cloud chamber and aerosol flow chamber observations with simulations using both an aerosol and a cloud microphysical box model.

With regard to aerosols:

2. *Test the importance of ion effects on aerosols under atmospheric conditions* for different cosmic ray fluxes and compare the magnitude of the ion effect on aerosols with the range of natural variations in other parameters. This will be achieved by performing aerosol box model simulations under atmospheric conditions. This work will focus particularly on the aerosol properties that are important for cloud formation.

With regard to clouds:

3. *Develop parameterisations of droplet activation and ice formation suitable for inclusion in cloud models.* This will be achieved by comparing box model simulations of droplet activation and freezing with cloud chamber results.

4. *Assess whether the direct effect of cosmic rays on cloud droplets and ice nucleation has a discernible effect on cloud formation and development.* This work will involve simulations of different cloud types under atmospheric conditions for a range of cosmic ray fluxes typical of their variation with altitude.

5. *Assess the relative importance of cosmic rays on cloud development.* The effect of ion formation will be compared with natural variations in other parameters.

6.1 Modelling of aerosol processes

6.1.1 Evaluation of experimental results

Aerosol microphysical models will be used to simulate the formation, growth and coagulation of aerosols measured by CLOUD. Radius-resolved models of H_2SO_4–H_2O aerosols including the processes of nucleation, coagulation, evaporation and condensation are appropriate for this task. Such models exist at the University of Helsinki and the University of Leeds. These models simulate the competition between condensation of H_2SO_4 on existing aerosols and on new aerosols, leading to formation of stable clusters. A recent study by Yu and Turco [5] has demonstrated the importance of air ions in the formation of new aerosols in the natural environment, although the potentially important process of attachment of air ions onto existing aerosols [128] was not considered. The magnitude of such effects remains uncertain and should be constrained in the models by comparison with experimental results from CLOUD.

The models, including ion-mediated nucleation and coagulation, will be compared with results from the cloud chamber and flow chamber, with and without the simulated cosmic ray source. According to Fig. 16, there are three processes that should be constrained in model simulations of the experimental results:

Charge-enhanced nucleation: Experiments investigating ion effects on nucleation of H_2SO_4/H_2O and $H_2SO_4/H_2O/NH_3$ aerosols will be carried out in the flow chamber and expansion chamber. The results will be compared with the classical ion-induced nucleation theory. Possible enhancements with respect to the classical nucleation theory will be parameterised in terms of gas concentrations, temperatures, and ionisation rates.

Charge-enhanced growth of nucleated clusters: The growth rate of freshly nucleated clusters can be affected by charges carried by the nuclei. The Helsinki group is developing a theory for the enhancement of the condensation rate of H_2SO_4 molecules on charged clusters due to ion-dipole interactions. The theory will be tested against growth experiments carried out with the CLOUD apparatus.

Charge-enhanced coagulation of nucleated clusters: The freshly nucleated clusters will coagulate within themselves and with larger (pre-existing) particles. The theory for charge-enhanced coagulation is well established and can be tested by CLOUD. The CLOUD results will be the first to observe directly the coagulation rates of charged nanometre aerosols.

6.1.2 Evaluation of atmospheric aerosol effects

Simulation of the CLOUD observations will enable a model including ion-mediated aerosol effects to be validated. The next element of the work is to apply this model to atmospheric conditions. While the experimental measurements will be performed under realistic temperatures, pressures and atmospheric concentrations of H_2SO_4 and H_2O, an

important missing element in the initial proposed programme is the influence of a larger background-aerosol mode. Such a mode in reality will scavenge condensable vapours and nucleated aerosols and suppress new particle formation. These effects may require experimental study by CLOUD. Using a model to scale the rates of new aerosol formation (determined by the beam intensity) to atmospheric conditions will be essential.

Idealised atmospheric box model simulations will be performed to study the influence of several quantities that affect the conversion of freshly nucleated particles into CCN (Fig. 16):

1. **H_2SO_4 concentrations.** The H_2SO_4 concentration is determined by production from oxidation of SO_2 by OH radicals and loss due to scavenging and aerosol nucleation. Realistic H_2SO_4 concentrations are therefore determined in a model simulation by specifying the background aerosol surface area and SO_2 and OH mixing ratios.

2. **Background aerosols.** A range of aerosol size distributions ranging between those typical of the free troposphere, the pristine marine boundary layer and polluted conditions will be used.

3. **Humidity and temperature** will be specified to be appropriate for the different atmospheric regions in item 2.

4. **Ion source strengths** vary between about 2 and 20 ion pairs/(cm^3s) between the boundary layer and the upper troposphere. Fluctuations in these source strengths at each altitude will be tested.

5. **Sensitivity to nucleation and coagulation rates** . These quantities, determined from the laboratory experiments, are likely to be uncertain and the effect of this on the calculations will need to be assessed.

Model simulations taking account of the full range of natural variations in the above quantities will be performed to establish whether variations in the cosmic ray flux are likely to have a significant effect on aerosol processes. In particular, we wish to establish whether there is an effect on aerosols in the CCN size range of about 100 nm, and which parts of the atmosphere are likely to be affected the most.

6.2 Modelling of cloud processes

The planned experiments in the cloud chamber will yield data that can be applied directly to numerical models of clouds. Two elements to a cloud modelling study based on these experiments can be identified:

1. Detailed simulation of the cloud chamber results to constrain microphysical parameters affected by ionisation.

2. Simulation of real clouds incorporating the effects identified in item 1.

The simulation of real clouds should take particular account of the relative effects of cosmic rays against a background of other natural variations.

6.2.1 Simulation of cloud chamber results

The cloud chamber experiments will enable the effect of ionisation on cloud droplet formation and freezing to be studied under well controlled conditions. It should be noted that the cloud formation processes in the chamber (principally droplet formation and freezing) are considerably simpler than the complex interacting processes that govern real cloud development (which include also coagulation, riming, sedimentation, droplet breakup etc). This relative simplicity will enable the cloud chamber observations to be compared with results of a highly simplified box model incorporating commonly used descriptions of droplet formation and freezing. Comparisons with and without beam should enable the effects of air ions to be identified and parameterised in the models.

6.2.2 Simulation of real clouds

The purpose of this element of the work is to determine whether the properties of natural clouds are sensitive to the effects of cosmic ionisation. There are *direct* effects and *indirect* effects that must be studied. The direct effects include charge-enhanced CCN activation into cloud droplets (Section 3.2.2) and ice nucleation (Section 3.2.4), while the indirect effect of interest is the charge-enhanced conversion of CN into CCN (Section 3.2.1).

In particular, we wish to examine the effect on the following cloud properties:

1. Cloud droplet number concentration (CDNC);
2. Precipitation formation in non-glaciating and glaciating clouds[19], which could influence cloud lifetime;
3. Cloud reflectivity and cloud emissivity.

There have been numerous studies of the factors affecting these cloud parameters. We anticipate that the contribution of small changes in the mean ionisation state of the atmosphere to the variance in these cloud properties will be small, though perhaps non-negligible. We also cannot exclude that a significant contribution to the variance could arise due to large amplitude fluctuations in ionisation rate.

We seek to understand whether ionisation variations are a *statistically significant* contributor to variations in these cloud properties. Our approach is to perform a Monte Carlo simulation using two detailed cloud microphysical models, one simulating marine stratus (the MISTRA model) and one simulating cumulus (described in the Appendix E). This requires running the cloud models a number of times with uncertain input parameters sampled at random from within appropriate ranges. Such a global stochastic approach also allows the synergistic effects between various input parameters to be determined. It is also the most appropriate technique for examining the significance of relatively minor variations in a parameter of interest. The models we propose to use are suitable for the calculation of these cloud properties but sufficiently simple to enable multiple calculations.

The important model variables to include in such a Monte Carlo simulation include, but are not restricted to, the following: Atmospheric thermodynamic state, which determines updraft velocities in clouds and entrainment rates and, in the case of stratus, the depth of the mixed layer; temperature and specific humidity; time of day, which affects

[19] *Glaciating* clouds are those in which ice formation occurs. Clouds in which this does not occur are often termed "warm clouds"

radiative imbalance and entrainment at the top of marine stratus. To test the effect of perturbations to the CCN abundance (Section 3.2.1) we will use the output of the aerosol models incorporating the charge-enhanced processes of nucleation, condensation and coagulation.

Several important questions need to be addressed at the single cloud level. The results of these detailed cloud resolving model studies could be parameterised for inclusion in atmospheric general circulation models to assess global changes.

1. What is the effect of aerosol changes on cloud droplet number densities and what effect does this have on cloud reflectivity (at solar wavelengths) and emissivity (in the infrared)? Can modelled changes in cloud optical properties be seen in satellite data? Cloud model studies will be needed using, as input, aerosol distributions calculated from off-line aerosol microphysical models.

2. How do changes in cloud droplet number affect the precipitation process in clouds? Changes in the efficiency of precipitation will influence cloud lifetime and, hence, on a statistical basis, average cloudiness. However, a direct relationship between changes in precipitation rate and cloudiness will be difficult to establish. The key point here is to establish the direction and approximate magnitude of any change.

3. How do changes in the efficiency of ice formation affect cloud thermodynamics (heat transport) and precipitation efficiency? Increased efficiency of ice formation in an individual cloud caused by a greater cosmic ray flux might be expected to lead to increased rainfall and decreased cloudiness, which would be opposite to the correlation that has been observed.

7 Accelerator and beam

In principle there are alternatives to a particle accelerator beam for providing a source of ionising radiation, such as UV or radioactive sources. However we consider that a particle accelerator beam has several advantages and is the best choice. Firstly a few-GeV hadron beam comprising protons and pions most closely duplicates the composition and energy of the cosmic rays and hadronic showers found in the upper atmosphere. The known timing of the beam pulse is also important for experiments such as ice nucleation where expansions are necessary at a precise time either before or after the beam exposure. A particle beam has the advantages that it is well collimated and easily traverses the material of the windows and gases of the cloud chamber and flow chamber, with negligible scattering. Finally, the beam intensity is easily adjusted over a broad range and can be measured precisely.

7.1 Experimental area

It is proposed to install CLOUD at the CERN PS (Proton Synchrotron) in the T11 secondary beamline of the East Hall. A preliminary study of the experimental installation has been carried out (Fig. 45). The cloud chamber itself would be permanently installed on the beamline for the duration of the experiment. However, to provide space for other

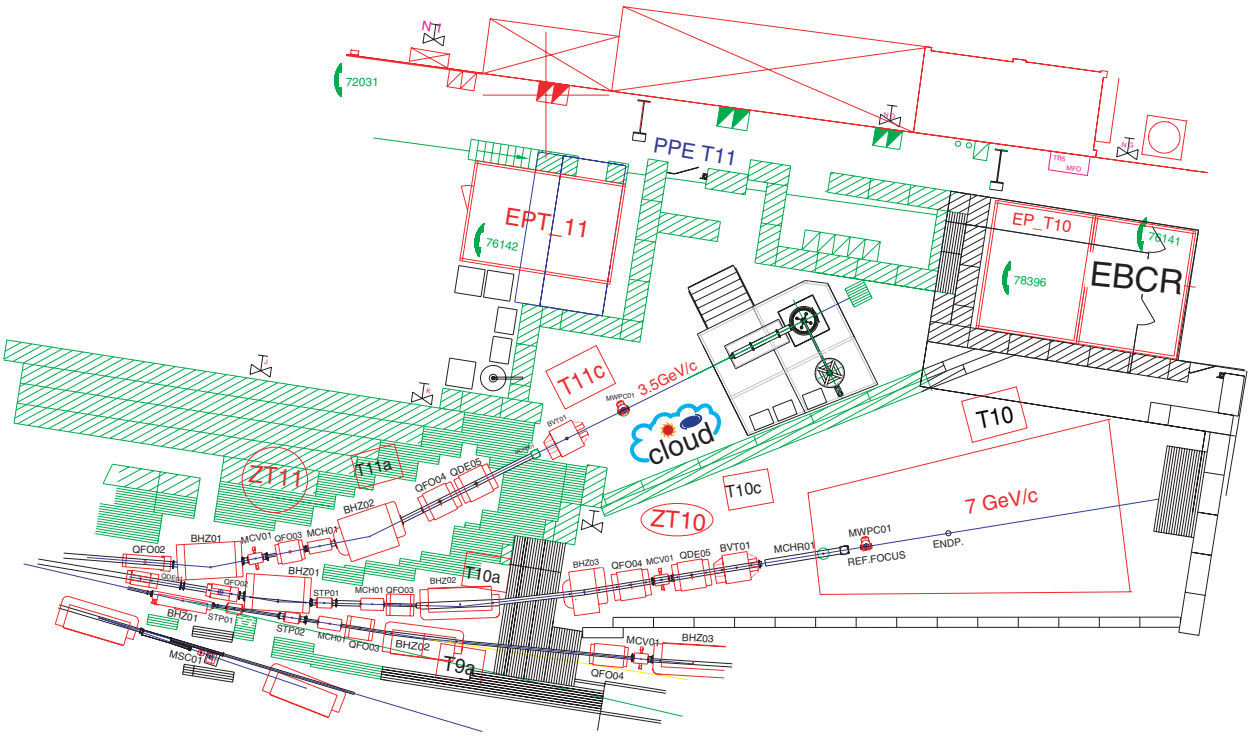

Figure 45: Experimental area layout of the CLOUD experiment at the CERN PS in the T11 beamline of the East Hall.

experiments to test detectors during periods when CLOUD is not running, we have designed the flow chamber to be dismountable from the beamline. The associated gas and aerosol generation and analysis systems, together with the liquid cooling and hydraulic systems, would be permanently installed near the apparatus. A dedicated counting room for CLOUD is foreseen to be installed above the current T11 counting room.

7.2 Beam requirements

The T11 beamline can deliver up to $\sim 10^6$ π/p per pulse (0.46 s duration). All lower intensities can be delivered. We assume one pulse would be available for CLOUD per supercycle (14.4 s). The T11 beam energy, which is selectable in the range ~1–3.5 GeV, matches the main part of cosmic ray spectrum . The transverse size of the beam at the detector (a minimum of about 7×7 mm^2 FWHM) is well-suited to the detector requirements.

We can compare the T11 beam with cosmic ray intensities in the upper troposphere as follows. One pulse of 10^6 π/p deposits $\sim 2 \cdot 10^7$ ion-pairs cm^{-3} in air at a pressure corresponding to 15 km altitude. At this altitude the molecular number concentration is about $5 \cdot 10^{18}$ cm^{-3}, so a single beam pulse deposits about 4 pptv ion-pairs (and also produces about 6 pptv NO and OH molecules). This beam flux is equivalent to about $5 \cdot 10^5$ s (5 days) of cosmic rays at 15 km altitude, and the initial ion-pair concentration is about a factor 10^4 higher than at 15 km altitude. The difference in these two factors is due to the ion lifetime in the atmosphere before recombination or scavenging, which is of order 100 s.

After beam passage, the ion concentration in the beam region will fall due to diffusion and to losses from ion-ion recombination and from scavenging by aerosols. The effects of diffusion and recombination have been simulated, as described in Section 5.4.3. The results show that the ion-pair concentration in the region around the beam about one minutes after a single pulse of 10^4 π/p is similar to the natural concentration at 15 km altitude (i.e. a few $\times 10^3$ i.p. cm^{-3}, see Fig. 50).

In summary, the T11 beam will allow a flexible exposure for CLOUD, with time-averaged ionisation cpncentrations ranging from below the natural level of cosmic rays (with the use of the clearing field) up to about a factor 100 times higher.

7.3 Beam counter system

The beam counter system (BCS) measures the particle beam intensity and its transverse profile. A telescope of plastic scintillation counters (T1, X1, Y1 and T2 in Fig. 26) measures the beam flux. The dimensions of the counters are approximately 60×60 mm^2 transversely and 8 mm thickness. A larger counter (H1) at the downstream end monitors the beam halo. The counters X1 and Y1 are beam hodoscopes to measure the beam profile in the horizontal and vertical projections, respectively. They are constructed from 4×4 mm^2 scintillator strips (or perhaps from scintillating fibres), read out with multi-anode phototubes, such as the Hamamatsu H6568/R5900-M16 with 4×4 photocathode pixels, each of size 4×4 mm^2. Scintillation counters will also be mounted above the cloud chamber to tag the presence of cosmic rays during data taking (not shown in the figure).

8 Planning

8.1 Cost estimates and responsibilities

Table 7 summarises the cost estimates for CLOUD and the proposed responsibilities of the collaborating partners. Following the standard CERN procedure, these financial responsibilities are to be considered as preliminary until they are agreed by the national funding agencies. When finalised they will be enacted by signing a memorandum of understanding between CERN and the collaborating institutes.

In addition to PS beam-time, the collaboration requests CERN provide the following:

1. Joint construction of the cloud chamber in collaboration with the Danish Space Research Institute (DSRI). This concerns:
   (a) Construction of subsystems for which CERN has special expertise, namely the piston and hydraulic system (which duplicates the BEBC design) and the liquid cooling system.
   (b) Engineering design support for the cloud chamber and associated equipment.
2. Technical coordination of the overall experiment.
3. Experimental research group (research staff and fellows).
4. Infrastructure support (offices, lab space, experimental counting room, computing support, etc.).

Table 7: Cost estimates and proposed responsibilities.

Item	**Cost [kCHF]**	**Responsible Institutes**
Cloud chamber & flow chambers:		
Mechanical assembly & field cage	150	DSRI-Copenhagen
Piston & hydraulic system	95	CERN
Liquid cooling system	75	CERN
Optical readout:		
CAMS detector & laser†	200	Vienna
CCD camera system & Xenon flasher	75	RAL
Gas & aerosol generation systems:		
Gas & aerosol systems	50	Helsinki, FMI, Kuopio
Water vapour system	20	UM-Rolla
Physical, chemical and ion analysis:		
Aerosol physical analysers	100	Helsinki, FMI, Kuopio, UM-Rolla
Linear quadrupole mass spectrometers	1100	MPIK-Heidelberg
ToF mass spectrometer	175	Aarhus, Ioffe
Ion mobility detector	75	Reading
Beam measurement:		
Beam counter system	30	Lebedev
DAQ & computing:		
DAQ & slow control system	65	-
Atmospheric cloud simulations	50	Leeds, Mainz
Infrastructure:		
Support structure & counting room	40	CERN
Total:	**2300**	

† Does not include contract manpower, estimated at 240 kCHF.

Table 8: Construction milestones.

Date	**Activity**
Dec 2000	Finish detailed design & prototyping
Jan 2001	Start construction
Nov 2001	Begin installation at CERN PS
Mar 2002	Checkout with beam
May 2002	Start data taking

The present estimate of the total construction cost is 2300 kCHF (Table 7), assuming an efficient use of existing equipment and the recuperation of some materials and infrastructure equipment from previous, terminated experiments. These estimates are based on delivered value on-site and do not include the technical infrastructure used in the home institutes. Neither do the above estimates include manpower costs since they are accounted for in the home laboratory infrastructure costs. Discussions are proceeding with the national funding agencies in order to secure adequate home laboratory infrastructure support for the experiment.

Plans are underway to apply for complementary funding from the European Union for equipment support as well as to fund a number of Ph.D. students and research assistants to participate in the experiment.

The annual maintenance and operation costs of CLOUD are estimated at 100 kCHF. These cost would be paid by the collaborating institutes, including CERN, following the standard CERN procedure. Since the total power consumption of the experiment is under 60 kW, the electricity costs are negligible.

8.2 Technical coordination

Technical coordination covers the following tasks:

- Establishment of a master schedule linked to each institute's own schedule, and monitoring of the progress.
- Management of all interfaces between the various components, and resolution of any technical inconsistencies.
- Management of the engineering data.

Concerning the last item, all relevant documents (technical specifications, engineering and calculation notes, documents from manufacturers, etc.) would be organised within the framework of the CERN EDMS (Engineering Data Management System). In particular, the CDD (CERN Drawings Directory) software will be used to provide a central library of all relevant drawings produced by the institutes or manufacturers. Once stored and archived in the CDD, the drawings are available to all registered collaborators through a web interface. The documents can be retrieved via the web and viewed under HPGL (Hewlett Packard Graphical Language) format, which is the equivalent of Postscript for technical drawings. Evolution of the detector design and the release of new technical drawings can then be efficiently managed in a controlled and readily-accessible manner.

8.3 Milestones

Assuming the SPSC recommends approval of the experiment in May 2000, the detailed design and prototyping will be finished by the end of 2000 and the construction will take place in 2001. The initial checkout of the equipment with beam is expected to start in March 2002. A preliminary estimate of the time required to complete the data taking is about 3 years, but at present this should be considered as approximate.

9 Conclusion

We have joined together in an unprecedented team of atmospheric physicists, solar-terrestrial physicists and particle physicists, to offer CERN the opportunity to make a major contribution to environmental science. Clouds are the engines of the weather, yet they are only sketchily understood at the microphysical level. Now satellite observations give empirical evidence for an astonishing link between high-energy physics and meteorology, namely that cosmic rays from the Galaxy may influence cloud formation and behaviour.

If this link between cosmic rays and clouds is real, it provides a major mechanism for climate change. During the 20th Century the cosmic rays reaching the Earth diminished by about 15% as a result of increasing vigour in the solar wind, which scatters the cosmic rays. The inferred reduction in cloud cover could have warmed the Earth by a large fraction of the amount currently estimated to be due to man-made carbon dioxide. In that case, the effect of carbon dioxide may have been overestimated. If, on the other hand, the link to cosmic rays proves to be illusory, present diplomatic efforts to curb emissions of carbon dioxide will be more strongly supported scientifically. Settling the issue, one way or the other, is therefore an urgent task.

To find out whether cosmic rays can affect cloud formation, and if so how, we propose to simulate the cosmic rays with a beam of charged particles from CERN's Proton Synchrotron, in the CLOUD experiment. The beam will pass through a cloud chamber where the atmosphere is to be represented realistically by moist air charged with condensation nuclei and trace condensable vapours, and chilled by expansion. We shall be able to compare processes when the beam is present and when it is not.

Our team brings to the planning of the CLOUD experiment a thorough knowledge of atmospheric and cloud science, derived from field and laboratory experiments, airborne data-gathering, satellite observations, and microphysical theories. We also possess considerable experience with cloud chambers and their optical readout, and with the mass spectrometers and aerosol particle detectors required for chemical and physical analyses of aerosols and ions. The design of the cloud chamber draws on CERN's own experience, notably with the Big European Bubble Chamber.

Space research has shown how "big science" can make spectacular contributions to knowledge of the environment by bringing together experts from different disciplines. As an analogous multidisciplinary team for particle physics, we do not claim total originality. More than 100 years ago C.T.R. Wilson invented the cloud chamber to investigate weather phenomena. It evolved into a prime instrument for particle physics. Now the wheel of history turns and we go back to Wilson's concept to investigate the possibility that the Earth's atmosphere acts like one big cloud chamber that echoes the whims of the Sun.

Acknowledgements

We would like to warmly thank for their advice and important contributions to this proposal, Jürg Beer, J.J. Blaising, Nigel Calder, Luc Durieu, Gregory Hallewell, Alain Hervé, Markus Nordberg, Michael Price, David Ritson, Jean-Pierre Riunaud, Thomas Ruf, Tom Taylor, Johann Tischhauser, Robert Veenhof and Alan Watson.

APPENDICES

In the following we provide some general background information on: cloud physics (Appendix A), aerosol-cloud-climate interactions (Appendix B), classical operation of a Wilson cloud chamber (Appendix C), cosmic rays in the atmosphere (Appendix D), and cloud models (Appendix E).

A Cloud physics

A.1 General properties of clouds

Clouds are principally composed of ice and water, and in some cases they may contain electrified particles. High and low altitude clouds of limited vertical extent may contain only one principal phase of liquid water or ice; for example, cirrus clouds in the upper troposphere (altitudes greater than about 8 km) are composed principally of ice. Clouds are often classified as stratiform or convective. The bulk properties of clouds have a marked influence on climate, although whether clouds cause a net warming or cooling of the atmosphere depends on the cloud properties and altitude.

Water vapour is effectively a gaseous constituent of atmospheric air, and its concentration can be determined by its gaseous partial pressure. At any given temperature there is an associated maximum value of partial pressure due to water vapour, the *saturation vapour pressure*. Air containing sufficient water vapour to generate the saturation vapour pressure is said to be saturated, and has a relative humidity of 100%. Most natural clouds form when air becomes saturated upon cooling, either adiabatically (cooling upon expansion of rising air) or isobarically (e.g. by radiatively cooling near the ground, producing fog). Occasionally it is possible for the saturation vapour pressure to be exceeded in localised regions, known as *supersaturation* (SS). In the atmosphere, this is never greater than an excess relative humidity of few percent, due to the abundance of small particles (or aerosol) on which the water can condense. Many different kinds of aerosol are capable of acting as *condensation nuclei* (CN) but it is the subset able to permit condensation (activation) at atmospheric SS (*cloud condensation nuclei*, CCN) which are of greatest interest for the formation of atmospheric clouds.

If the temperature is below 0°C, liquid water droplets may persist in a thermodynamically unstable *supercooled* state from which freezing may be readily initiated. Freezing can be initiated by heterogeneous or homogeneous nucleation. In *heterogeneous nucleation*, the supercooled water freezes in the presence of a suitable ice nucleus. *Homogeneous nucleation* occurs if cooling is continued further, and all supercooled water in atmospheric clouds becomes ice at about -40°C by this process. Suitable ice nuclei are very rare in the atmosphere, and it is certainly the case that only a very small (but variable) fraction of the atmospheric aerosol is able to initiate ice. Consequently a significant fraction of atmospheric clouds contain supercooled water. At temperatures between about -5 and -10°C, ice multiplication processes can occur. When a particle freezes at these temperatures, mechanical stresses during freezing lead to the ejection of small ice fragments, which in turn act as efficient ice nuclei.

The *droplet number density* in water clouds depends upon the cooling rate of air as

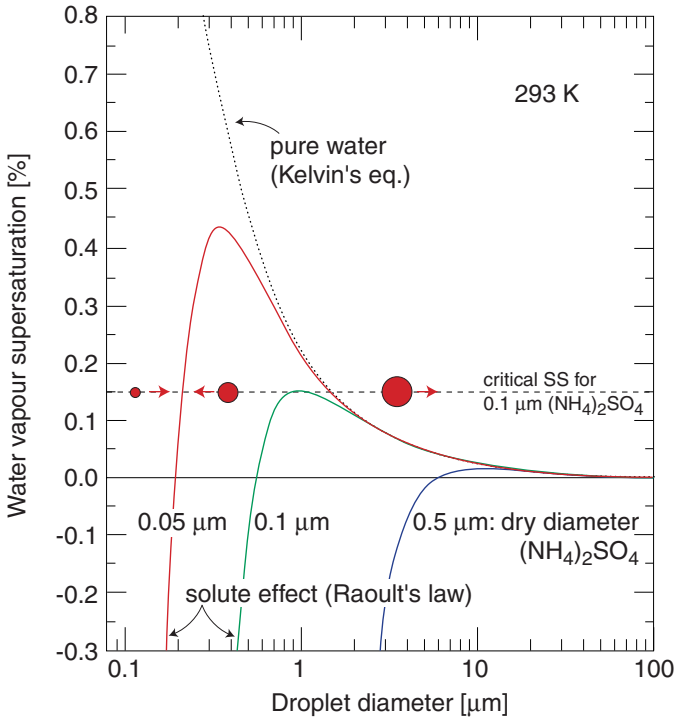

Figure 46: Köhler curves showing the equilibrium water vapour supersaturation at 293 K for droplets of pure water (dotted curve) and for droplets containing various masses of dissolved $(NH_4)_2SO_4$ (solid curves) vs. diameter of the droplet [129]. The water vapour supersaturation, $SS\ (\%) = (p/p_0 - 1)\cdot 100$, where p is the partial pressure of the water vapour and p_0 is the saturated vapour pressure over a plane surface of water at this temperature. In the indicated example, an ambient water vapour SS of 0.15% (dashed line) exceeds the critical value for all ammonium sulphate aerosols with dry diameter ≥ 0.1 μm. These aerosols will therefore activate and grow into cloud droplets, whereas smaller aerosols remain as unactivated haze particles. Droplets below their corresponding equilibrium curve will shrink by evaporation whereas those above will grow by condensation (the indicated droplets correspond, for example, to a dry diameter of 0.05 μm).

it enters the cloud (since this affects the peak SS that is reached) and upon the concentration, size and chemical composition of the CCN. Although highly variable, typical number densities are a few $\times$ 100 cm^{-3} in continental clouds and a few $\times$ 1–10 cm^{-3} for maritime clouds. Number densities are usually higher in convective clouds than in stratiform clouds.

Activation of a CCN occurs when the water vapour SS exceeds a critical value. This can be seen from the Köhler curves (Fig. 46), which show the equilibrium SS (and therefore equilibrium vapour pressure) over droplets of various sizes and containing various masses of dissolved salts. The equilibrium SS of pure water droplets increases with decreasing radius due to the effect of curvature (Kelvin's equation; $\ln(p/p_0) \propto 1/r$). However dissolved salts reduce the equilibrium SS due to a reduction of the molar concentration of the water (Raoult's law; $p/p_0 \propto -1/r^3$). The latter effect dominates at small radii, i.e. at high solute concentrations.

Once activated, droplets grow by diffusion of water vapour. *Diffusional growth* is rather

slow and it is unusual for droplet radii to exceed 20–30 μm by this process. Cloud droplets typically attain sizes of 10 μm within a few minutes but take over an hour to reach 100 μm (the growth time $\propto r^2/SS$). Droplet *collision and coalescence* (which occurs when droplets collide while falling under the influence of gravity) takes over as the principal growth mechanism for radii greater than about 20 μm.

For clouds to generate *rainfall*, some drops must grow to precipitable sizes of 1 mm or greater. This is achieved not by diffusional growth of water droplets, but by collision and coalescence of droplets or formation of ice (*glaciation*). Ice formation usually occurs in only a small fraction of the cloud droplets, allowing these to grow by vapour diffusion preferentially due to the lower vapour pressure of ice crystals compared with water droplets. The ability of a cloud to generate rain is an important factor in determining its lifetime.

Clouds have a high *reflectivity* at visible wavelengths and contribute significantly to the net *albedo* of the planet, reducing the net amount of radiation that is absorbed at the Earth's surface. Any changes in cloud reflectivity would therefore have potential implications for the radiative balance of the climate system. Cloud reflectivity depends on the mass of condensed water (termed the *liquid water content*), the depth of the cloud and the droplet number density. Figure 47 shows the variation of cloud reflectivity with cloud depth and cloud droplet number density for a fixed liquid water content of 0.3 g m^{-3} (most data confirm that there is little or no dependence of liquid water content on cloud droplet number density). Any perturbation of cloud droplet number density by cosmic rays could lead to changes in cloud reflectivity.

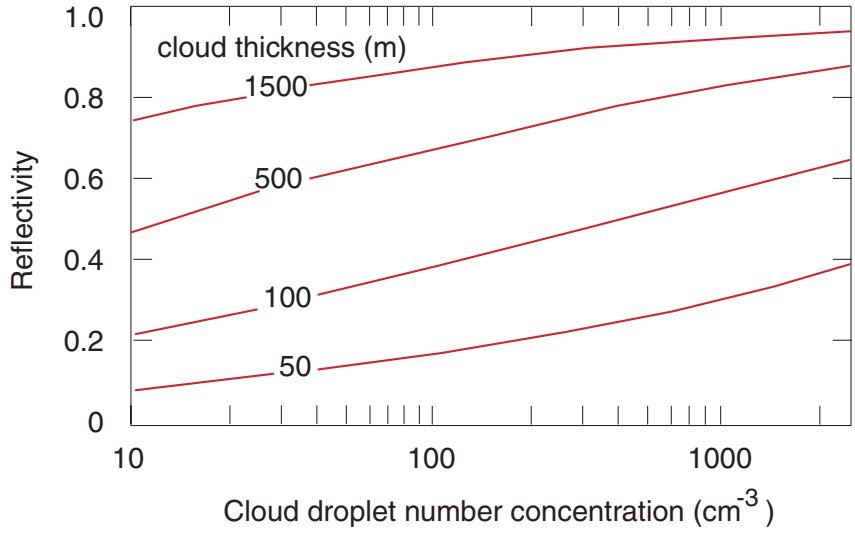

Figure 47: The variation of cloud albedo with cloud thickness and droplet number concentration for a fixed liquid water content of 0.3 g m^{-3} [130].

A.2 Aerosols and cloud condensation nuclei

Atmospheric aerosols are liquid or solid particles or clusters of molecules suspended in the air. The atmosphere contains significant concentrations of aerosols, sometimes as high as

10^6 cm^{-3}, with diameters spanning over four orders of magnitude from a few nm to a 100 μm or so. Aerosols are often classified as either *primary* or *secondary*. Primary particles are those injected directly into the air (e.g. by wind erosion, sea spray, pollen, etc). These may be either of natural or anthropogenic origin. Secondary aerosols are those created by gas-to-particle conversion of molecules (*nucleation*).

Aerosol composition varies widely depending upon geographical location and proximity to specific sources. It also varies significantly across the size distribution, with the smallest aerosols often being clusters of volatile species such as sulphuric acid and water (formed from gas-to-particle conversion) and the largest often being inorganic salts and dust particles. Although it is not possible to define a canonical aerosol distribution, observations indicate that aerosol sizes can often be described by quasi-distinct modes. For example, a typical remote continental aerosol (Fig. 48) is composed of a *nucleation* mode (median radius $\simeq 0.01$ μm), an *accumulation* mode (median radius $\simeq 0.1$ μm) and a *coarse* mode (median radius $\simeq 10$ μm).

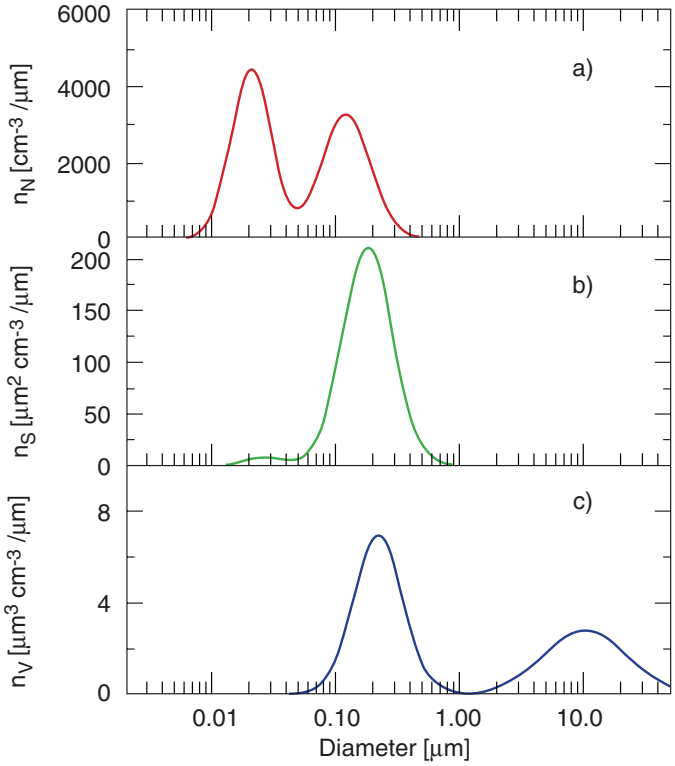

Figure 48: Typical remote continental aerosol distributions: a) number, b) surface area and c) volume [129].

The size and composition distribution are determined by many different processes. They include the following: nucleation of new particles at small sizes, formation of larger primary particles, coagulation, deposition, condensation of soluble gases, phases changes (e.g. crystallisation), in-cloud transformations and washout, and water uptake. Inorganic aerosols are usually weakly acidic, with the most common aqueous cationic components being H^+, ammonium (NH_4^+) and sodium, and with anionic components sulphate, chloride, nitrate. Such aerosols are hygroscopic. Aerosols can also be partly or wholly com-

posed of organic compounds derived from plant waxes and combustion sources. These aerosols may be either hygrophobic or hygroscopic.

Nucleation of new aerosols is an important way in which anthropogenic emissions can perturb the properties of aerosols. An important source of new aerosols is the oxidation of sulphur dioxide in the presence of water vapour to give sulphuric acid, which readily combines with water vapour to form new aerosols. This is believed to be primarily a *homogeneous* nucleation process, although atmospheric ions from cosmic rays may affect the rate of formation of new aerosols. The rate of nucleation is extremely difficult to predict from theory and must be measured in the laboratory under well-controlled conditions.

Hygroscopic aerosols serve as centres for the growth of cloud droplets. Such *cloud condensation nuclei (CCN)* are normally aqueous acids or dissolved salts. Not all aerosols grow into cloud droplets. The number that do depends on their composition, the SS attained in the cloud, and the size distribution of aerosols competing for moisture. An increased aerosol number density in general leads to an increased cloud droplet number density.

A.3 Atmospheric electricity

Electric fields present in the atmosphere vary between fair weather values of typically 100 Vm^{-1} at the surface to about 100 kVm^{-1} in thunderstorms before a lightning discharge. The atmospheric electric circuit, which involves a global current of 2000 A, is thought to be sustained by thunderstorms continually active around the tropics. This current between the ionosphere and the Earth's surface flows throughout the atmosphere, in regions of disturbed and undisturbed weather, and is carried by vertical migration of molecular ions.

The molecular ions (more traditionally known as small ions) are formed continuously in the atmosphere by galactic cosmic rays (see Appendix D.1) and, close to the land surface, also by natural radioactivity. The ions produced are rarely single species but clusters of water molecules around a central ion. Typical atmospheric ion concentrations at low altitudes in unpolluted air and fine weather are about 500 ions cm^{-3}, and vertical charge fluxes caused by conduction in fair weather conditions are typically 2 pA m^{-2} ($\sim$12 ions $\mathrm{cm}^{-2}\mathrm{s}^{-1}$). Ions are removed by self-recombination and by attachment to atmospheric aerosols. Ion concentrations are generally lower in clouds than in clear air conditions due to scavenging by droplets. Chemical differences between positive and negative ions leads to a natural asymmetry in which the negative ions have a slightly higher (20%) electrical mobility: this asymmetry leads to a small average charge on atmospheric particles.

Electrification in disturbed weather (thunderstorms) is not completely understood but is thought to result from ice-water interactions in thunderclouds, in which vertical convective motions lead to differential transport of rising ice crystals and falling soft hail. Their interaction leads to electrification, the sign and magnitude of charge exchange depending on the temperature at which they interact which, in turn, is a function of height. It has also been suggested that negatively-charged aerosols have faster activation and growth than positive aerosols and that this may contribute to the charge-separation mechanism in thunderclouds.

B Aerosol-cloud-climate interactions

The increased concentration of greenhouse gases such as water vapour, carbon dioxide and methane may have large effects on the Earth's climate by enhancing the greenhouse effect. Much attention has also been paid to the possibility that the increased concentrations of aerosol particles can have a cooling effect on the global climate [131, 132, 133].

Clouds can affect on electromagnetic radiation fluxes in the Earth's atmosphere by scattering and absorption. Locally the net effect is not very evident (e.g. because of different kinds of surfaces) [134]. According to measurements, however, the global net effect of today's clouds on the climate is probably cooling [135] and thus opposite to the effect of greenhouse gases. The effects of clouds on the radiation fluxes depend on their depth, liquid water content and cloud droplet size distribution [136] (Appendix A.1).

The formation and growth of cloud droplets occur on pre-existing aerosol particles. The characteristics of the pre-existing particle distribution strongly affect the developing cloud droplet distribution. Field experiments show that the pre-existing aerosol particle distribution is usually composed of mixed particles, i.e. particles including both hygroscopic and insoluble components [137, 138, 139]. According to recent model studies by the Helsinki group [140, 141], the soluble mass of pre-existing aerosol particles is the most important factor (other than dynamics) in determining the developing cloud droplet distribution. Hygroscopic material decreases the saturation vapour pressure of water vapour above the surface of a solution droplet and makes the formation of a cloud droplet easier. The condensation of different gaseous substances on the aqueous particles during their growth increases the hygroscopicity of the particles. When the amount of the hygroscopic material in the particles increases it also decreases the critical supersaturation needed for their activation to cloud droplets [121, 142] (see Fig. 46). It has been recently shown that thin organic films can also affect the water vapour pressure above the growing droplet's surface and thus influence cloud droplet formation [143].

The amount of water vapour available during the growth process depends on various dynamical aspects and on the particle size distribution. When an air parcel exceeds 100% relative humidity the most hygroscopic particles activate first and start to consume water vapour. The maximum supersaturation achieved is therefore smaller when there is a larger amount of soluble material in the nascent aerosols. Condensation of some strongly hygroscopic gaseous substances on the particles simultaneously with water vapour can allow a larger fraction of the pre-existing particle distribution to grow to cloud droplets.

Recently we have investigated the effects of changing hygroscopicity (the availability of condensable material in the gas phase) on the formation of cloud droplets [144, 145]. In the simulation, water (H_2O), nitric acid (HNO_3), hydrochloric acid (HCl) and ammonia (NH_3) vapours condense on mixed particles composed of ammonium sulphate ($(NH_4)_2SO_4$) and an insoluble substance. In order to take into account the dynamical aspects, we used an adiabatic air parcel model [121]. The initial mean radii, standard deviations and number concentrations as well as the fraction of soluble salt in the particles and the concentration of gaseous HNO_3, HCl and NH_3 in ambient air are varied about their observed values in marine and continental air (Table 9). The Helsinki group has also investigated how the optical thickness of the simulated clouds varies as a function of initial ratio of acid and ammonia mixing ratios.

Our simulations confirm that gas phase hygroscopicity has a large effect on the forma-

Table 9: Measured ranges of gaseous ammonia, nitric acid and hydrochloric acid concentrations in marine and continental air.

Trace gas	**Marine** [ppb]	**Continental (rural or semi-rural)** [ppb]	**Continental (polluted)** [ppb]
NH_3	0.1- 14	0.2 - 5.4	7 - 100
HNO_3	0.05 - 0.8	0.2 - 1.8	4 - 8
HCl	$<$ 0.1 - 1.0	0.08 - 1.4	1 - 23

tion and properties of clouds [144, 145]. The Köhler curves are also modified [146, 147]. In general, this study shows that the increase in hygroscopicity of growing droplets implies an increasing number of cloud droplets and increasing optical thickness of a cloud. The way in which the soluble mass is distributed among aerosol particles and between the size modes also seems to be important [148]. When condensed on aqueous solution droplets, nitric and hydrochloric acids enhance the activation of cloud droplets. This is also the case when no other condensable trace gases present. In contrast, ammonia alone cannot enhance the number of activated cloud droplets significantly. But in real atmospheric situations where particles also take up strong acids, ammonia has a clear increasing influence on the activation of cloud droplets. This is due to the fact that larger amounts of free hydrogen ions enhance the formation of ammonium ions significantly. On the other hand condensed ammonia neutralises the solution droplets efficiently, which allows larger amounts of condensable acids to be taken up.

We have also studied how the optical properties of the resulting cloud droplet distribution vary with changing hygroscopicity. The change of optical thickness is usually very large (the maximum $\Delta\tau/\tau$ is 1.6, where τ is the optical thickness). This is the case even at moderate concentrations, for example $\Delta\tau/\tau$ is around 0.5 when the sum of acids is 1 ppbv and ammonia is 1 ppbv. This change in optical thickness means that the albedo of an individual cloud may change significantly. In summary, therefore, it is important to estimate the global indirect forcing due to the effect of condensable gases on cloud droplet formation, and to understand the possible influence of galactic cosmic rays on this process.

C Classical operation of a Wilson cloud chamber

The principle of classical operation of a Wilson cloud chamber [70, 149] for the detection of charged particles can be understood from Fig. 49 which shows the water vapour pressure equilibrium curves for small droplets carrying a charge Qe:

$$\log_e\left(\frac{p}{p_0}\right) = \frac{M}{RT\rho}\left[\frac{2\gamma}{r} - \left(\frac{Q^2e^2}{4\pi\epsilon_0 r^2}\cdot\frac{1}{8\pi r^2}\right)\right],$$

where p is the vapour pressure, p_0 the saturated vapour pressure at a plane water surface, R the gas constant, T the absolute temperature, γ the surface tension, M the molecular

weight, ρ the density, ϵ_0 the permittivity of free space and r the radius of the droplet. The curves divide an upper region of vapour pressure in which water droplets grow by condensation (e.g. droplet D_1 in Fig. 49) from a lower region where they shrink by evaporation (e.g. D_2).

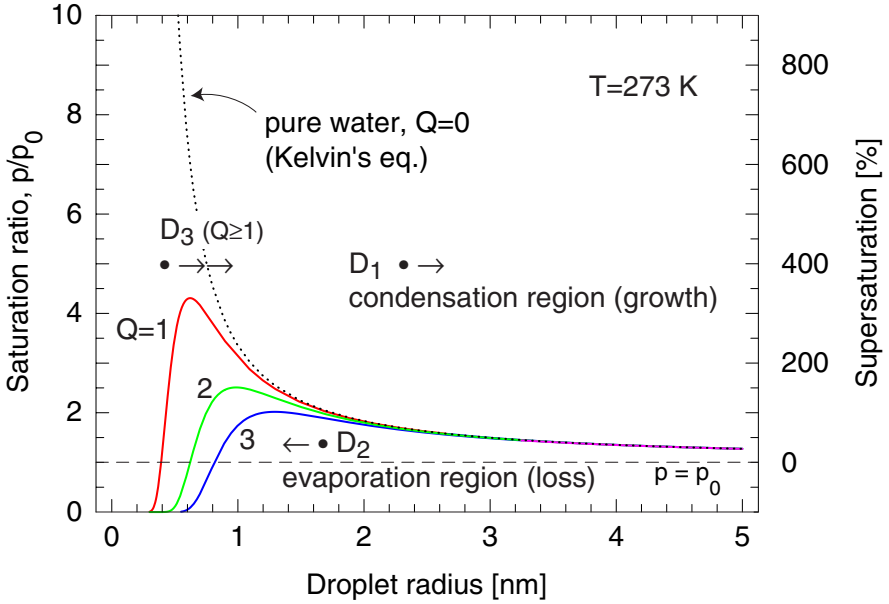

Figure 49: Thomson-Kelvin curves showing the equilibrium saturation ratio for charged droplets of pure water at 273 K. The curves are labelled according to the droplet electronic charge, Qe. The saturated vapour pressure, p_0, corresponds to equilibrium with a plane water surface (0% supersaturation). Droplets formed in the region above the curves will grow (condensation region) while those below will shrink (evaporation region).

The curves are similar in shape to the Köhler curves for the equilibrium vapour pressure over aerosol-nucleated droplets, but much higher supersaturations are required for activation of charged droplets of pure water (compare Fig. 46 with the right-hand scale of Fig. 49). The (purely electrostatic) influence of droplet charge is significant only for very small radii ∼1 nm. To set this scale, the effective radius of one water molecule is ∼0.2 nm and a droplet of radius 0.5 nm contains about 18 molecules. The charge reduces the equilibrium water vapour pressure by an increased attraction of the polar water molecules. Evidence suggests that negative ions form larger condensation nuclei than do positive ions, and hence the former activate more rapidly and at lower water vapour supersaturations.

The necessary supersaturation in a cloud chamber is generated by fast adiabatic expansion. For an ideal gas and an adiabatic expansion,

$$\begin{aligned} P_1 V_1^{\gamma} &= P_2 V_2^{\gamma}, \quad \text{and} \\ T_1 V_1^{\gamma-1} &= T_2 V_2^{\gamma-1}, \end{aligned}$$

where γ is the ratio of specific heats C_P/C_V (1.40 for air and saturated water vapour). For example, when a mixture of air and saturated water vapour at 1 atmosphere and 293 K is adiabatically expanded by a large volume ratio $V_2/V_1 = 1.3$, the temperature

falls to 264 K and the resultant saturation ratio is 5.9 (i.e. 490% supersaturation). Under these conditions all small ions ($Q \geq 1$) are activated and rapidly grow to visible droplets.

In contrast, very small adiabatic expansions are required to generate the low supersaturations of a few $\times$ 0.1% found in the atmosphere (Fig. 46). For example, a 100 μm piston movement of the CLOUD expansion chamber at one atmosphere and 293 K gives a volume expansion ratio $dV/V = 2.0 \cdot 10^{-4}$ and a pressure expansion ratio $dP/P = 2.8 \cdot 10^{-4}$. This reduces the gas temperature by 0.023 K and produces a supersaturation of 0.12%. These considerations set the required temperature stability of 0.01 K for the CLOUD expansion chamber.

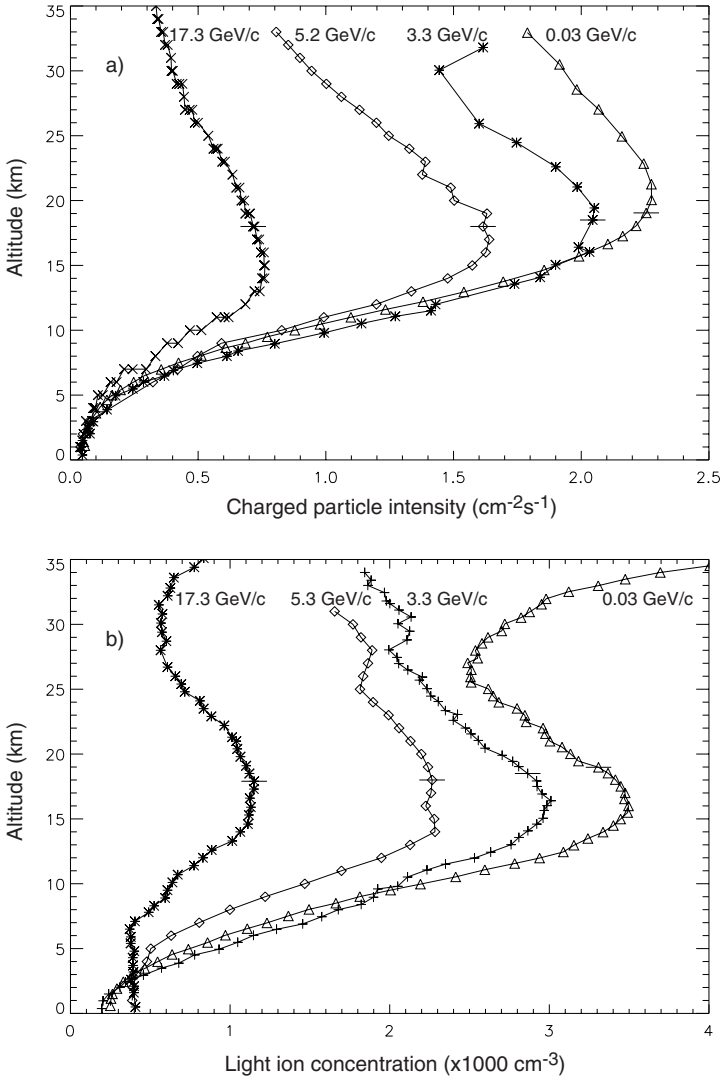

Figure 50: a) The charged particle intensity and b) the light ion concentration vs. altitude, measured at several latitudes with cutoff rigidities as indicated [150]. The intensity measurements in a) were made with the omnidirectional Geiger counter described in Appendix D.2. In b) the five-point running averages are shown. The data were recorded in or near 1990, corresponding to a sunspot maximum (but without solar proton events), i.e during a cosmic ray *minimum*. The horizontal bars show the typical experimental statistical errors.

D Cosmic rays in the atmosphere

D.1 General characteristics of atmospheric ions

The maximum cosmic ray fluxes occur at altitudes of 15–20 km, where the charged particle intensities vary between about 0.8 and 2.3 $cm^{-2}s^{-1}$, depending on geomagnetic latitude (Fig. 50a) [150]. In air at 101 kPa pressure (1.22×10^{-3} gm cm^{-3}), the mean ionisation density for minimum-ionising charged particles is 68 ion-pairs cm^{-1}. At high altitudes the fraction of heavily-ionising non-relativistic particles becomes significant and the mean ionisation density is about 110 ion-pairs cm^{-1}, corrected to 1 atmosphere pressure [150]. At 15 km the density of air is 0.20×10^{-3} gm cm^{-3} and the mean ionisation density is therefore about 18 ion-pairs cm^{-1} per charged particle. Therefore the ion-pair production rate by cosmic rays at 15 km altitude is $q = 18\times$ (0.8–2.3) = (14–41) $cm^{-3}s^{-1}$, depending on geomagnetic latitude. Free radicals are also created by galactic cosmic rays and these may lead to chemically-reactive molecules. As examples, about 1–2 OH radicals [53] and 1.5 NO molecules [55, 56, 57] are estimated to be produced per ion-pair. Mixing ratios of about 0.7 pptv OH or NO are therefore generated by cosmic rays per day in the upper troposphere.

Once created, the charged particles will interact with atmospheric gas molecules and thereby become converted to complex positive and negative cluster ions [151]. Free electrons will rapidly ($\tau \sim 200$ ns) attach to O_2, leading to O_2^- as the most important primary negative ion. Primary positive ions are mostly N_2^+, O_2^+, N^+, and O^+. Both positive and negative primary ions experience rapid ion-molecule reactions with relatively abundant atmospheric gases leading to the cluster ions $H^+(H_2O)_n$ and $CO_3^-(H_2O)_n$. The former react further with basic molecules B possessing proton affinities larger than that of H_2O leading to $H^+B(H_2O)_n$. An important example for B is acetone $(CH_3)_2CO$ (proton affinity: 194 kcal/mol). Negative ions react with acidic molecules, particularly HNO_3 and H_2SO_4, leading to $NO_3^-(HNO_3)_m$ and $HSO_4^-(H_2SO_4)_l(HNO_3)_k$. The above species have been observed in the upper troposphere and lower stratosphere by aircraft-based ion mass spectrometers [152, 62].

The variation of ion concentration with time is given by

$$\frac{dn}{dt} = q - \alpha n^2 - \beta n N_a - \gamma n^p \tag{7}$$

where q [$cm^{-3}s^{-1}$] is the ion-pair production rate by cosmic rays, $n = n_+ = n_-$ [cm^{-3}] are the positive and negative small ion concentrations, α [cm^3s^{-1}] is the ion-ion recombination coefficient (about 1.5×10^{-6} cm^3s^{-1}), β [cm^3s^{-1}] is the ion-aerosol attachment coefficient (which varies with aerosol size and charge) and N_a [cm^{-3}] is the aerosol number concentration. The final term represents the unknown contribution of ion induced nucleation; γ is the ion induced nucleation coefficient, and the power p may lie between 1 and 2, depending on the mechanism. If we assume for the moment that the principal removal mechanism is ion-ion recombination, then equilibrium is reached when the ion-pair production and recombination rates are equal, i.e. when $q = \alpha n^2$. This implies an equilibrium ion-pair density, $n = \sqrt{q/\alpha} = \sqrt{(14-41)/(1.5 \times 10^{-6})} = (3.1 - 5.2) \times 10^3$ cm^{-3}. Therefore the total light ion concentration (both + and -) is about $(6 - 10) \times 10^3$ cm^{-3}. The measured light ion concentrations (Fig. 50b) are between a factor 3–5 smaller than this estimate,

indicating extra losses due to ion-scavenging by aerosols and perhaps also to ion-induced nucleation.

Figure 50b) shows that the maximum light ion concentration occurs at an altitude of about 17 km, and the concentration at 8–9 km is about a factor of two lower. Since the troposphere has a depth of about 18 km over the tropics, decreasing to about 8 km over the poles, this indicates that between one third and one half of the total ionisation from galactic cosmic rays is deposited directly in the troposphere, depending on latitude.

From Eq. 7, the recombination lifetime of an ion is $\tau \simeq 1/(\alpha n)$. This implies ion lifetimes of about 3–9 min. Additional loss mechanisms, such as aerosol attachment, will reduce the actual lifetime. The ions drift vertically in the electric field created by the negatively-charged Earth and the positively-charged ionosphere. The field strength is $E \sim 100$ V/m at sea level, producing an drift velocity for small ions of about 1.5 cm s^{-1}. At an altitude of 15 km, however, $E \sim 2$ V/m due to the higher conductivity of the air, and the drift velocity is only 0.1 cm s^{-1} This results in an ion drift distance at 15 km altitude of only 0.4–1.0 m before recombination. The ions and free radicals produced by cosmic radiation will in general be transported substantially further by tropospheric dynamics, both vertically and horizontally.

D.2 Atmospheric measurements of cosmic rays

We present here a summary of the regular balloon cosmic ray (CR) observations started by Lebedev Physical Institute in the former Soviet Union in 1957. The cosmic ray monitoring in the atmosphere consists of the launching of small rubber balloons, each carrying a special radiosonde and a charged particle detector [153, 154].

The charged particle detector comprises two cylindrical Geiger counters, each of 9.8 cm length and 1.8 cm diameter, and with steel walls of 0.05 g cm^{-2} thickness. The counters are arranged in a vertical telescope with their axes separated by 2.7 cm and a 7 mm (2 g cm^{-2}) Al filter inserted between them. A single counter provides the omnidirectional flux of charged particles: electrons with energy $E_e > 0.2$ MeV and protons with $E_p > 5$ MeV. A coincidence of the two counters records the vertical flux of charged particles within a solid angle of about 1 sr: electrons with $E_e > 5$ MeV and protons with $E_p > 30$ MeV. Both the omnidirectional and vertical fluxes of charged particles in the atmosphere are measured simultaneously. A radio pulse caused by a charged particle passing through one or both counters is transmitted to a ground-level receiver. In addition, the air pressure (atmospheric depth) is measured by a special barometric sensor. In this way the charged particle counting rates versus atmospheric depth are recorded. Measurements are made continuously from ground level up to altitudes of 30–35 km.

The monitoring stations for the long-term cosmic ray study are summarised in Table 10. Balloon launches are made almost every day at these sites, and have been continuously for about 40 years. Despite the difference in their geomagnetic cutoff rigidities, R_c, the measured intensities at Mirny and Murmansk are essentially equal to each other because of the atmospheric material cutoff, which is higher than R_c at these latitudes.

Figure 51 shows a typical measurement of CR transition curves in the atmosphere obtained two years before a solar maximum (cosmic ray minimum). The data obtained during quiet geomagnetic conditions show the secondary flux in the atmosphere originating from galactic CR's alone. The secondary CR fluxes grow with increasing altitude until

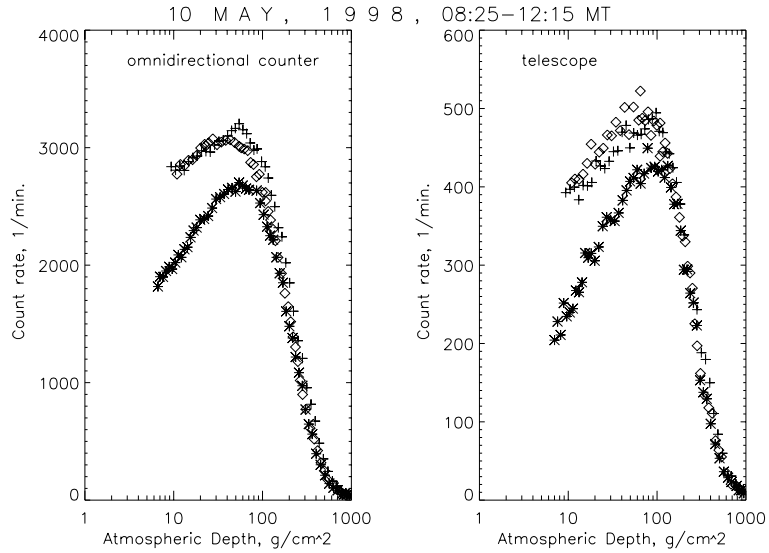

Figure 51: Balloon-borne measurements of cosmic ray intensities in northern latitudes: Mirny (plus sign), Murmansk (diamond) and Moscow (asterisk). Data are shown for the omnidirectional counter (left panel) and the vertical telescope (right panel). The data are obtained in May 1998, two years before a solar maximum (cosmic ray minimum).

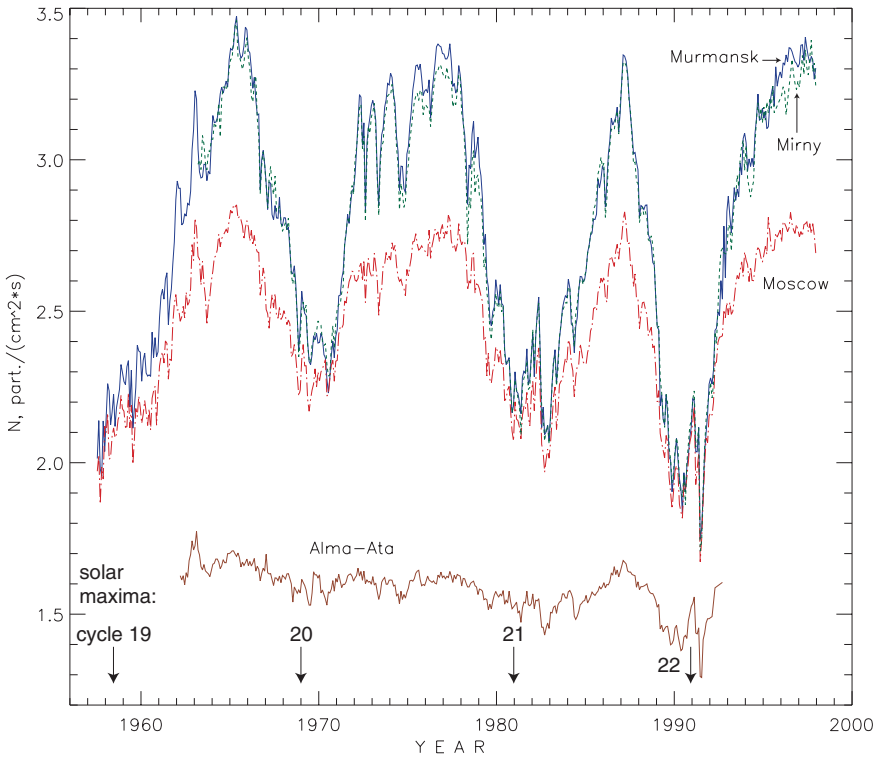

Figure 52: Cosmic ray intensity at the Pfotzer maximum in the atmosphere as measured by the omnidirectional Geiger counter. The lines correspond to different locations for the balloon flights: Mirny, Murmansk, Moscow and Alma-Ata. The data of Murmansk and Mirny practically coincide with each other. The approximate times of the sunspot maxima for the last 4 solar cycles are indicated.

Table 10: Summary of the monitoring stations used for long-term cosmic ray measurements by the Lebedev Physical Institute.

Station	**Location**	**Geomagnetic cutoff rigidity, R_c [GeV/c]**
Mirny (Antarctica)	66.34S, 92.55E	0.03
Murmansk	68.57N, 33.03E	0.6
Moscow	55.56N, 37.11E	2.4
Alma-Ata	43.25N, 76.92E	6.7

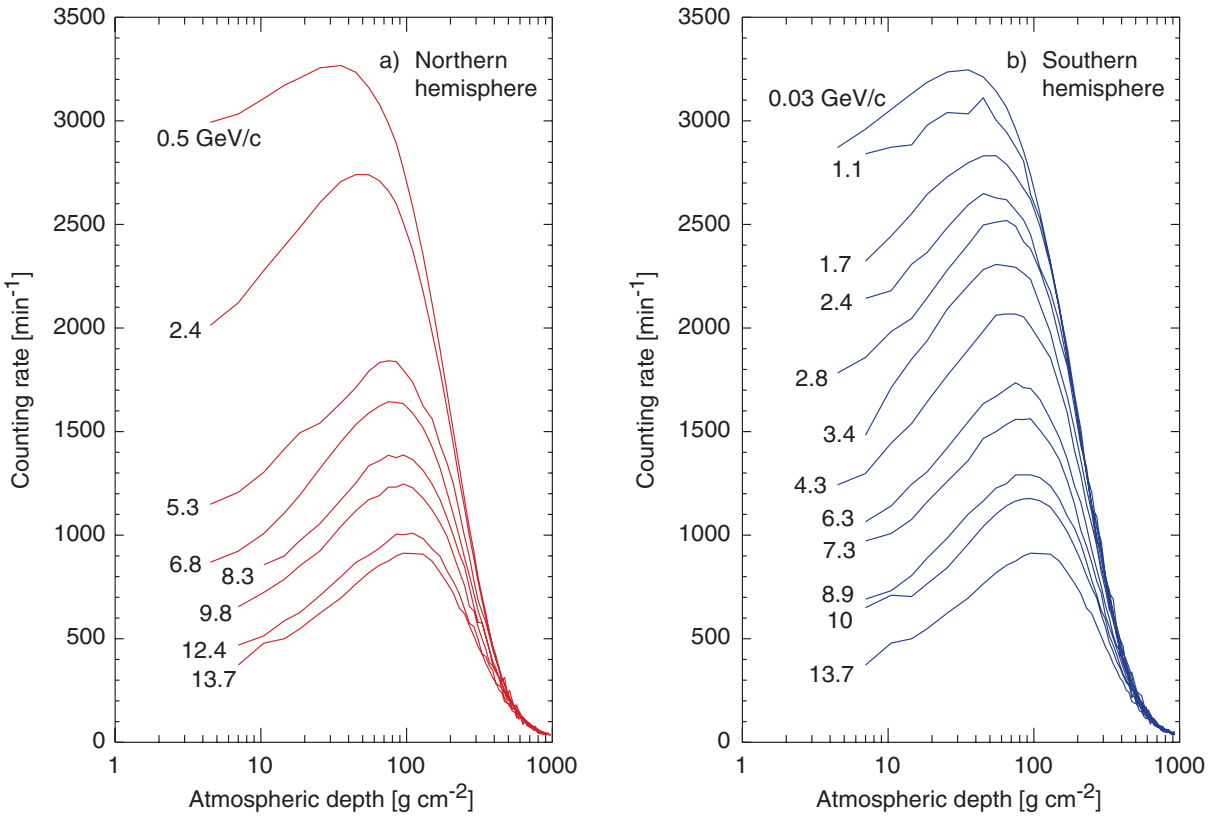

Figure 53: Cosmic ray intensities vs. altitude and geomagnetic latitude. Each curve corresponds to a different latitude with cutoff rigidity, R_c (GeV/c), as indicated. The data were recorded with the omnidirectional counter during the 1987 (cosmic ray maximum) survey of a) the northern and b) the southern hemispheres [155, 156].

they reach a maximum (which is known as the Pfotzer maximum, N_{max}) at 16–25 km. The value of N_{max} depends on the geomagnetic latitude and phase of the solar activity cycle. The counting rates are substantially increased in the upper atmosphere at times of special events such as solar particle events, coronal mass ejections, energetic electron precipitations, radioactive clouds, etc.

While propagating inside the heliosphere, the GCR intensity is modulated by solar activity. The balloon CR observation provide experimental data over 4 cycles of solar activity for the study of long-term modulation of GCR's and its effects on atmospheric phenomena. Figure 52 shows the monthly-averaged Pfotzer maxima measured with the omnidirectional counter at the sites of permanent launchings. The main feature of the GCR intensity is the 11-year solar cycle. It is seen that the amplitude of the solar cycle modulation depends strongly on R_c, being up to 70% at the polar stations, 30% at Moscow and about 10% at Alma-Ata. These data also provide evidence for a systematic decrease of cosmic ray intensity over the last 40 years (Table 2) [37].

To study the global distribution of CR in the atmosphere we carried out *latitude* surveys of CR fluxes in the atmosphere. Such a surveys were fulfilled during the sea expeditions in 1962–1965, 1968–1971, 1975–1976, 1979–1980 and in 1987. The measurements covered the R_c range from 0.03 to 15–17 GeV/c [155, 156]. In Figure 53 we give an example of the CR transition curves obtained at different latitudes in the northern and southern hemispheres during the 1987 solar minimum (cosmic ray maximum). Each curve averages the data from the omnidirectional counter recorded over several radiosonde flights. The ratio of N_{max} at polar latitudes to its value at the equator is about a factor 3.6.

E Cloud models

Marine stratus cloud model: The MISTRA (microphysical stratus) model [157] is a one-dimensional model of stratus clouds including a detailed treatment of size-segregated aerosol and cloud microphysical processes, which is essential in this study. Aerosols and cloud are treated either in a 2-dimensional particle distribution or as internal mixtures with 40 aerosol and 50 droplet size class. The hygroscopic growth and evaporation of aerosols in sub-saturated air and their activation to form droplets are explicitly calculated by solving the droplet growth equation for all droplets at all humidities. Coalescence of droplets necessary for the simulation of warm rain is included [158]. The model has a vertical resolution of 10 m from ground level to 1 km (spanning the cloud level), a further 50 logarithmically spaced grid levels up to 2 km (to treat dynamics and radiative transfer only) and a homogeneous layer up to 50 km (for radiative transfer only). Entrainment of aerosols is accounted for using a turbulent kinetic energy closure scheme. Radiative transfer is treated using a δ-two stream approximation (12 broad-band intervals from 4–100 μm and 6 intervals from 0.2–4 μm).

Cumulus cloud model: Cumulus clouds will be simulated using a two-dimensional slab-symmetric non-hydrostatic cloud model including detailed cloud microphysics. Four hydrometeor classes are considered: water drops, ice crystals, graupel particles and snowflakes (aggregates of ice crystals). The warm microphysical processes included are

nucleation of CCN, condensation and evaporation, collision-coalescence, binary breakup, and sedimentation. The ice microphysical processes included are drop freezing, ice nucleation (deposition and condensation-freezing, and contact nucleation), ice multiplication, deposition and sublimation of ice, interactions of ice-ice and ice-drop (aggregation, accretion and riming), melting of ice particles, and sedimentation of ice particles. All the microphysical processes are formulated as kinetic equations and solved using the method of Multi-Moments [159]–[162].

Each type of particle is divided into 34 bins with mass doubling for connected bins. The masses at the beginning of the first bin and the end of last bin for both liquid and solid phases are 0.160×10^{-13} and 0.175×10^{-3} kg, which correspond to drop diameters of 3.13 and 8060 μm, respectively.

This model has been used in studies concerning the effect of natural and artificial large and giant CCN on development of cloud particles and precipitation in convective clouds (e.g. refs. [163, 164]). It is currently being extended to include the evolution of aerosols inside various hydrometeors in order to study the venting of trace gases and aerosols by convective clouds.

References

[1] H. Svensmark and E. Friis-Christensen, Variation in cosmic ray flux and global cloud coverage—a missing link in solar-climate relationships, *Journal of Atmospheric and Solar-Terrestrial Physics* **59** (1997) 1225.

[2] M. Lockwood, R. Stamper and M.N. Wild, A doubling of the Sun's coronal magnetic field during the past 100 years, *Nature* **399** (1999) 437.

[3] F. Arnold, Ion nucleation - a potential source for stratospheric aerosols, *Nature* **299** (1982) 134.

[4] R.P. Turco, J.-K. Zhao and F. Yu, A new source of tropospheric aerosols: ion-ion recombination, *Geophys. Res. Lett.* **25** (1998) 635.

[5] F. Yu and R.P. Turco, Ultrafine aerosol formation via ion-mediated nucleation, *Geophys. Res. Lett.* **27** (2000) 883.

[6] S. Eichkorn, K. H. Wohlfrom, and F. Arnold, Massive ion detection in the upper troposphere: implications for aerosol particle formation via ion-induced nucleation, poster presented at the *EGS General Assembly*, The Hague (1999).

[7] B.A. Tinsley and G.W. Dean, Apparent tropospheric response to MeV–GeV particle flux variations: a connection via the solar wind, atmospheric electricity and cloud microphysics, *J. Geophys. Res.* **96** (1991) 22283.

[8] Intergovernmental Panel on Climate Change (IPCC), *Climate change 1995: the science of climate change*, eds. J.T. Houghton et al., WMO and UNEP, Cambridge University Press, Cambridge (1996).

[9] *Aerosol-cloud-climate interactions*, International Geophysics Series, Vol. 54, ed. P.V. Hobbs, Academic Press Inc., San Diego (1993).

[10] P.V. Foukal, The variable Sun, *Scientific American* **262** (1990) 26.

[11] W. Herschel, Some remarks on the stability of the light of the Sun, *Philosphical Transactions of the Royal Society*, London (1796) 166.

[12] J.A. Eddy, The Maunder minimum, *Science* **192** (1976) 1189.

[13] R. Dickinson, Solar variability and the lower atmosphere, *Bull. Am. Met. Soc.* **56** (1975) 1240.

[14] J.R. Herman and R.A. Goldberg, *Sun, weather, and climate*, *NASA* **SP 426** (1978).

[15] D.V. Hoyt and K.H. Schatten, *The role of the Sun in climate change*, Oxford Univ. Press, Oxford (1997).

[16] E. Friis-Christensen and K. Lassen, Length of the solar cycle: an indicator of solar activity closely associated with climate, *Science* **254** (1991) 698.

[17] *The Sun in time*, eds. C.P. Sonett, M.S. Giampapa and M.S. Matthews, University of Arizona Press, Tucson (1991).

[18] C. Fröhlich, P.V. Foukal, J.R. Hickey, H.S. Hudson and R.C. Willson, Solar irradiance variability from modern measurements, in ref. [17], p.11.

[19] C. Fröhlich and J. Lean, *Proc. IAU Symposium 185*, ed. F.L. Deubner, Kyoto (1997).

[20] E.P. Ney, Cosmic radiation and the weather, *Nature* **183** (1959) 451.

[21] L.J. Gleeson and W.I. Axford, Cosmic rays in the interplanetary medium, *Astrophys. J.* **149** (1967) 115; also, Solar modulation of galactic cosmic rays, *Astrophys. J.*, **154** (1968) 1011.

[22] K.O. O'Brien, A. De La Zerda Lerner, M.A. Shea and D.F. Smart, The production of comsogenic isotopes in the Earth's atmosphere and their inventories, in ref. [17], p.317.

[23] J. Masarik and J. Beer, Simulation of particle fluxes and cosmogenic nuclide production in the Earth's atmosphere, *J. Geophys. Res.* **104** D10 (1999) 12099-12111.

[24] H. Svensmark, Influence of cosmic rays on the Earth's climate, *Phys. Rev. Lett.* **81** (1998) 5027.

[25] M.I. Pudovkin and S.V. Veretenenko, Cloudiness decreases associated with Forbush decreases of galactic cosmic rays, *J. Atmos. Solar-Terrestrial Phys.* **75** (1995) 1349.

[26] Yu. I. Stozhkov *et al.*, Rainfalls during great Forbush decreases, *Il Nuovo Cimento* **18C** (1995) 335.

[27] D.M. Hunten, J.-C. Gérard and L.M. François, The atmosphere's response to solar irradiation, in ref. [17], p.463.

[28] J.D. Haigh, The impact of solar variability on climate, *Science* **272** (1996) 981.

[29] M.A. Geller and J.C. Alpert, Planetary wave coupling between the troposphere and the middle atmosphere as a possible Sun–weather mechanism, *J. Atmos. Sci.* **37** (1980) 1197.

[30] D. Shindell *et al.*, Solar cycle variability, ozone, and climate, *Science* **284** (1999) 385.

[31] W.B. Rossow, and R.A. Schiffer, ISCCP Cloud Data Products, *Bull. Am. Met. Soc.* **72** (1991) 2.

[32] W.B. Rossow, A.W. Walker, D.E. Beuschel, and M.D. Roiter, *International Satellite Cloud Climatology Project (ISCCP): documentation of new cloud datasets*, WMO/TD **737**, World Meteorological Organization, Geneva (1996).

[33] N. Marsh and H. Svensmark, Low cloud properties influenced by solar activity, submitted to *Geophys. Res. Lett.* (2000).

[34] A.J. Heymsfield, Microphysical structures of stratiform and cirrus clouds, in ref. [9], p.97.

[35] D.L. Hartmann, Radiative effects of clouds on Earth's climate, in ref. [9], p. 151.

[36] J. Beer, G.M. Raisbeck and F. Yiou, Time variations of ^{10}Be and solar activity, in ref. [17], p.343.

[37] Y.I. Stozhkov *et al.*, Long-term negative trend in cosmic ray flux, *J. Geophys. Res.* **105** (2000) 9.

[38] P.-N. Mayaud, The aa indices: a 100-year series characterizing the magnetic activity, *J. Geophys. Res.* **77** (1972) 6870.

[39] P.E. Damon and C.P. Sonett, Solar and terrestrial components of the atmospheric ^{14}C variation spectrum, in ref. [17], p.360.

[40] D. Verschuren, K. Laird and B. Cumming, Rainfall and drought in equatorial East Africa during the past 1100 years, *Nature* **403** (2000) 410.

[41] F. Raes and A. Janssens, Ion-induced aerosol formation in a H_2-H_2SO_4 system - I. Extension of the classical theory and search for experimental evidence, *J. Aerosol Sci.* **16** (1985) 217.

[42] F. Raes, A. Janssens and R.V. Dingenen, The role of ion-induced aerosol formation in the lower atmosphere, *J. Aerosol Sci.* **17** (1986) 466.

[43] F. Arnold, Multi-ion complexes in the stratosphere: implications for trace gases and aerosols, *Nature* **284** (1980) 610.

[44] U. Hõrrak, J. Salm and H. Tammet, Bursts of intermediate ions in atmospheric air, *J. Geophys. Res.* **103** D12 (1998) 13909.

[45] C.D. O'Dowd, M.H. Smith, J.A. Lowe, R.M. Harrison, B. Davison and C.N. Hewitt, New particle formation in the marine environment, *Proc. 14th Int. Conf. on Nucleation and Atmospheric Aerosols*, eds. M. Kulmala and P.E. Wagner, Elsevier Science (1996) 925.

[46] M.K. Kulmala, L. Pirjola and J.M. Mäkëla, Stable sulphate clusters as a source of new atmospheric particles, *Nature* **404** (2000) 66.

[47] C.T.R. Wilson, *Philos. Trans.* **A 193** (1899) 289.

[48] L.B. Loeb, A.F. Kip and A.W. Einnarssonn, *J. Chem. Phys.* **6** (1938) 264.

[49] V. Talanquer and D.W. Oxtoby, Nucleation in molecular and dipolar fluids: interaction site model, *J. Chem. Phys.* **103** (1995) 3686.

[50] A.I. Rusanov and F.M. Kuni, Reformulation of the thermodynamic theory of nucleation on charged particles, *J. Colloid and Interface Science* **100** (1984) 264.

[51] D. Rosenfeld, Suppression of rain and snow by urban and industrial air pollution, *Science* **287** (2000) 1793.

[52] C.-C. Cheng, C.-J. Tao and H.-J. Shu, Heterogeneous nucleation of n-butanol vapour on submicrometer charged and neutral particles of lactose and monosodium glutamate, *J. Colloid Interface Sci.* **224** (2000) 11.

[53] P.J. Crutzen and F. Arnold, Nitric acid formation in the cold antarctic atmosphere: a major cause for the springtime 'ozone hole', *Nature* **324** (1986) 651.

[54] R. Müller and P.J. Crutzen, A possible role of galactic cosmic rays in chlorine activation during polar night, *J. Geophys. Res.* **98** (1993) 20483.

[55] M. Nicolet, On the production of nitric oxide by cosmic rays in the mesosphere and stratosphere, *Planet. Space Sci.*, **23** (1975) 637.

[56] C.H. Jackman, J.E. Frederick and R.S. Stolarski, Production of odd nitrogen in the stratosphere and mesosphere: an intercomparison of signal strengths, *J. Geophys. Res.* **85** C12 (1980) 7495.

[57] P.J. Crutzen, I.A.S. Isaksen and G.C. Reid, Solar proton events: stratospheric sources of nitric oxide, *Science* **189** (1975) 457.

[58] G. Dreschhoff and E.J. Zeller, Ultra-high resolution nitrate in polar ice as indicator of past solar activity, *Solar Physics* **177** (1998) 365.

[59] G.E. Kocharov, M.G. Ogurtsov, and G.A.M. Dreschhoff, On the quasi-five-year variation of nitrate abundance in polar ice and solar-flare activity in the past, *Solar Physics* **188** (1999) 187.

[60] H.R. Pruppacher and J.D. Klett, *Microphysics of clouds and precipitation*, 2nd ed., Kluwer Academic Publishers, The Netherlands (1997).

[61] R.J. Anderson, R.C. Miller, J.L. Kassner, Jr., and D.E. Hagen, A study of homogeneous condensation-freezing nucleation of small water droplets in an expansion cloud chamber, *J. Atmospheric Sciences* **37**, No. 11 (1980) 2508–2520.

[62] A. Krieger and F. Arnold, First composition measurements of stratospheric negative ions and inferred gaseous sulphuric acid in the winter arctic vortex: Implications for aerosols and hydroxyl radical formation, *Geophys. Res. Lett.* **21** (1994) 1259.

[63] S. Solomon, Stratospheric ozone depletion: a review of concepts and history, *Rev. Geophys.* **37** (1999) 275-316.

[64] T. Peter, Microphysics and heterogeneous chemistry of polar stratospheric clouds, *Ann. Rev. Phys. Chem.* **48** (1997) 785-822.

[65] K.S. Carslaw, T. Peter and S.L. Clegg, Modelling the composition of liquid stratospheric aerosols, *Revs. Geophys.* **35** (1997) 125-154.

[66] A.E. Waibel, T. Peter, K.S. Carslaw, H. Oelhaf, G. Wetzel, P.J. Crutzen, U. Pöschl, A. Tsias, E. Reimer and H. Fischer, Arctic ozone loss due to denitrification, *Science* **283** (1999) 2064-2069.

[67] T. Koop, K.S. Carslaw and T. Peter, Thermodynamic stability and phase transitions of PSC particles, *Geophys. Res. Lett.* **24** (1997) 2199-2202.

[68] K.S. Carslaw, T. Peter, J.T. Bacmeister, S.D. Eckermann, Widespread solid particle formation by mountain waves in the Arctic stratosphere, *J. Geophys. Res.* **104** (1999) 1827-1836.

[69] T. Koop, B.P. Luo, U.M. Biermann, P.J. Crutzen, T. Peter, Freezing of $HNO_3/H_2SO_4/H_2O$ solutions at stratospheric temperatures: Nucleation statistics and experiments, *J. Phys. Chem.* **A 101** (1997) 1117-1133.

[70] C.T.R. Wilson, Expansion apparatus, *Proc. Royal Society of London* **A 87** (1912) 277.

[71] P. Galison, *Image and Logic; a material culture of microphysics*, University of Chicago Press, Chicago (1997).

[72] G.R. Evans and A.A. Watson, Production of hypersensitive condensation nuclei, *Nature* **196** (1962) 729; G.R. Evans *et al.*, Some remarks on the origin and elimination of background cloud in expansion cloud chambers, *J. Sci. Inst.* **41** (1964) 770; G.R. Evans and A.A. Watson, Nitrogen dioxide vapour and the creation of condensation nuclei, *Proc. Royal Society of Edinburgh* **LXVII** part III-10 (1966) 136.

[73] A. Hervé and G. Bachy, Huge electrohydraulic servovalves control 2-ton cryogenic piston, *Hydraulics & Pneumatics*, Pention/IPC, Cleveland, Ohio (1977); and, The hydraulic expansion servo-system of the Big European Bubble Chamber, CERN preprint CERN/EF 77-6 (1977).

[74] P. Minginette, CERN Technical Note, CERN EP/EC-TO 2000-09 (1997).

[75] R. Strey, P.E. Wagner and T. Schmeling, Homogeneous nucleation rates for n-alcohol vapours measured in a two-piston expansion chamber, *J. Chem. Phys.* **84** (1986) 2325.

[76] R. Rudolf and P.E. Wagner, Experimental study of condensational particle growth in nitric acid - water vapour mixtures at nearly ambient pressures and temperatures, *J. Aerosol Sci.* **25**, S97 (1994).

[77] Y. Viisanen, P.E. Wagner and R. Strey, Measurement of the molecular content of binary nuclei: IV. Use of the nucleation rate surfaces for the n-nonane - n-alcohol series, *J. Chem. Phys.* **108** (1998) 4257.

[78] P.E. Wagner, A constant-angle Mie scattering method (CAMS) for investigation of particle formation processes, *J. Colloid Interface Sci.* **105** (1985) 456.

[79] W.W. Szymanski and P.E. Wagner, Absolute aerosol number concentration measurement by simultaneous observation of extinction and scattered light, *J. Aerosol Sci.* **21** (1990) 441.

[80] G. Mie, Beiträge zur optik trüber medien, speziell kolloidaler metallösungen, *Ann. Phys.* **25** (1908) 377.

[81] P. Debye, Der lichtdruck auf kugeln von beliebigem material, *Ann. Phys.* **30** (1909) 57.

[82] C.F. Bohren, and D.R. Huffmann, *Absorption and scattering of light by small particles*, John Wiley and Sons, New York (1983).

[83] D. Filipovicova, Bestimmung hoher partikelkonzentrationen mit hilfe simultaner streulicht- und extinktionsmessungen in einer expansionskammer, M.S. Thesis, University of Vienna (1996).

[84] W.C. Hinds, *Aerosol technology*, John Wiley and Sons, New York (1982).

[85] K. Willeke and P. Baron, *Aerosol Measurement,* Van Nostrand Reinhold, New York (1993).

[86] H.G. Scheibel and J. Porstendrfer, Generation of monodisperse Ag- and NaCl-aerosols with particle diameters between 2 and 300 nm, *J. Aerosol Science* **14** (1982) 113-126.

[87] S. Mertes, F. Schröder and A. Wiedensohler, The particle detection efficiency curve of the TSI-3010 CPC as a function of temperature difference between saturator and condenser, *Aerosol Sci. Technol.* **23** (1995) 257-261.

[88] M.R. Stolzenburg and P.H. McMurry, An ultrafine aerosol condensation nucleus counter, *Aerosol Sci. Technol.* **14** (1991) 48-65.

[89] A. Wiedensohler, P. Aalto, D. Covert, J. Heintzenberg and P.H. McMurry, Intercomparison of four methods to determine size distributions of low-concentration ($\sim$100 cm^{-3}) ultrafine aerosols (3nm $< D_p <$ 410nm) with illustrative data from the Arctic, *Aerosol Science and Technology* **21** (1994) 95-109.

[90] E.O. Knutson and K.T. Whitby, Aerosol classification by electric mobility: apparatus, theory and applications, *J. Aerosol Sci.* **6** (1975) 443-451.

[91] W. Winklmayr, G.P. Reischl, A.O. Lindner and A. Berner, A new electromobility spectrometer for the measurement of aerosol size distributions in the size range from 1 to 1000 nm, *J. Aerosol Sci.* **22** (1991) 289-296.

[92] V. Jokinen and J.M. Mäkelä, Closed loop arrangement with critical orifice for DMA sheath/excess flow system, *J. Aerosol Science* **28** (1997) 643-648.

[93] G.P. Reischl, J.M. Mäkelä and J. Necid, Performance of Vienna Type DMA at 1.2-20 nanometre, *Aerosol Science and Technology* **27** (1997) 651-672.

[94] A. Wiedensohler, An approximation of the bipolar charge distribution for particles in the submicron size range, *J. Aerosol Sci.* **19** (1988) 387-389.

[95] G.P. Reischl, J.M. Mäkelä, R. Karch and J. Necid, Bipolar charging of ultrafine particles in the size range below 10 nm, *J. Aerosol Science* **27** (1996) 931-949.

[96] Y. Kousaka, K. Okuyama and M. Adachi, Determination of particle size distribution of ultra-fine aerosols using a differential mobility analyser, *Aerosol Sci. Technol.* **4** (1985) 209-225.

[97] P.G. Gormley and M. Kennedy, *Proc R. Ir. Acad.* **52A** (1949) 163-169.

[98] O. Möhler and F. Arnold, Flow reactor and triple quadrupole mass spectrometer investigations of negative ion reactions involving nitric acid: Implications for atmospheric HNO_3 detection by chemical ionization mass spectrometry, *J. Atm. Chem.* **13** (1991) 33.

[99] T. Reiner, O. Möhler and F. Arnold, Improved atmospheric trace gas measurements with an aircraft-based tandem mass spectrometer: Ion identification by mass-selected fragmentation studies, *J. Geophys. Res.* **103** (1998) 31309.

[100] J. Schneider, F. Arnold, V. Bürger, B. Droste-Franke, F. Grimm, G.Kirchner, M. Klemm, T. Stilp, K.-H. Wohlfrom, P. Siegmund and P.F.J. van Velthoven, Nitric acid (HNO_3) in the upper troposphere and lower stratosphere at midlatitudes: New results from aircraft-based mass spectrometric measurements, *J. Geophys. Res.* **103** (1998) 25,337.

[101] J. Curtius, B. Sierau, F. Arnold, R. Baumann, R. Busen, P. Schulte, and U. Schumann, First direct sulphuric acid detection in the exhaust plume of a jet aircraft in flight, *Geophys. Res. Lett.* **25** (1998) 923.

[102] K. H. Wohlfrom, T. Hauler and F. Arnold, Acetone in the free troposphere and lower stratosphere, Aircraft-based CIMS- and GC- measurements over the North Atlantic and a first comparison, *Geophys. Res. Lett.* **26** (1999) 2849.

[103] J.R. Holton, P.H. Haynes, M.E. McIntyre, A.R. Douglas, R.B. Rood, and L. Pfister, Stratosphere-troposphere exchange, *Rev. Geophys.* **33** (1995) 403.

[104] A. Kiendler, Aufbau und Einsatz einer neuartigen flugzeug-getragenen Ionenfallen-Massenspektrometer-Sonde zur Analyse von Spurengasen und Ionen: Messungen im Labor, im Abgas von Düsentriebwerken und atmosphärische Spurengasmessungen mit Flugzeugen, *PhD thesis* Univ. Heidelberg (1999).

[105] B. Fastrup, E. Horsdal-Pedersen, V.V. Afrosimov, A.A. Basalaev and M.N. Panov, 21 ICPEAC, Abstracts of Contributed Papers, Sendai, Japan, 462 (1999) 462.

[106] K. H. Wohlfrom, Measurements of ions and trace gases by aircraft-based mass spectrometers: New insights into ozone, aerosols, and the impact of air traffic on the atmosphere, *PhD thesis,* Univ. Heidelberg (2000).

[107] K. H. Wohlfrom, S. Eichkorn and F. Arnold, Very massive positive and negative chemiions in jet engine exhaust at the ground: Mass distribution measurements and implications for aerosol formation, *manuscript in preparation* (2000).

[108] K. H. Wohlfrom, S. Eichkorn and F. Arnold, Detection of very massive positive and negative chemiions in the wake of a jet aircraft in flight: Mass distribution measurements by an aircraft based Ion Mass Spectrometer, *manuscript in preparation* (2000).

[109] F. Yu, and R. Turco, The role of ions in the formation and evolution of particles in aircraft plumes, *Geophys. Res Lett.* **24** (1997) 1927.

[110] F. Yu, R. Turco, B. Kärcher, and F. Schröder, On the mechanisms controlling the formation and properties of volatile particles in aircraft wakes, *Geophys. Res Lett.* **25** (1998) 3839.

[111] F. Arnold, Curtius, J., Sierau, B., Bürger, V., Busen, R., Schumann, U., Detection of massive negative chemiions in the exhaust plume of a jet aircraft in flight, *Geophy. Res. Lett.* **26** (1999)1577.

[112] F. Arnold, V. Wiedemer, S. Aberle, A. Kiendler, and T. Stilp, Chemiion concentration measurements in jet engine exhaust at the ground: Implications for ion chemistry and aerosol formation in the wake of a jet aircraft, *Geophy. Res. Lett.* submitted (2000).

[113] A. Kiendler, S. Aberle and F. Arnold, Negative chemiions formed in jet fuel combustion: New insights from jet engine and laboratory measurements using a quadrupole ion trap mass spectrometer apparatus, *Atmos. Environ.* in press (2000).

[114] R.G. Harrison and K.L. Aplin, The interaction between air ions and aerosol particles in the atmosphere, in *Proc. 10th Int. Electrostatics Conf.*, Cambridge, 28–31 March 1999, ed. D.M. Taylor, Institute of Physics Conference series **163**, Cambridge (1999) 411.

[115] K.L. Aplin and R.G. Harrison, A computer-controlled Gerdien ion counter, accepted by *Rev. Sci. Inst.* (2000).

[116] R.G. Harrison, A noise-rejecting current amplifier for surface atmospheric ion flux measurements, *Rev. Sci. Instrum.* **68** (1997) 3563.

[117] R.G. Harrison and K.L. Aplin, Femtoampere current reference stable over atmospheric temperatures, accepted by *Rev. Sci. Inst.* (2000).

[118] Further information on ROOT can be found at http://root.cern.ch.

[119] Details on LHC++ can be found at http://wwwinfo.cern.ch/asd/lhc++/index.html.

[120] R.R. Rogers and M.K. Yau, *A short course in cloud physics*, 3rd edition, Butterworth-Heinemann, Woburn, USA (1989).

[121] M. Kulmala, A. Laaksonen, P. Korhonen, T. Vesala, T. Ahonen and J.C. Barrett, The effect of atmospheric nitric acid vapour on cloud condensation nucleus activation, *J. Geophys. Res.* **98** (1993) 22949-22958.

[122] N.A. Fuchs and A.G. Sutugin, *Highly dispersed aerosols,* Ann Arbor Science Publ., Ann Arbor, Michigan (1970) 105 p.

[123] W.H. Press, B.P. Flannery, S.A. Teukolsky and W.T. Vettering, *Numerical recipies*, Cambridge University Press, New York (1986).

[124] T. Mattila, M. Kulmala and T. Vesala, On the condensational growth of a multicomponent droplet, *J. Aerosol Sci.* **28** (1997) 553-564.

[125] R. Rudolf, Experimental investigation on condensation of supersaturated acid-water vapour mixtures by means of laser light scattering in a newly developed expansion chamber, Ph.D. thesis, Formal-und Naturwissenschaftlichen Fakultät, University of Vienna (1994).

[126] N.N. Das Gupta and S.K. Ghosh, A report on the Wilson cloud chamber and its application in physics, *Rev. Modern Physics* **18** (1946) 225–290.

[127] R. Veenhof, The GARFIELD program v.7.01, http://consult.cern.ch/writeup/garfield (2000). The electric field is modelled with the Maxwell 3D Field Simulator, Ansoft Corporation, Pittsburgh, USA, http://www.ansoft.com.

[128] C.F. Clement and R.G. Harrison, The charging of radioactive aerosols, *J. Aerosol Sci.* **23** (1992) 481.

[129] J. Seinfeld and S.N. Pandis, *Atmospheric Chemistry and Physics*, Wiley, New York (1998).

[130] S.E. Schwartz and A. Slingo, Enhanced shortwave cloud radiative forcing due to anthropogenic aerosols, in *Clouds, Chemistry and Climate*, Proceedings of NATO Advanced Study Workshop, edited by P. Crutzen and V. Ramanathan, Springer, Heidelberg (1996) 191–236.

[131] R.J. Charlson, J. Lagner, H. Rodhe, C.B. Leovy and S.G. Warren, Perturbation of northern hemisphere radiative balance by backscattering from anthropogenic sulphate aerosols, *Tellus* **43AB** (1991) 152-163.

[132] R.J. Charlson, S.E. Schwartz, J.M. Hales, R.D. Cess, J.A. Coakley, Jr., J.E. Hansen and D.J. Hofmann, Climate forcing by antropogenic aerosols, *Science* **255** (1992) 423-430.

[133] R.J. Charlson and T.M.L. Wigley, sulphate aerosol and climatic change, *Scientific American* **2** (1994) 48-57.

[134] J.A. Curry, Interactions among aerosols, clouds and climate of the Artic Ocean, *The science of the total environment*, **160/161** (1995) 777-791.

[135] D.L. Hartmann and D. Doelling, On the net radiative effectiveness of clouds, *J. Geophys. Res.*, **96** (1991) 869-891.

[136] S. Twomey, The influence of pollution on the shortwave albedo of clouds, *J. Atmos. Sci.* **34** (1977) 1149-1152.

[137] X.Q. Zhang, P.H. McMurry, S.V. Hering and G.S. Casuccio, Mixing characteristics and water content of submicron aerosols measured in Los Angles and at the Grand Canyon, *Atm. Env.* **27A** (1993) 1593-1608.

[138] I.B. Svenningsson, H.-C. Hansson, A. Wiedensohler, J.A. Ogren, K.J. Noone and A. Hallberg, Hygroscopic growth of aerosol particles in the Po valley, *Tellus* **44B** (1992) 556-569.

[139] I.B. Svenningsson, H.-C. Hansson, A. Wiedensohler, K.J. Noone, J. Ogren, A. Hallberg and R. Colvile, Hygroscopic growth of aerosol particles and its influence on nucleation savenging in cloud: experimental results from Kleiner Feldberg, *J. Atmospheric Chem.* **19** (1994) 129-152.

[140] P. Korhonen, M. Kulmala, H.-C. Hansson, I.B. Svenningsson and N. Rusko, Hygroscopicity of pre-existing particle distribution and formation of cloud droplets: a model study, *Atmospheric Research* **41** (1996) 249-266.

[141] M. Kulmala, P. Korhonen, T. Vesala, H.-C. Hansson, K. Noone and B. Svenningsson, The effect of hygroscopicity on cloud droplet formation, *Tellus* **48B** (1996) 347-360.

[142] P. Korhonen, M. Kulmala and T. Vesala, Model simulation of the amount of soluble mass during cloud droplet formation, *Atmos. Env.* **30**, Nos 10/11 (1996) 1773-1785.

[143] M.L. Schulman, M.C. Jacobson, R.J. Charlson, R.E. Synovec and T.E.Young, Dissolution behaviour and surface tension effects of organic compounds in nucleating cloud droplets, *Geophys. Res. Lett.* **23**, No. 3 (1996) 277-280.

[144] M. Kulmala, A. Toivonen, T. Mattila, P. Korhonen, Variations of cloud droplet concentrations and the optical properties of clouds due to changing hygroscopicity: a model study, *J. Geophys. Res.* **103** (1998) 16183-16195.

[145] A. Laaksonen, J. Hienola, M. Kulmala and F. Arnold, Supercooled cirrus cloud formation modified by nitric acid pollution of the upper troposphere, *Geophys. Res. Letters* **24** (1997) 3009-3102.

[146] M. Kulmala, A. Laaksonen, R.J. Charlson, P. Korhonen, Cloud without supersaturation, *Nature* **388** (1997) 336-337.

[147] A. Laaksonen, P. Korhonen, M. Kulmala and R.J. Charlson, Modification of the Köhler equation to include soluble trace gases and slightly soluble subtances, *J. Atmospheric Sci.* **55** (1998) 853-862.

[148] J.A. Ogren and R.J. Charlson, Implications for models and measurements of chemical inhomogeneities among cloud droplets, *Tellus* **44B** (1992) 208-225.

[149] E. Segrè, *Experimental nuclear physics*, Wiley, New York (1953) 53.

[150] V.I. Ermakov, G.A. Bazilevskaya, P.E. Pokrevsky, and Y.I. Stozhkov, Ion balance equation in the atmosphere, *J. Geophys. Res.* **102** (1997) 23413.

[151] A.A. Viggiano and F. Arnold, Ion chemistry and composition of the atmosphere, *Handbook of atmospheric electrodynamics*, Vol. 1, ed. H. Volland, CRC Press, Boca Raton (1998).

[152] H. Heitmann and F. Arnold, Composition measurements of tropospheric ions, *Nature* **306** (1993) 747.

[153] A.N. Charakhchyan, Radiosond for the measurement of cosmic ray intensity in the stratosphere, Kosmicheskiye Luchi, Moscow, AN USSR, No.3 (1961) 134-136 (in Russian).

[154] G.A. Bazilevskaya, M.B. Krainev, Y.I. Stozhkov, A.K. Svirzhevskaya and N.S. Svirzhevsky, Long-term Soviet program for the measurement of ionizing radiation in the atmosphere, *J. Geomagn. Geoelectr. Suppl.* **43** (1991) 893-900.

[155] V.K. Babarykin, V.V. Bayarevich, Y.I. Stozhkov and T.N. Charakhchyan, Latitude survey of cosmic ray intensity in the stratosphere, *Geomagnetizm i Aeronomia* **4** No.3 (1964) 458-463 (in Russian).

[156] A.E. Golenkov, A.K. Svirzevskaya, N.S. Svirzhevsky and Y.I. Stozhkov, Cosmic ray latitude survey in the stratosphere during the 1987 solar minimum, Proc. *21st Int. Cosmic Ray Conference*, Adelaide, v.7 (1990) 14-17.

[157] A. Bott, T. Trautmann, W. Zdunkowski, A numerical model of the cloud-topped planetary boundary layer: radiation, turbulence and spectral microphysics in marine stratus, *Q. J. R. Meteorol. Soc.* **122** (1996) 635.

[158] T. Trautmann and C. Wanner, A fast and efficient modified sectional method for simulating multicomponent collisional kinetics, *Atm. Environment* **33** (1999) 1631.

[159] S. Tzivion, G. Feingold, and Z. Levin, An efficient numerical solution to the stochastic collection equation, *J. Atmos. Sci.* **44** (1987) 3139.

[160] S. Tzivion, G. Feingold, and Z. Levin, The evolution of raindrop spectra; Part II: Collisional collection/breakup and evaporation in a rainshaft, *J. Atmos. Sci.* **46** (1989) 3312.

[161] G. Feingold, S. Tzivion, and Z. Levin, The evolution of raindrop spectra; Part I: Stochastic collection and breakup, *J. Atmos. Sci.* **45** (1988) 3387.

[162] T. Reisin, Z. Levin, and S. Tzivion, Rain production in convective clouds as simulated in an axisymmetric model with detailed microphysics; Part I: Description of the model, *J. Atmos. Sci.* **53** (1996) 497.

[163] Y. Yin, Z. Levin, T. G. Reisin, and S. Tzivion, The effects of giant cloud condensation nuclei on the development of precipitation in convective clouds — a numerical study, accepted for publication in *Atmospheric Research* (1999).

[164] Y. Yin, Z. Levin, T. G. Reisin, and S. Tzivion, Seeding convective clouds with hygroscopic flares: Numerical simulations using a cloud model with detailed microphysics, accepted for publication in *J. Appl. Meteor.* (1999).